Review of e^+e^- physics at PETRA

P. Duinker

National Institute of Nuclear and High Energy Physics, Amsterdam, The Netherlands

A review is given of the experimental investigation of high-energy e^+e^- interactions at PETRA, the electron-positron colliding beam accelerator at DESY in Hamburg, Germany. The energy of the machine is such that the strong, electromagnetic, and weak interactions start to play a role in the processes which can be studied. Results are presented on tests of quantum electrodynamics studying e^+e^-, $\mu^+\mu^-$, and $\tau^+\tau^-$. The fermion pair production processes $e^+e^-\rightarrow F\bar{F}$, where the $F\bar{F}$ pair stands for either a lepton pair (e^+e^-, $\mu^+\mu^-$, and $\tau^+\tau^-$) or a quark-antiquark pair, are investigated to study the effects of the Z° exchange. The measurements of R, the ratio of hadronic to pointlike muon pair cross section, the search for new quark flavors, and other new particles are reviewed. Finally the discovery of three-jet events arising from the radiation of hard noncollinear gluons as predicted by quantum chromodynamics and the determinations of the strong coupling constant α_s are discussed.

CONTENTS

I. INTRODUCTION

This article reviews the experimental results up to the middle of 1981 obtained with PETRA, the world's highest-energy electron-positron colliding beam storage ring, which is at DESY in Hamburg, Germany.

Five experiments (CELLO, JADE, MARK-J, PLUTO, and TASSO) were approved in 1976, and at the end of 1978 the first measurements were taken. The machine has been running with beam energies ranging from 6 to 18.5 GeV. The general features and the performance of PETRA are given in Sec. II. The experiments are discussed in Sec. III, starting with an overall view of the goals of the physics program in Sec. III.A and a description of the principal components of the detectors in Sec. III.B. Section III ends with a brief discussion of the Monte Carlo simulation programs in use for the various processes and some aspects of the radiative correction calculations.

Tests of quantum electrodynamics (QED) and the universality of the charged leptons are given in Secs. IV.A and B. The measurements of the asymmetry in the production of muon pairs and the first tests of models of

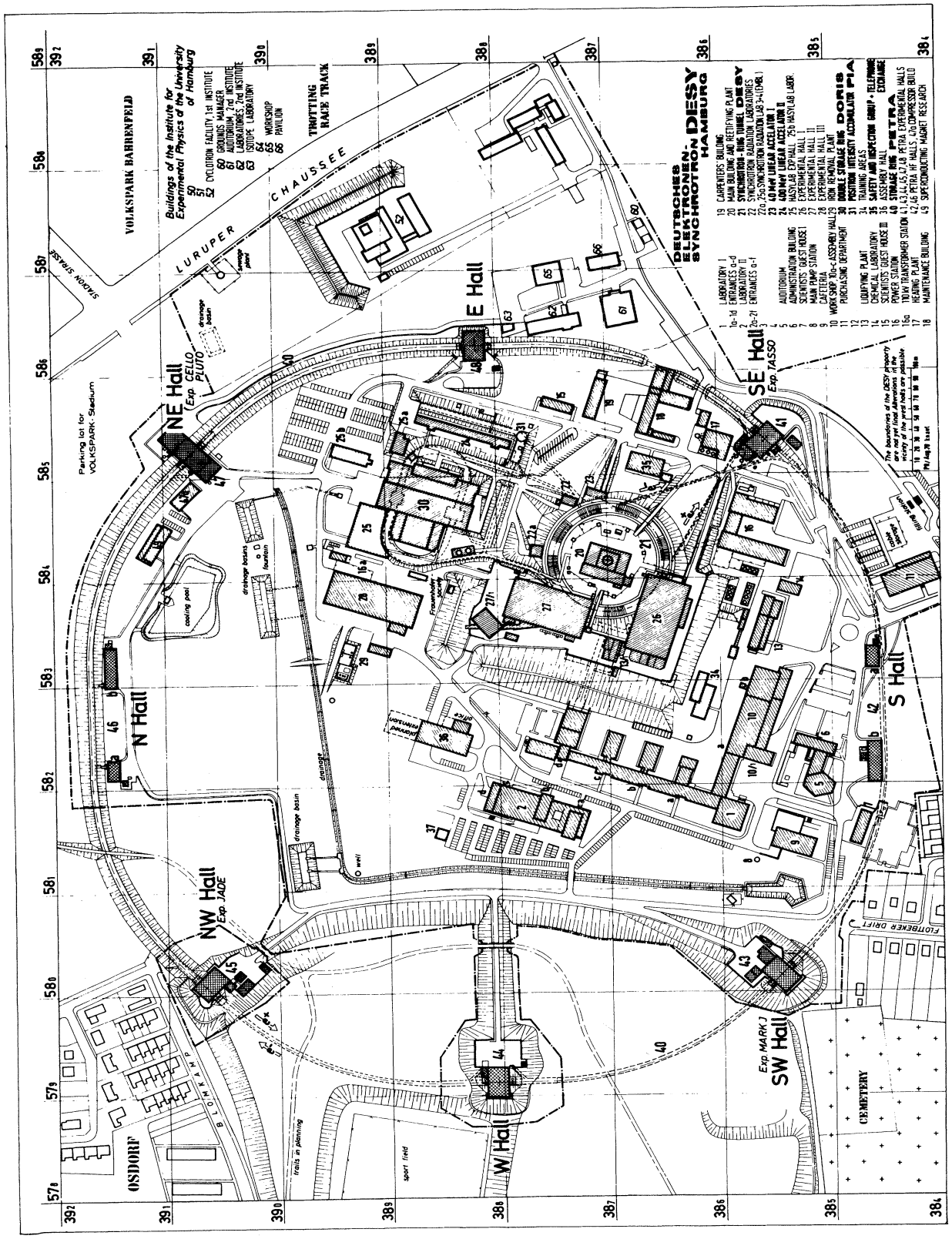

FIG. 1. Layout of the DESY site at Hamburg, West Germany with the PETRA e^+e^- storage ring showing the locations of the detectors. The N-E hall with PLUTO and CELLO, the S-E hall with TASSO, the S-W hall with MARK-J, and the N-W hall with the JADE detectors, respectively.

the electroweak interaction with one or more neutral bosons are presented in Secs. IV.C, D, and E.

PETRA makes possible for the first time the study of the two-photon exchange reaction in a systematic way with events samples comparable to the single-photon annihilation channel, and some of the results obtained so far are described in Sec. V.

The general characteristics of hadron events such as the total hadronic cross section, jet analysis, searches for the top quark in hadronic events with and without a muon, the searches for free quarks and other new particles, multiplicity distributions, particle spectra, and particle yields are presented in Sec. VI.

The tests of quantum chromodynamics (QCD) and the detailed analysis of an event topology by the JADE, MARK-J, PLUTO, and TASSO collaborations which led to the discovery of three-jet events arising from the radiation of hard noncollinear gluons are reviewed in Sec. VII.

Section VIII closes this review with a summary of the main results.

II. THE e^+e^- MACHINE PETRA

PETRA (Positron Elektron Tandem Ringbeschleuniger Anlage) began operation in the fall of 1978 as the world's higest-energy e^+e^- colliding beam machine. Since its commissioning, PETRA beams have been available for physics runs 60% of the time, with the remaining time being devoted to machine development and maintenance periods (PETRA Proposal, 1976; Voss, 1979)

The ring, with a circumference of 2.3 km, has eight long straight sections, of which two are reserved for the RF (radio frequency) accelerating cavities. At present only four of the experimental areas are occupied. The remaining two experimental areas are reserved for second-generation experiments.

The original injection scheme utilized both of the existing DESY facilities, DESY and DORIS. Electrons, initially accelerated in LINAC I (see Fig. 1) are injected into DESY (Deutsches Elektronen Synchrotron) where they are further accelerated to 6 GeV and injected into PETRA. Positrons follow a somewhat more complicated path: after initial acceleration in LINAC II, positrons are injected via DESY into DORIS (Doppel-Ring-Speicher), where they are accumulated at an energy of 2.2 GeV. Stored positron bunches in DORIS are then transferred back to DESY for further acceleration to 6 GeV, the minimum PETRA injection energy.

With the discovery of the Υ resonance in 1977 at FNAL (Herb *et al.*, 1977) and the confirmation in e^+e^- interactions (Darden *et al.*, 1978a, 1978b; Berger *et al.*, 1978a, Bienlein *et al.*, 1978), the need to operate DORIS as a storage ring independent of PETRA was realized. Consequently, in the fall of 1977 the decision was made to construct a positron intensity accumulator (PIA) (Febel and Hemmie, 1979) to free DORIS for physics runs. In this new injection scheme, positrons are accumulated in PIA after acceleration in LINAC II. Twenty

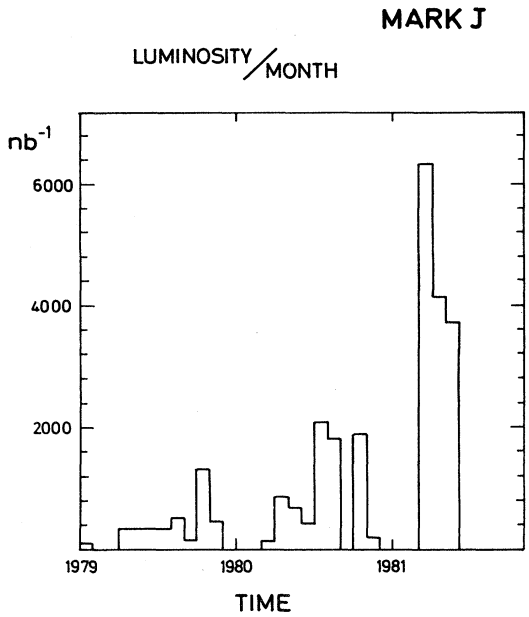

FIG. 2. The integrated luminosity per month obtained with the MARK-J detector since the beginning of 1979 as a function of time.

successive LINAC bunches are injected into PIA, compressed in phase space, and transferred to DESY for acceleration and injection into PETRA. PIA was assembled in record time and since the summer of 1979 has served as the injector for both DORIS and PETRA.

An important result was obtained in 1981, when the luminosity was increased considerably through installation of mini-β quadrupoles in the four intersection regions (Steffen, 1979). The time-integrated luminosity per month obtained since the beginning of 1979 with the MARK-J detector is shown in Fig. 2. The months without any luminosity are the periods of the major machine shutdowns. The striking increase, a factor ~ 3.5 in 1981, is due to the decrease in value of the vertical β function at the intersection point using the mini-β scheme. An average luminosity of $\sim 10^{31}$ cm^{-2} sec^{-1} at beam energies of ~ 17.5 GeV have been obtained.

Recently the vertical polarization of the beams caused by the synchrotron radiation has been observed by the PETRA polarimeter (Bremer *et al.*, 1980). Figure 3

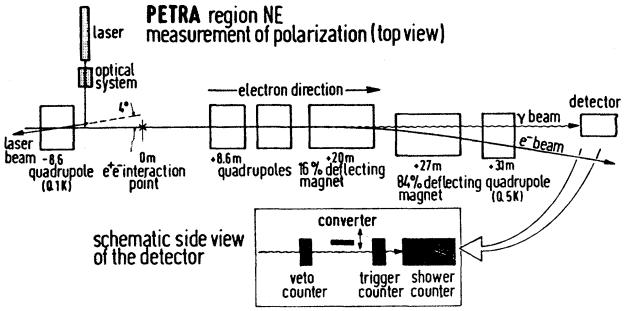

FIG. 3. Layout of the system to measure the polarization of the PETRA beams.

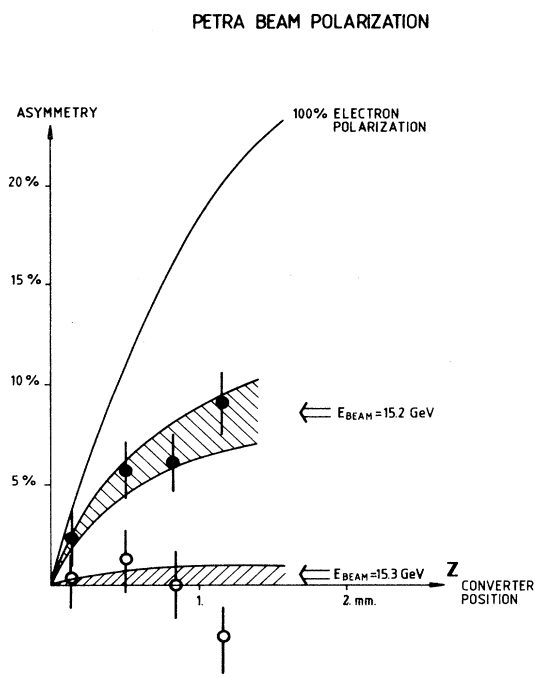

FIG. 4. Difference in counting rates between right- and left-handed circularly polarized light (asymmetry) as a function of the position of the converter. The solid line shows the expected asymmetry for 100% polarization. The open circles are the measurements for a beam energy of 15.3 GeV, and the black circles the ones at 15.2 GeV.

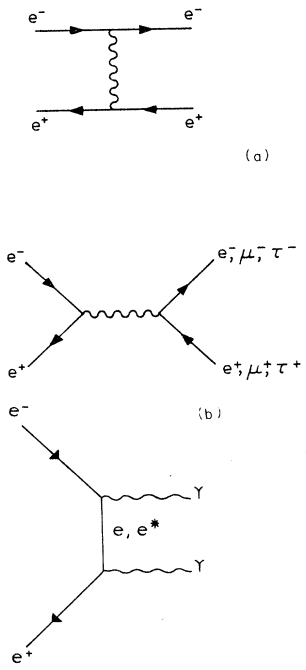

FIG. 5. (a) Electron, muon, and τ pair production in lowest order. (b) Photon production in lowest order.

shows the arrangment in the NE hall which is used to measure the polarization of the electron beam by detecting a backscattered circularly polarized photon beam. The detector measures the difference in counting rates between the scattered left- and right-handed photons as a function of the converter position.

In Fig. 4, the counting rate for 100% polarization is compared with the measured asymmetry values V, where

$$V=\frac{1}{2}\left[\frac{N_R-N_L}{N_R+N_L}\right]_{Z=a}-\frac{1}{2}\left[\frac{N_R-N_L}{N_R+N_L}\right]_{Z=-a},$$

N_R = measured counting rate for right-handed photons, and N_L = measured counting rate for left-handed photons. The two terms in brackets in the expression for V are measured at the positions for the converter of $Z=a$ and $Z=-a$, respectively.

At 15.3 GeV the polarization is essentially zero or very small due to the influence of a nearby depolarizing machine resonance. At 15.2 GeV, however, the electron beam is polarized up to about $(40\pm10)\%$. So far the polarization has been detected under certain beam conditions when beam-beam interactions were not present. The aim of the future measuring program will be to investigate the polarization as a function of those machine parameters which are decisive for the effect.

To summarize this section one can say that in the first three years of operation of PETRA the energy range has been from 12 to 36.7 GeV and that it has run reliably with very few failures. The stability of the machine was the major reason why all the groups at PETRA have been able to perform their experiments satisfactorily.

III. THE PETRA EXPERIMENTS

A. Physics objectives

Some of the prime physics goals of the experiments are as follows:

(1) To study the various QED processes shown in Fig. 5(a) and (b), and to study the universality of the known charged leptons in their electromagnetic interactions. At PETRA the maximum available c.m. energy at the moment is $\sqrt{s}=36.7$ GeV (q^2 up to 1350 GeV^2). Since first-order QED processes exhibit a $1/s$ cross-section dependence, one can probe the validity of QED with a sensitivity an order of magnitude greater than previously available in earlier colliding beam experiments performed at storage rings at SLAC, DESY, ADONE, and CEA in the range of $q^2\lesssim 50$ GeV^2.

(2) To measure the charge asymmetry expected from the interference of weak and electromagnetic interactions in the production of $\mu^+\mu^-$ pairs. As shown in Fig. 6, diagrams in which either a virtual photon is exchanged or a Z^0 vector boson is exchanged contribute to $\mu^+\mu^-$

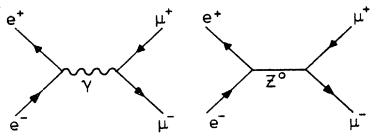

FIG. 6. First-order electromagnetic and weak processes contributing to the reaction $e^+e^-\rightarrow\mu^+\mu^-$.

production. The interference can be understood in terms of a variety of models based on the weak interaction Lagrangian

$$L_{\text{int}} = i\bar{\mu}\gamma^r(g_V - g_A\gamma^5)\mu Z_r .$$

In the simple $V-A$ model, for example, one assumes $g_V = g_A = g$, and $g^2/M_Z{}^2 = G/\sqrt{2}$, and G is the Fermi coupling constant. In the now standard Glashow-Weinberg-Salam (GWS) model (Glashow, 1961; Weinberg, 1967, 1972; Salam, 1968) the couplings are expressed in terms of the single parameter θ_W, the Weinberg angle:

$$g_V = \tfrac{1}{4}g\cos\theta_W(3\tan^2\theta_W - 1) ,$$

and

$$g_A = \tfrac{1}{4}g\sec\theta_W .$$

In order to distinguish between theoretical hypotheses, we can use the forward-backward charge asymmetry

$$A \equiv \frac{\sigma^- - \sigma^+}{\sigma^- - \sigma^+} ,$$

where σ_- (σ_+) corresponds to the cross section for events which have the μ^- (μ^+) appearing in the forward hemisphere. At $\sqrt{s} = 30$ GeV, with a total time-integrated luminosity of 10^{38} cm^{-2}, one obtains $\sim 10^4$ events in a 4π detector, leading to a 10 standard deviation asymmetry effect in the $V-A$ model and a 5 standard deviation effect in the GWS model.

One notes that before the direct observation of the Z^0, the precise determination of the charge asymmetry arising from weak-electronmagnetic interference is the most important verification of the idea of the unified electromagnetic and weak theory.

(3) To test models of the electroweak interaction with the QED processes shown in Fig. 5(a). At the highest PETRA energies the weak interaction's effects become noticeable and limits on the vector and axial-vector coupling constants can be obtained in a model independent way. Models of the weak interaction with a larger symmetry group than the standard GWS model can be tested and the two neutral boson masses which appear in those models can be restricted.

(4) To study the photon-photon scattering process as shown in Fig. 7. The theoretical work on this subject started in the nineteen thirties (Landau and Lifschitz,

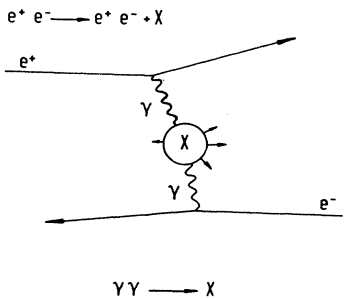

FIG. 7. The two-photon mechanism in an e^+e^- interaction.

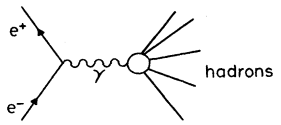

FIG. 8. The reaction $e^+e^- \rightarrow$ hadrons in lowest order.

1934; Euler and Kockel, 1953), and it was revived in the sixties (Low, 1960; Calogero and Zemack, 1960; Arteago-Roméro *et al.*, 1969; Jaccarini *et al.*, 1970) and early seventies (Balakin *et al.*, 1970; Brodsky *et al.*, 1970, 1971; Terazawa, 1973). The first events were observed at ADONE (Paoluzi *et al.*,1974), and later some measurements were obtained at DORIS (Besch *et al.*, 1979) and SPEAR (Abrams *et al.*, 1979). Since the advent of PETRA the two-photon exchange channels $\gamma\gamma \rightarrow$hadrons can be studied in a systematic way with a number of events compatible with the number obtained from the single-photon annihilation.

(5) To measure the total hadronic cross section (Fig. 8) and thereby the structure and energy dependence of the total cross section, in order to search for new thresholds in the hadronic final-state continuum, and to search directly for more J-like particles which appear as sharp resonances.

(6) To search for new quark flavors by studying the shape distributions of the hadronic events without and with inclusive muons [Fig. 9(a)].

(7) Using the distributions of the μe, μh, and hh final states shown in Fig. 9(b) to search for the existence of new charged leptons heavier than the τ.

(8) To study the topology of hadronic events by measuring the direction and energy of charged and neutral particles. In particular, at PETRA energies, the fragmentation of hard gluons emitted in association with quark-antiquark pairs leads to the creation of additional gluons and quarks, resulting in the production of multijet events. Study of the properties of these jets enables one to make a direct comparison with the predictions of QCD (Gross *et al.*, 1973; Politzer, 1973; Ellis *et al.*, 1976; DeGrand *et al.*, 1977; Kramer *et al.*, 1978; De Rujula *et al.*, 1978; Hoyer *et al.*, 1979; Ali, Körner *et al.*, 1979; Ali *et al.*, 1979). The rate of three-jet events rela-

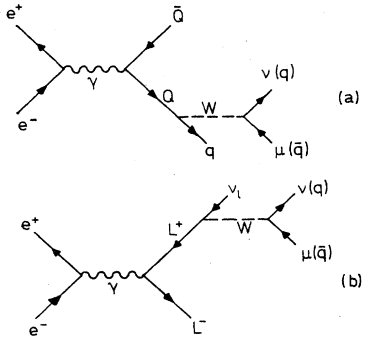

FIG. 9. (a) Diagram for production and decay of heavy quarks in e^+e^- annihilation. (b) Diagram for production and decay of heavy leptons in e^+e^- annihilation.

TABLE I. Main characteristics of the track detectors.

	Radius in meters	Length in meters	B field in kG	Photon detection	$\sigma(r,\phi)$ in microns
PLUTO	0.70	1.0	17.0	Shower counters	~1000
CELLO	0.80	4.0	13.0	Liquid argon	210
JADE	1.00	3.6	5.0	Lead glass	180
TASSO	1.35	4.5	5.0	Liquid argon plus shower counters	220

tive to two-jet events is a direct measure of the strong-interaction coupling constant α_s.

B. The detectors

The collaborations which built the five large detectors for the experiments at PETRA are CELLO: DESY-Karlsruhe-Munchen-ORSAY-Paris-SACLAY; JADE: DESY - Hamburg - Heidelberg - Lancaster - Manchester-Rutherford-Tokyo; MARK-J: Aachen-DESY-MIT-NIKHEF-Peking; PLUTO: Aachen-DESY-Hamburg-Bergen-Maryland-Siegen-Wuppertal; TASSO: Aachen-Bonn - DESY - Hamburg - London - Oxford - Rutherford-Weiszmann-Wisconsin.

Table I summarizes the main characteristics of the four track detectors CELLO, JADE, PLUTO, and TASSO. The radius of the cylindrical chambers with the magnetic fields of the solenoids and the various detection

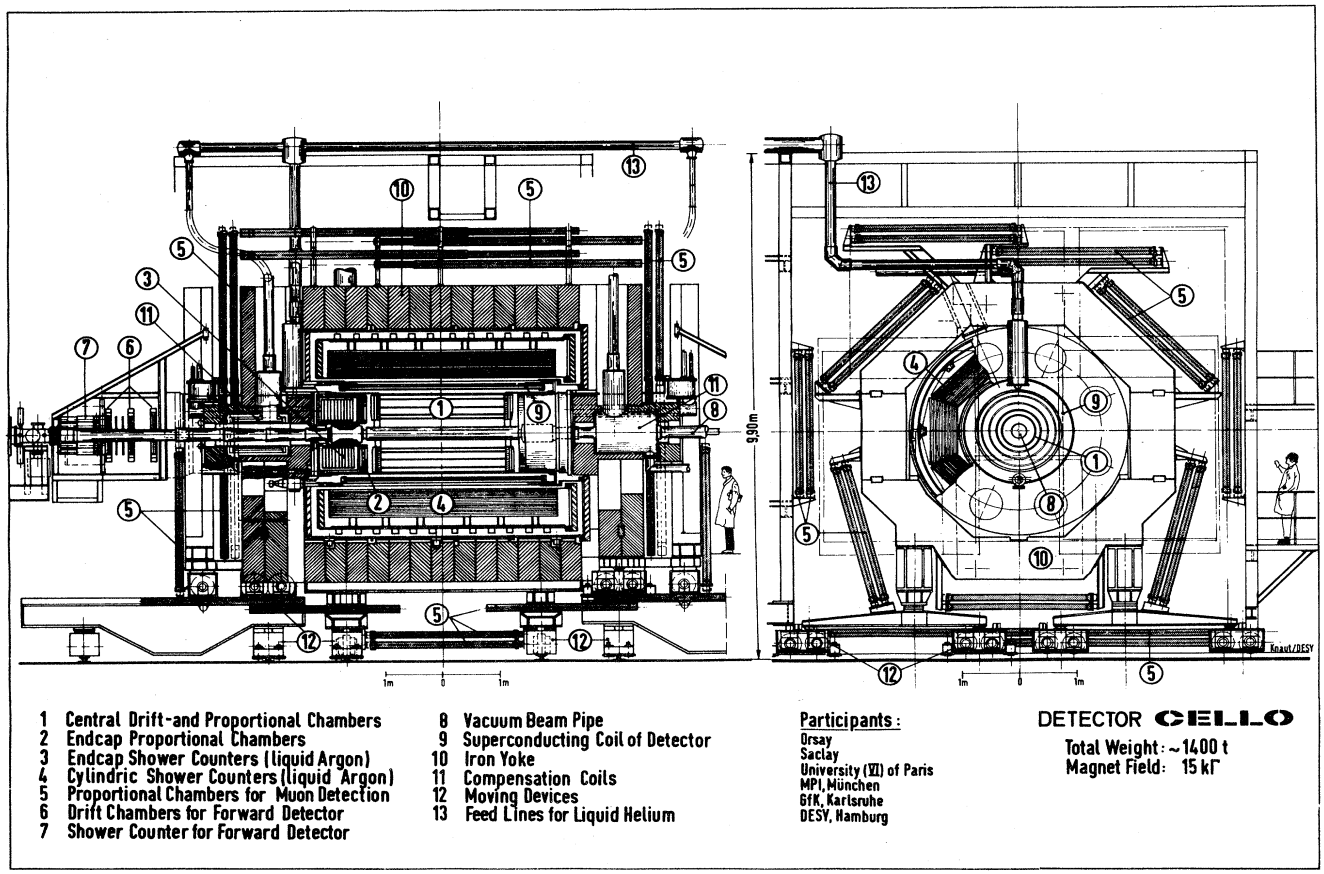

FIG. 10. The CELLO detector.

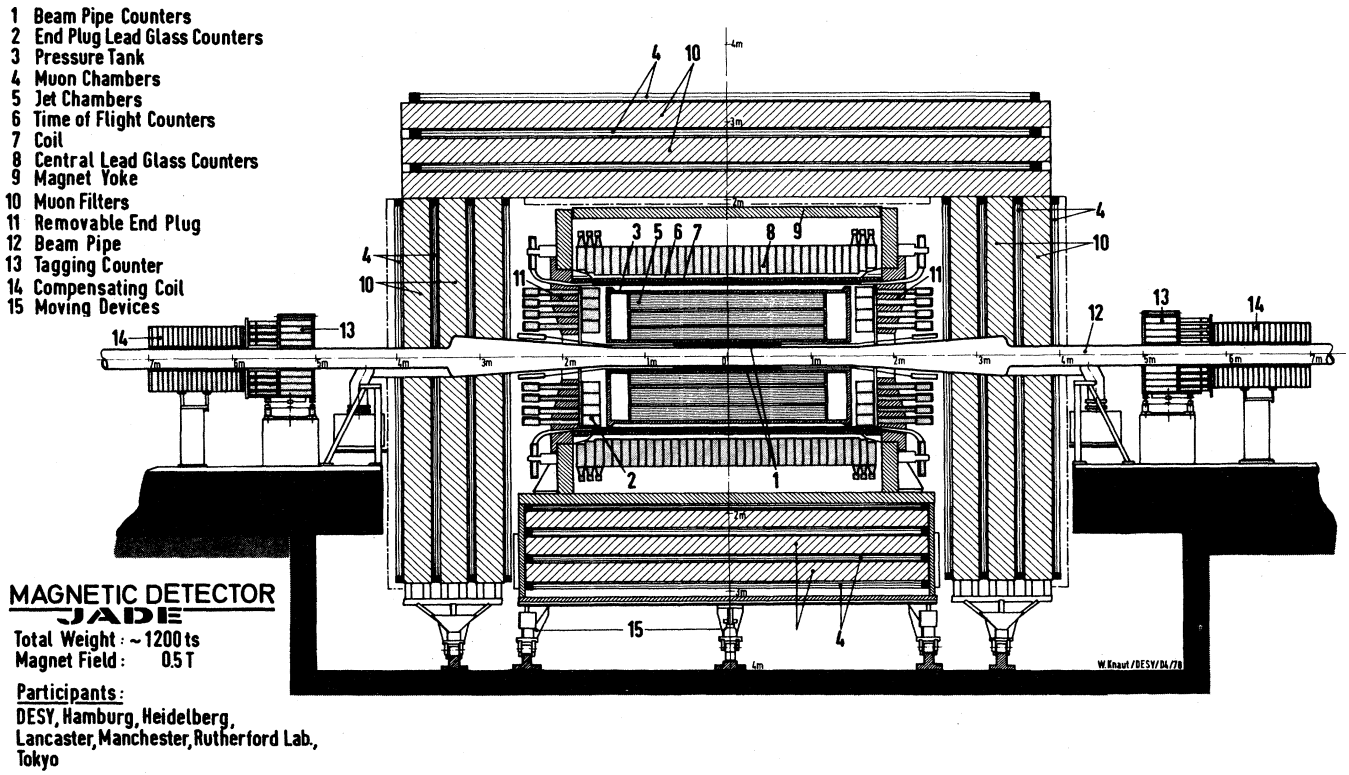

FIG. 11. The JADE detector.

devices for the energy measurements of photons and electrons are given. The setting errors obtained for the charged tracks are listed in the last column (for detailed descriptions of these detectors see Behrend *et al.*, CELLO, 1981c; Drumm *et al.*, JADE, 1980; Barber *et al.*, MARK-J, 1980b; Criegee and Knies, PLUTO, 1981; Burkhardt *et al.*, TASSO, 1981).

The momentum resolution $\Delta p/p$ of a charged track measured in a central track detector is given by the Glueckstern formula:

$$\frac{\Delta p}{p}=\frac{3.3\times 10^3}{BL^2}\sigma\left[\frac{720}{N+5}\right]^{1/2}p\ ,$$

where p is the momentum of the charged track in GeV/c, B the magnetic field in kG, L the track length in the detector in cm, σ the setting error in cm, and N the number of measurements along the charged track. Multiple scattering is neglected in this formula.

The CELLO detector (Fig. 10) was moved into the beam in the fall of 1979 replacing PLUTO. A thin superconducting coil (0.5 radiation lengths thick) provides an ~13 kG solenoidal magnetic field. The inner detector measuring the trajectories of charged particles consists of separate concentric cylindrical packages containing a total of 12 layers of proportional and drift chambers. The solid angle covered by this part of the detector is 87% of 4π. The r and ϕ measurements of the cylindrical chambers are complemented by $r-z$ measurements along the charged tracks using the information from cathode strips running at 90° and 30° relative to the beam direction. The coil is surrounded by a lead-liquid argon electromagnetic calorimeter consisting of 16 modules and supplemented by two symmetric end-cap modules. Each of the 16 modules is a stack of 41 layers of ~20 radiation lengths thick. The information of the shower development is obtained from two−cm strips running at 0°, 90°, and 45° to the beam direction. The resolution for electrons at 18 GeV is found to be 3%. The inner detectors are surrounded by the iron return yoke followed by large drift chambers to identify and measure muon tracks.

The JADE detector is shown in Fig. 11. It has a conventional coil producing a field of 5 kG. The cylindrical drift chamber is pressurized to increase the track resolution and to measure the energy loss dE/dX of a charged track in the gas. Forty-eight dE/dX samples along the track are measured and provide a means to identify particles in certain momentum regions. The coil is surrounded by about 2700 lead glass blocks (12.5 radiation lengths thick) to measure the electromagnetic showers. Time-of-flight counters inside the coil and outside and a muon-detector array of loaded concrete interleaved with drift chambers complete the setup. Figure 12 shows the visible energy as measured by the JADE detector as function of the momentum imbalance. In Fig. 12(b) the visible energy is plotted. The two-photon annihilation events from the reaction $e^+e^-\rightarrow e^+e^-+$ hadrons cluster at low visible energy and are well separated from the hadron events caused by the e^+e^- annihilation.

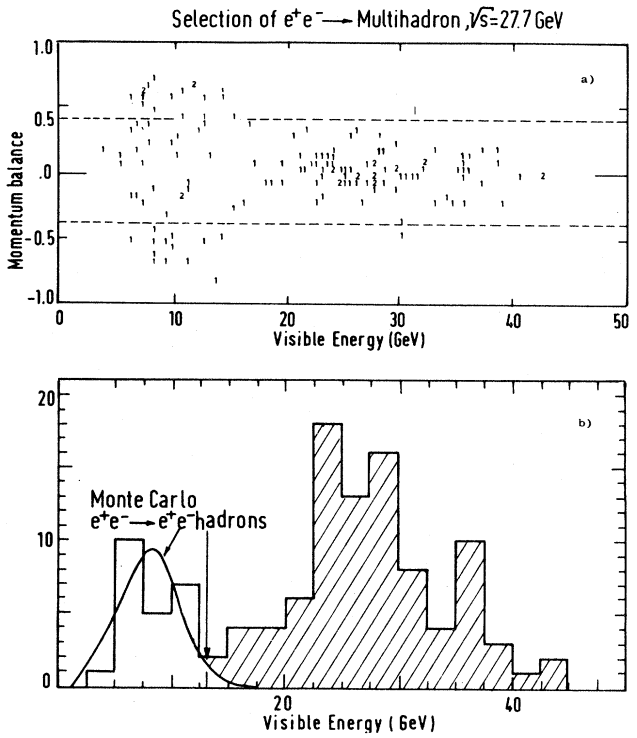

FIG. 12. (a) The visible energy (charged tracks and neutral electromagnetic energy as measured by the JADE detector) plotted as a function of the momentum balance. (b) The distribution of the visible energy as measured by the same detector. The solid line represents the prediction for photon-photon events of the process $e^+e^- \to e^+e^-$ hadrons. The hatched area contains the events of the process $e^+e^- \to$ hadrons.

The PLUTO detector (Fig. 13) consists of a superconducting coil which produces a magnetic field of 17 kG. A set of cylindrical proportional chambers detects the tracks of charged particles. Outside the iron flux return yoke proportional tube chambers are used to identify muons. An additional iron absorber outside the magnet yoke provides additional absorption length for the separation of the hadrons from the muons. The solid angle covered for the muon detection is 83% of 4π with a punch through and decay probability of less than 3% up to a muon momentum of 5 GeV.

To investigate the two-photon events, two forward spectrometers enable electron detection in the angular region between 23 and 250 mrad. Each spectrometer contains a small-angle tagger (SAT) covering the angular range up to 68 mrad. Finely segmented arrays of lead glass blocks and two sets of proportional chambers complete this part of the setup. The remaining part of the forward angular range is covered by the large-angle tagger (LAT) which uses a lead scintillator sandwich preceded by a layer of proportional tubes. The rms energy resolutions in the SAT and LAT are $8.4\%/\sqrt{E}$ and $11\%/\sqrt{E}$, respectively. Similar systems of forward spectrometers have been installed by the CELLO, JADE, and TASSO groups.

The TASSO detector is shown in Fig. 14. The central detector consists of a cylindrical drift chamber, time-of-flight system, magnet, liquid argon shower counters, and the top and bottom muon chambers. The conventional coil provides a solenoidal field of 5 kG. Inside this field is placed a large cylindrical drift chamber with 15 sense wire planes, nine radial and six with a stereo angle of $\pm 4°$. The single-wire resolution is 220 microns, yielding

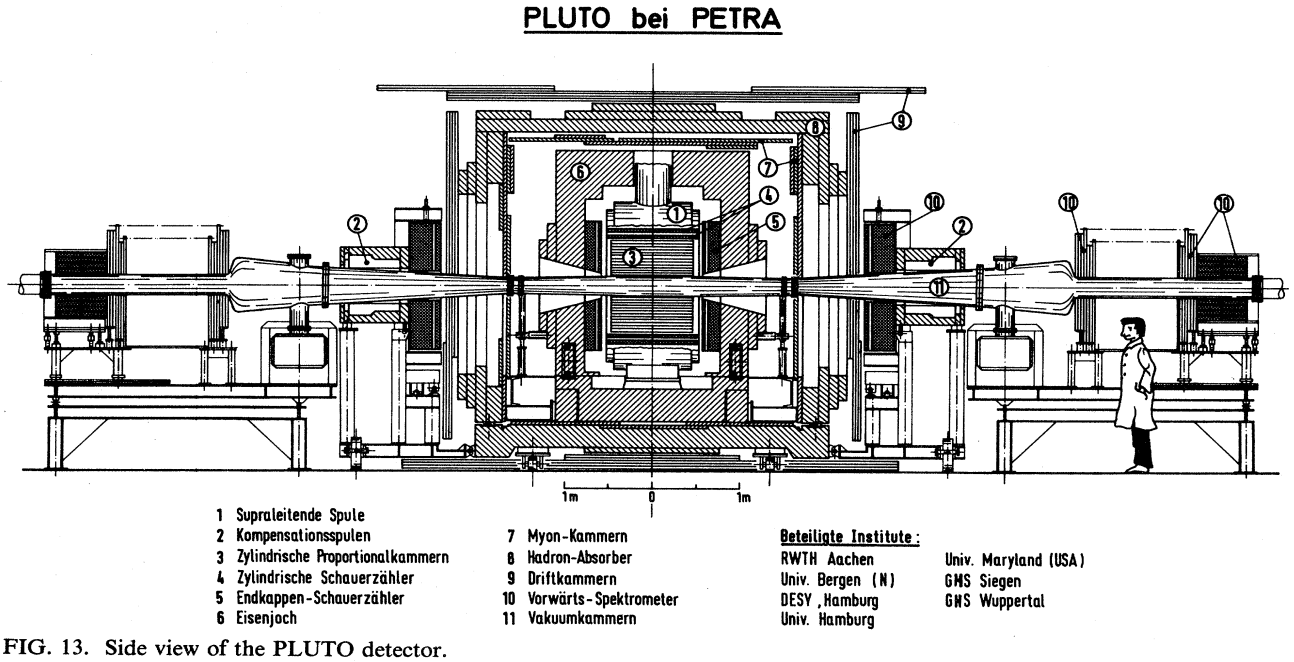

FIG. 13. Side view of the PLUTO detector.

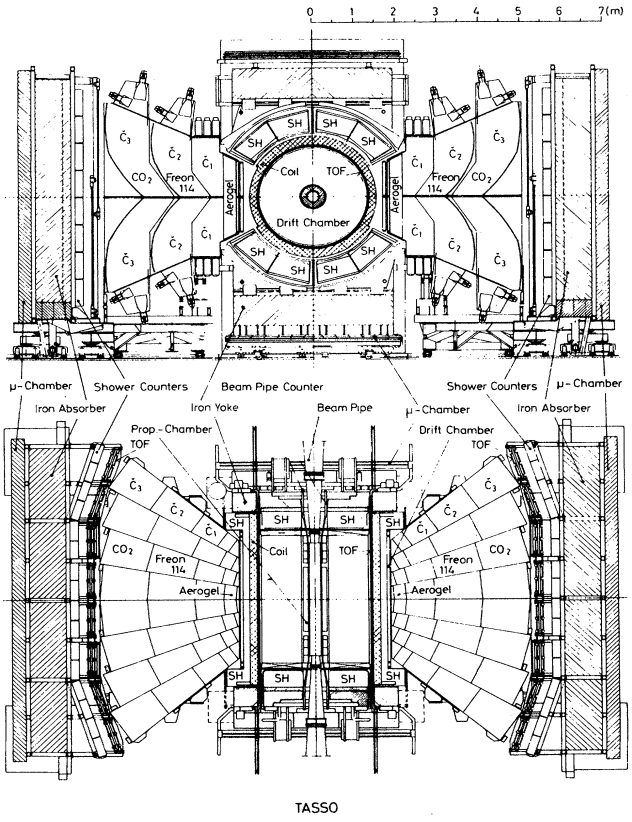

FIG. 14. End and top views of the TASSO detector.

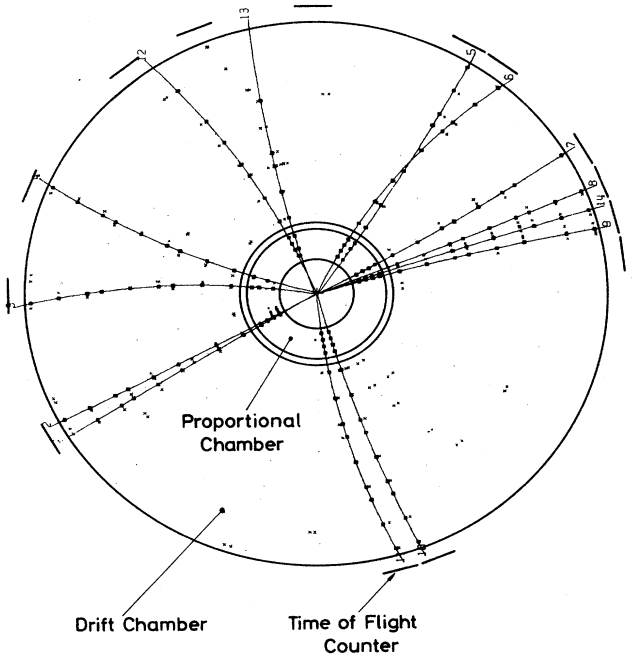

FIG. 15. A hadronic event at 35.8 GeV c.m. energy as seen by the central cylindrical chambers of the TASSO detector. The black points represent the wires which fired, the solid lines are the track reconstructions by the pattern-recognition program. Also indicated are the time-of-flight counters which were hit.

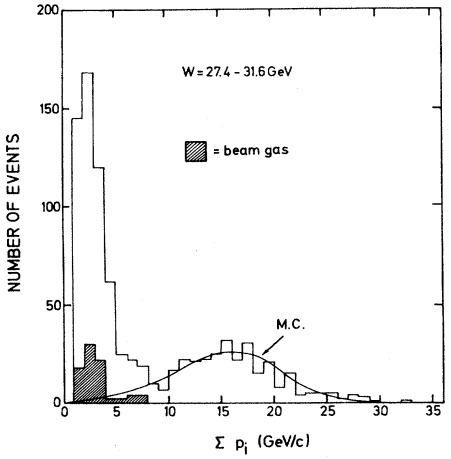

FIG. 16. Distribution of the total visible momentum of charged tracks from hadron events as measured by the TASSO detector. Beam-gas events are indicated by the hatched part of the histogram. The solid line is a Monte Carlo prediction for hadron production through one-photon annihilation in the $q\bar{q}$ model.

a momentum resolution of $\Delta p/p = 2\%\ p$ (p in GeV) for the muon tracks. A four-gap proportional chamber aids the pattern recognition and the z reconstruction.

Two spectrometer arms in the central region for detailed particle identification with three different Čerenkov counter systems followed by time-of-flight counters, shower counters, a hadron absorber, and muon chambers complete the detector. A hadron event as reconstructed by the TASSO pattern recognition program is displayed in Fig. 15. A total of 14 tracks is reconstructed for this particular event. In Fig. 16 the distribution of the sum of the momenta of the charged tracks for a sample of hadron events is plotted. Below 10 GeV the events are due to two-photon events. The background from beam-gas events in this region is small, as is indicated by the hatched part of the histogram. The solid line is a Monte Carlo prediction for the momentum distribution of hadronic events produced by the single-photon annihilation process and, as can be seen, the two-photon and single-photon events are readily separated.

The MARK-J detector is shown in Fig. 17. It is designed to distinguish charged hadrons, electrons, muons, and neutral hadrons, and photons and to measure their directions and energies. It covers a solid angle of $\phi = 2\pi$ and $\theta = 12°$ to $168°$ (θ is the polar and ϕ is the azimuthal angle). The detector, which consists of five magnetized iron toroids built around a nonmagnetic inner detector complemented by end caps, was designed to be insensitive to the effects of synchrotron radiation. The detector layer structure is best understood by referring to Fig. 18.

The beam pipe is surrounded by a four-layer inner track detector composed of 992 drift tubes. The tubes, which are arranged perpendicularly to the beam line, reconstruct the position of the event vertex along the beam line to an accuracy of 2 mm. The distribution of

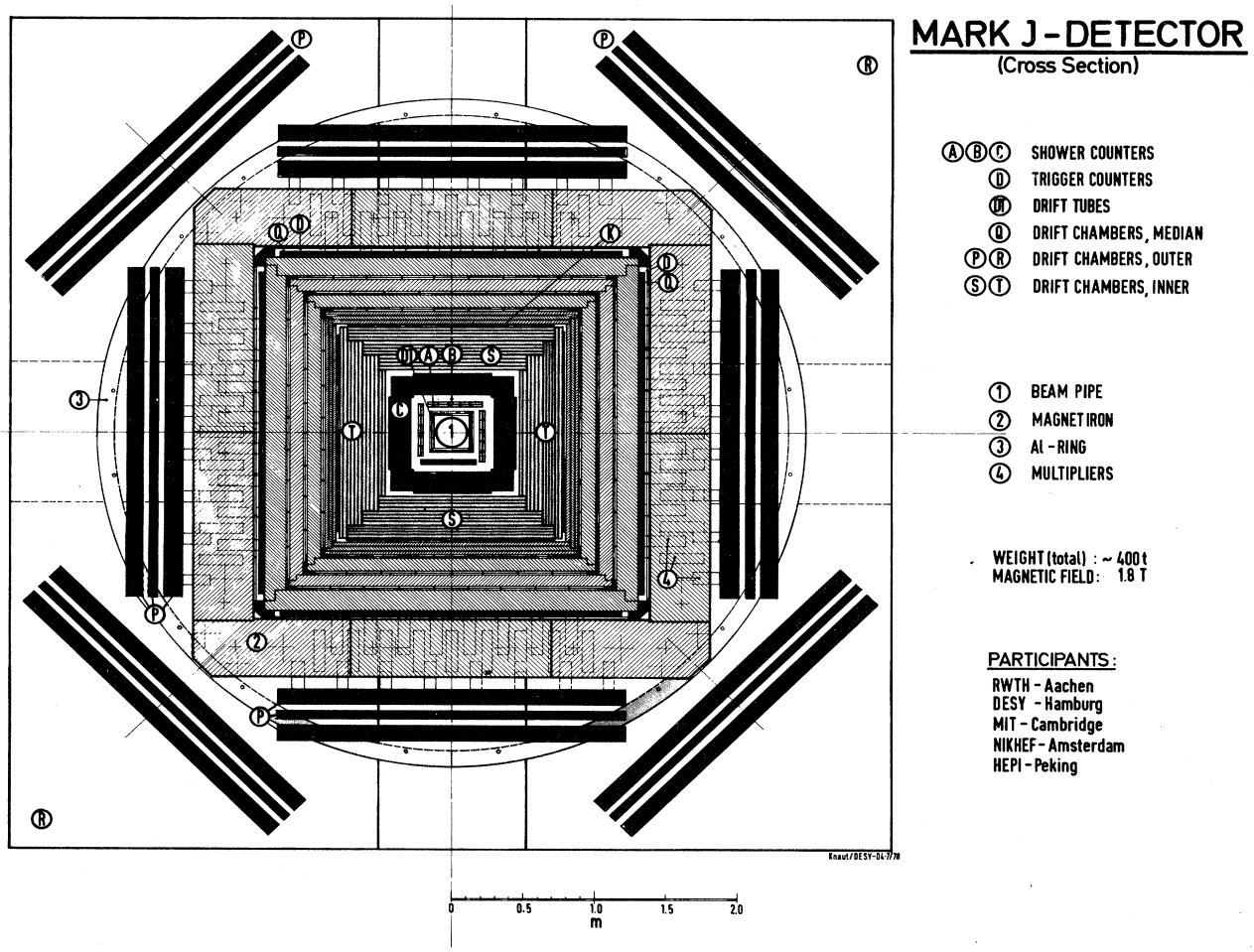

FIG. 17. The MARK-J detector in end view. Beam pipe (1), the drift tubes (DT), shower counters (A,B,C), inner drift chambers (S,T), calorimeter counters (K), outer drift chambers (Q,P,R), and magnetized iron (2).

event vertices obtained using the drift tubes is shown in Fig. 19. The observed rms width of 1.27 cm is compatible with that expected from the known bunch length of the machine.

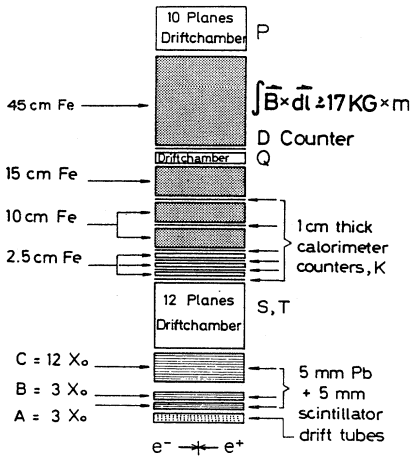

FIG. 18. The layer structure of the MARK-J detector as seen by a particle emerging from the interaction point at a right angle to the beam axis.

Particles then pass through 18 radiation lengths of shower counters used to identify and measure the energy of electrons, photons, and charged and neutral hadrons. This inner calorimeter is divided into three layers of shower counters (labeled A, B, and C in Fig. 17). Since every shower counter is viewed by one phototube at each end, the longitudinal (z) position of particle trajectories

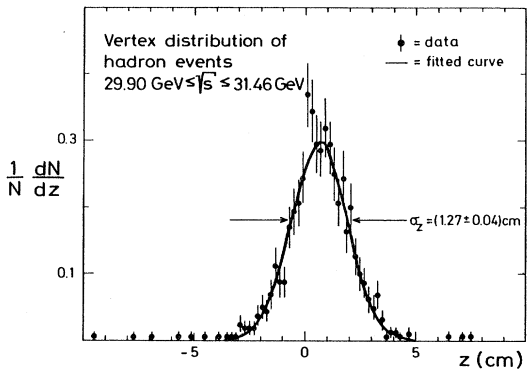

FIG. 19. Distribution of event vertices along the beam direction reconstructed using the drift tube tracks of the MARK-J detector.

can be determined by comparing the relative pulse heights from each end of the counter. Timing information provides another measure of the longitudinal position.

Twelve planes of drift chambers (labeled S and T) measure the angles of particles penetrating the inner electromagnetic calorimeter. The energy-sampling elements of the calorimeter K, shown in Fig. 17, are 192 scintillation counters arranged in four layers. The main body of the calorimeter is composed of the magnetized iron plates which are also used to momentum analyze muons. Hadrons penetrating the inner shower-counter layers, and secondary particles produced by hadronic showers initiated in the inner layers, deposit most of their remaining energy in the calorimeter K.

Muons are identified by their ability to penetrate the iron of the hadron calorimeter. The low-momentum cutoff is about 1.3 GeV/c at normal incidence. The initial muon trajectory is measured in the S and T chambers and in the drift tubes.

The bend angle and position of muons exiting from the calorimeter are measured in 10 planes of drift chambers, labeled R and P in Fig. 17. The total thickness of the iron is 87 cm, and it has a bending power of approximately 17 kG. The typical bend angle for a 15-GeV muon is 30 mrad.

An additional two layers of drift chambers (Q chambers) are situated amidst the iron layers to measure the muon tracks in the bending plane. Adjacent to these chambers are the 32 muon trigger counters marked (D) used to trigger on single- and multiple-muon events and to reject cosmic rays.

For hadronic events the rms resolution in the total observed energy is ~20% as can be seen in Fig. 20(a). From tracks reconstructed with the shower-counter layers the total missing energies in the directions parallel and perpendicular to the beam may be computed. The observed distributions of these quantities are shown in Figs. 20(b) and 20(c) for high-energy hadronic events.

C. Monte Carlo simulation

A large part of the analysis effort of the experimental groups is devoted to the development and use of Monte Carlo programs. This simulation of events proceeds in three steps:

(1) event generation,
(2) detector simulation, and
(3) event coding.

The event generators produce simulated events for a wide variety of e^+e^- reactions. The momenta, masses, charges, and spatial distribution of the final-state particles are generated according to the physics hypothesis appropriate to each process.

Hadron production by e^+e^- annihilation,

$$e^+e^- \rightarrow \text{hadrons} , \tag{1}$$

is treated in the framework of QCD, where the final-state hadrons are viewed as composite particles made up of quarks (and antiquarks) bound by a force mediated by gluons. Process (1) proceeds through the production of a quark-antiquark ($q\bar{q}$) pair, accompanied by the possible final-state radiation of one or two gluons (denoted by g or gg) or in rare cases by the production of an additional $q\bar{q}$ pair. The quarks and gluons then fragment, meaning that they pull additional $q\bar{q}$ pairs from the sea with limited P_t with respect to the quark gluon directions, forming jets of hadrons. Reaction (1) thus includes the following subprocesses:

$$e^+e^- \rightarrow q\bar{q} \rightarrow \text{hadrons} , \tag{1a}$$

$$e^+e^- \rightarrow q\bar{q}g \rightarrow \text{hadrons} , \tag{1b}$$

$$e^+e^- \rightarrow q\bar{q}gg \rightarrow \text{hadrons} , \tag{1c}$$

$$e^+e^- \rightarrow q\bar{q}q\bar{q} \rightarrow \text{hadrons} . \tag{1d}$$

As an example, Fig. 21 shows a $q\bar{q}g$ final state, accompanied by radiation of an initial-state photon, which leads to multijets. For the search for the existence of new heavy quark flavors such as the top quark t, the reaction

$$e^+e^- \rightarrow t\bar{t} \rightarrow \text{hadrons} \tag{1e}$$

is simulated as a special case of process (1a)–(1d).

Pair production of the charged leptons and two-photon production through the reactions

$$e^+e^- \rightarrow e^+e^- , \tag{2}$$

$$e^+e^- \rightarrow \mu^+\mu^- , \tag{3}$$

$$e^+e^- \rightarrow \tau^+\tau^- \rightarrow \text{hadrons and leptons} , \tag{4}$$

$$e^+e^- \rightarrow \gamma\gamma \tag{5}$$

is also simulated. The analysis of computer-generated final states for reactions (2)–(5) is a major part of the

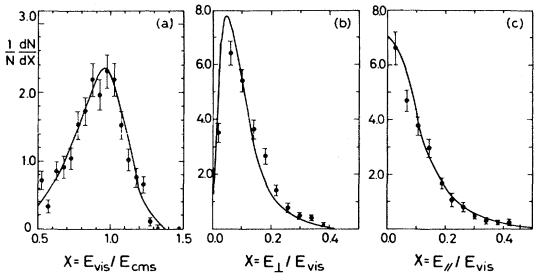

FIG. 20. Energy measurement at $\sqrt{s} = 30$ GeV. The solid lines are predictions of Monte Carlo computations. (a) Visible energy spectrum for hadronic events. (b) Energy imbalance $E_\perp$ in the direction transverse to the beam. (c) Energy imbalance $E_{||}$ in the beam direction.

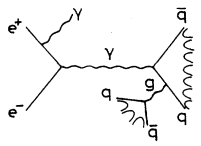

FIG. 21. Gluon bremsstrahlung from the final state of e^+e^- annihilation into quark-antiquark pairs.

QED tests discussed in Sec. IV.A. Other processes simulated include the "two-photon processes"

$$e^+e^- \rightarrow e^+e^-e^+e^- , \tag{6}$$

$$e^+e^- \rightarrow e^+e^-\mu^+\mu^- , \tag{7}$$

and

$$e^+e^- \rightarrow e^+e^- + \text{hadrons} . \tag{8}$$

Event types (1a)—(1e) are generated in most cases using a slightly modified version of the computer program implemented by Ali, *et al.* (1980b), which provides a detailed model of hadron production by e^+e^- annihilation in the framework of QCD. In general, $q\bar{q}$ pairs are produced in fractions proportional to the square of the quark charges for flavors up, down, strange, charm, and bottom (denoted u, d, s, c, and b, respectively). The fragmentation procedure used to transform quarks into hadrons is similar to that used by Feynman and Field (1978). The fragmentation functions used are $zD(z) = (1-z)^2$ for u, d, and s quarks and $zD(z) =$ constant for c and b quarks, where z represents the fraction of the quark momentum carried away by the hadron formed at each stage of the fragmentation process. Heavy quarks (c and b) are allowed to decay weakly according to the usual six-quark model (Kobayashi and Maskawa, 1973), and the light quarks produced in the decay sometimes fragment independently, forming additional jets. Since gluon fragmentation functions are unknown, gluons simply fragment to quark pairs, which in turn fragment according to the normal procedure. The $q\bar{q}g$ events in which hard noncollinear gluons are radiated (see Fig. 21) are generated according to the perturbative QCD matrix elements which include the effects of nonzero quark mass (Ali *et al.*, 1980b). Events of this type are required to have a thrust (Sec. VI.B.1) less than 0.95 before fragmentation in order to avoid the singularity for soft or collinear gluon emission. Checks are made to insure the results do not depend strongly on the value of this cut.

Events from the higher-order QCD processes $q\bar{q}gg$ and $q\bar{q}q\bar{q}$ are treated in a way similar to those from $q\bar{q}g$. The principal difference is that instead of applying the thrust cut, the requirement of acoplanarity greater than 0.05 is imposed, where acoplanarity is defined as

$$A = \min \sum |\mathbf{E}_i \cdot \mathbf{n}_3| / \sum |\mathbf{E}_i| ,$$

and $\mathbf{E}_i$ is the vector energy and $\mathbf{n}_3$ is chosen to minimize A. This implies that none of the four partons can be soft and that no two are collinear. It does, however, reject planar events which are not near a singularity in the matrix element. A $t\bar{t}$ generator (Ali *et al.*, 1980b), which proceeds in the same way as for other heavy quarks, is used to study the effects that will be useful in searching for the top quark. All of the first four event generators use a (QED) radiative correction generator (Mo *et al.*, 1969; Bonneau *et al.*, 1971; Tsai, 1974; Berends *et al.*, 1973a; 1973b, 1974).

Bhabha scattering, μ-pair production, τ-pair production, and $\gamma\gamma$ events are currently generated according to lowest-order distributions and radiative corrections are applied externally for the first three processes using the programs of Berends *et al.* (see Sec. IV). Two-photon event generation for $e^+ e^- \rightarrow e^+e^- e^+e^-$ and $e^+e^- \rightarrow e^+e^-\mu^+\mu^-$ is done using the program of Vermaseren (1980), which is exact to order α^4 in the cross section.

The output of the Monte Carlo generators is used by the detector simulation programs. This latter program proceeds for the MARK-J detector in the following way. Particles are tracked through the detector, and interaction points with counter and chamber planes are computed. The amount of energy in each counter hit is determined from tables that give the dependence on penetration depth, angle, and particle energy. Energy resolution and longitudinal shower fluctuations are also simulated using tabulated information. The above-mentioned tables were generated from the test beam data taken with electrons and pions at energies from 0.5 to 10 GeV, from experimental calorimeter studies (Sanders, 1974), and from shower Monte Carlo programs (Gabriel and Bishop, 1978).

Hits in the drift chamber and drift tubes are digitized. The chamber performance is simulated in detail including background, inefficiency, multiple hits, cross talk, and δ rays. The full chamber survey information is used as provided on an input file. The somewhat complicated drift distance versus drift time function is also reproduced.

Finally, the counter ADC and TDC information is digitized. Pulse heights are corrected for attenuation in the scintillator, and times are corrected for particle flight time, scintillation light transit time, and time slewing due to varying pulse height. Multiple hits are also treated.

To summarize, the detector is simulated in detail so that Monte Carlo events can be treated in the same way as actual data. To complete this process, the information described above is then coded into a form that resembles the raw data format. These events are stored on tape or disk so they may be read by the various analysis programs. This is useful for many purposes such as calculation of acceptance for a process, computation of background, and determination of detector effects on measured quantities. In particular, the MARK-J group uses Monte Carlo simulation and the appropriate event generator to produce expected distributions in variables that can be compared to data. Similar methods have been used by the other groups, taking into account the various components of their detectors.

D. Radiative corrections

The luminosity of PETRA in the intersections is monitored by measuring the rate of Bhabha events in the central detectors and the small-angle luminosity monitors. We assume that at present energies and small q^2 the absolute rate of the Bhabha scattering process is well described by QED and may thus be used as an absolute

monitor. The large q^2 Bhabha scattering covered by the central detectors as described in Sec. III.B is also well described by QED and can be used as an independent monitor. Nevertheless, care must be exercised to take proper account of radiative corrections which may be as large as 20% for some final-state configurations in, for example, the MARK-J detector.

The measured rate for Bhabha scattering [reaction (2)] receives contributions from all orders in the perturbation expansion of QED. Furthermore, given the finite energy and position resolution of the detector, some events in which a hard photon is radiated,

$$e^+e^-\rightarrow e^+e^-\gamma\,, \tag{9}$$

are also detected and attributed to Bhabha scattering.

It is therefore necessary to evaluate the contribution to the total Bhabha scattering cross section to order α^3. Higher-order corrections are difficult to compute and have not yet been calculated exactly. Fortunately, they are small, since the result of the α^3 correction is already only a few percent.

The calculations described below were first carried out by Berends *et al.* (1974), and the most recent version of their computer program is used by several of the groups. The cross section for Bhabha scattering can be written as

$$d\sigma/d\Omega = d\sigma_0/d\Omega(1+\delta\{\theta,\phi\})\,,$$

where $d\sigma_0/d\Omega$ is the lowest-order (α^2) cross section and δ represents the radiative correction to order α^3. Following their notation, we write

$$\delta=\delta_b+\delta_v\,,$$

where δ_b is due to real bremsstrahlung and receives contributions from the eight diagrams in Fig. 22(a) and δ_v is due to virtual bremsstrahlung, which is the contribution of the interference between the lowest-order diagrams and the diagrams in which one closed loop occurs (due to virtual photons, virtual electron-positron pairs, $\mu^+\mu^-$ or $\tau^+\tau^-$ pairs) shown in Fig. 22(b).

Renormalization removes the ultraviolet divergence of δ_v, and one is left with an infrared divergence which is exactly canceled by the infrared divergence occurring in δ_b; δ is then finite.

A further correction which could have been included in δ_v is the hadron contribution to vacuum polarization. It can be thought of as quark-antiquark loops occurring in the photon propagator and is similar to lepton loops. Those contributions have been calculated (Berends and Komen, 1976) using experimental knowledge of R, the ratio of the cross section for $e^+e^-\rightarrow$hadrons to the cross section of the pointlike process $e^+e^-\rightarrow\mu^+\mu^-$.

At 90° with respect to the beam axis the contribution from quark loops to δ is of the order of $+4\%$ at $\sqrt{s}=17$ GeV and slowly increases with energy. The procedure followed by the MARK-J group is described in some detail in the next paragraphs. The other PETRA groups use similar calculations in determining the radiative corrections.

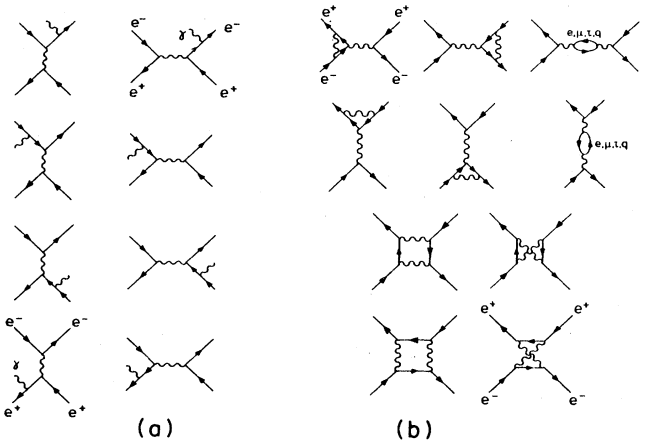

FIG. 22. Radiative diagrams for the process $e^+e^-\rightarrow e^+e^-$.

1. Small-angle radiative corrections

The radiative corrections for the small-angle Bhabha scattering require careful treatment since the differential cross section is strongly peaked in this region. Ripken (1979) has overcome the technical difficulties of numerical computation in the small-angle region by using Gaussian integration techniques, and he has applied his program to the case of the MARK-J using a matrix element provided by Berends. At angles smaller than 5° with respect to the beam axis, all electron, muon, and τ loop diagrams and the hadronic contribution to vacuum polarization are small and neglected.

In the small-angle luminosity monitoring stations of the MARK-J detector pairs comprising one small scintillator and one opposite large scintillator define the acceptance. The geometry of these counters has been incorporated into the radiative corrections in the following fashion. For the hard-photon part of the cross section electron-positron-photon triplets are generated where one of the leptons is within the acceptance of a small scintillator and the other lepton is required to pass within the boundaries of the large scintillator diametrically opposite. The soft-photon part is incorporated analytically. These corrections are very sensitive to the relative position of the small scintillator with respect to the larger one. The residual uncertainty in the positions of the scintillators contributes a relative systematic error in the calculation of δ of about 30%. Since the value of δ is -8%, the radiative corrections contribute an error of 2.5% to the total luminosity measured in the small-angle monitor.

2. Large-angle radiative corrections

For large-angle Bhabha scattering the phase space for real bremsstrahlung can be experimentally characterized by two simple boundaries: $E_{\rm th}$, an energy threshold for the outgoing electron and positron, and ξ, a limit on the angle in space between the electron direction and the direction at 180° to the positron direction (acollinearity cut).

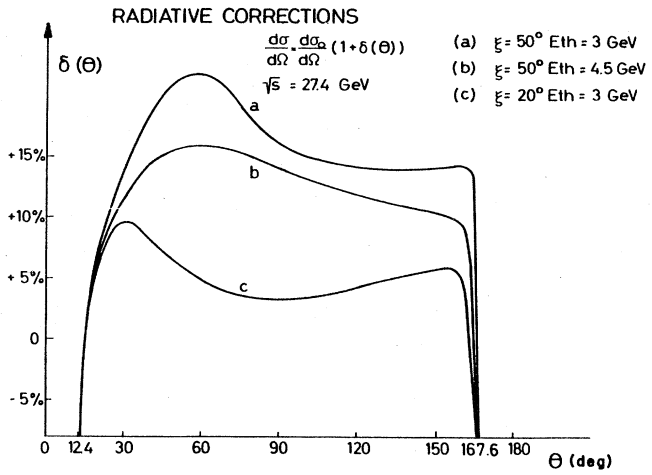

FIG. 23. Radiative corrections δ as a function of the scattering angle θ for different acceptance cuts for the central part of the MARK-J detector.

Figure 23 shows δ plotted as a function of θ over the A counter acceptance at $\sqrt{s}=27.4$ GeV for various combinations of the cuts.

With the knowledge of δ one may integrate the differential cross section over the detector acceptance to find the Bhabha rate expected in the central detector.

One finds that the luminosity measurement with the central detector agrees within ~3% with the measurement made with the small-angle luminosity counters (see Fig. 24). As will be described in Sec. IV.D, precise knowledge of the overall normalization plays an important role in the g_V and g_A determinations because the weak interaction modifications of QED predictions are small.

An experimental check on the calculations of the radiative corrections is the distribution of the measured angle ξ compared with the QED prediction. In Fig. 25 the acollinearity angle for ξ for the MARK-J data for the Bhabha events is shown. The agreement between the measurements and the calculations (Berends and Kleiss, 1981) is good. The JADE data for the same angular distribution are shown in Fig. 26, and here also the agreement over a wide range of acollinearity angles (up to 120°) between the data and the QED predictions is very good.

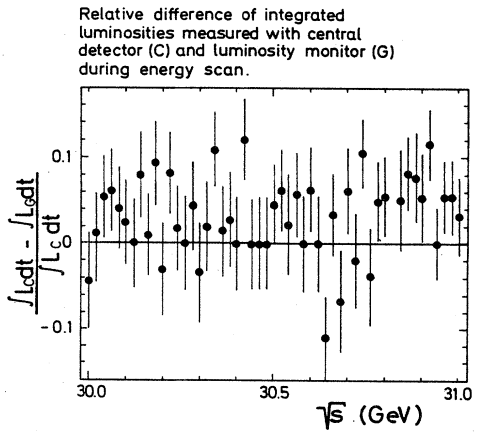

FIG. 24. Luminosity measured with the central MARK-J detector (L_c) and with the luminosity monitor (L_G) during energy scans.

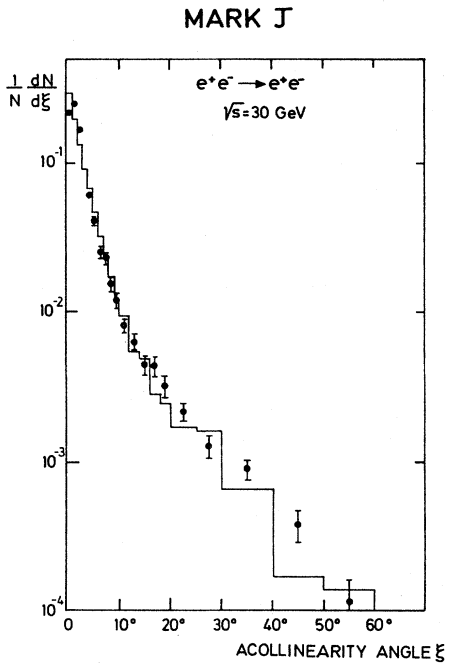

FIG. 25. Acollinearity distribution for Bhabha scattering events observed in the central detector of the MARK-J detector. The data are compared to the prediction of QED (Berends and Kleiss, 1981).

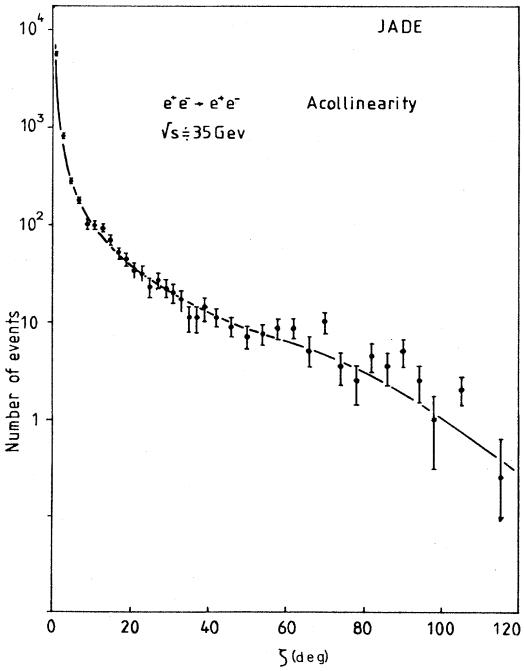

FIG. 26. Acollinearity distribution for Babha scattering events observed in the JADE detector. The data are compared to the prediction of QED.

TABLE II. Resolution and detector type employed by the experiments for various QED processes. Resolution at $E_{beam}=15$ GeV.

	$e^+e^-\to e^+e^-$, $e^+e^-\to\gamma\gamma$ Shower detector					$e^+e^-\to\mu^+\mu^-$		
	$\Delta p/p$	$\Delta E/E$	L_R	Material	$\Delta\theta$	$\Delta p/p$	Magnet	Absorber
JADE	60%	3.8%	12.5	Pb-glass	0.6°	50%	Solenoid 0.5 T	Concrete $L_A=6$
MARK-J		10%	18	Pb/scint.	3°	26%	Fe toroid	Fe (magn.) ≥ 87 cm
PLUTO	90%	5–9%	10.6 8.6	Pb/scint.	1–1.4°	45%	Solenoid 1.7 T	Fe 105 cm
TASSO	30%	14–18%	9	Pb/scint.	~15°	30%	Solenoid 0.5 T	Fe 50–87 cm

IV. TESTS OF QED, UNIVERSALITY OF CHARGED LEPTONS, AND MODELS OF THE ELECTROWEAK INTERACTION

A. Introduction

There have been many experiments testing QED with electrons, muons, and photons at electron-positron storage rings (Alles-Borelli *et al.*, 1972; Newman *et al.*, 1974; Augustin *et al.*, 1975; O'Neill *et al.*, 1976). For a comprehensive review of QED work, see Brodsky and Drell (1970). Much has been learned about the properties of the heavy-lepton τ since the original search began at ADONE on $e^+ + e^- \to \mu e + \cdots$ (Bernardini *et al.*, 1973; Orito *et al.*, 1974). The discovery of the τ lepton at SLAC (Perl *et al.*, 1975; Feldman *et al.*, 1977) and its subsequent confirmation at DESY (Burmester *et al.*, 1977a,b) have inspired further studies. We know it is a spin-$\frac{1}{2}$ particle which decays weakly (Fluegge, 1979a; Brandelik, 1980b) and whose properties are very similar to the muon.

With the PETRA experiments the reactions $e^+ + e^- \to l^+ l^-$ for all the known charged leptons ($l = e, \mu, \tau$) are studied by measuring the cross section as a function of the scattering angle over a wide range of PETRA energies. These measurements enable one to compare the data with predictions of quantum electrodynamics, to test the universality of these leptons at very small distances, and to set a limit on the charge radius of these particles. Up to the present time the reactions

$$e^+e^- \to e^+e^- \text{ (Bhabha scattering)}, \tag{2}$$

$$e^+e^- \to \mu^+\mu^-, \tag{3}$$

$$e^+e^- \to \tau^+\tau^-, \tag{4}$$

have been measured in the range of $\sqrt{s}=12$ to 36.7 GeV.

The fermion-pair-production processes $e^+e^- \to F + \bar{F}$, where the $F\bar{F}$ pair stands for either a lepton pair (e^+e^-, $\mu^+\mu^-$, and $\tau^+\tau^-$) or quark-antiquark pairs, proceed via the exchange of a virtual photon. At sufficiently high energies, however, the Z^0 exchange effects have to be taken into account. One of the aims of the e^+e^- experiments at the highest machine energies is to detect weak effects due to this exchange.

The analysis of the weak effects is performed in two ways:

(a) The $\sin^2\theta_W$ is determined within the context of the standard model of Glashow, Weinberg, and Salam, using all the available data of the production of fermion-antifermion pairs.

(b) A model-independent analysis is presented for the determination of the weak neutral current coupling con-

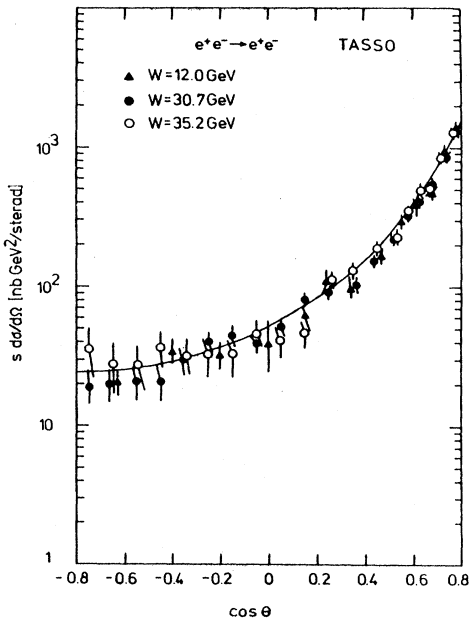

FIG. 27. The differential cross section $s\,d\sigma/d\cos\theta$ for $e^+e^-\to e^+e^-$ at $\sqrt{s}=12$, 30.7, and 35.2 GeV obtained by the TASSO collaboration.

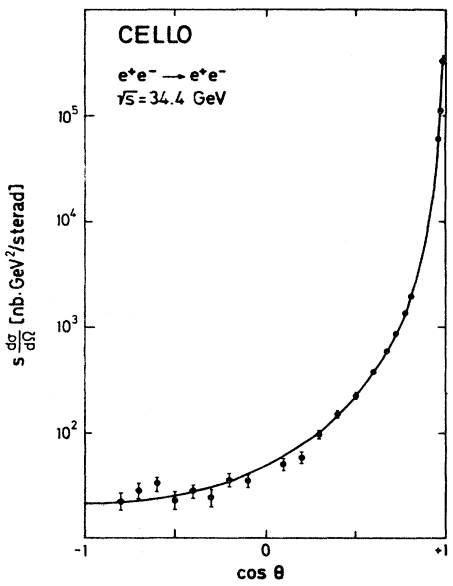

FIG. 28. The differential cross section $s\,d\sigma/d\Omega$ for $e^+e^-\to e^+e^-$ at $\sqrt{s}=36.5$ GeV obtained by the CELLO collaboration.

stants using the data of the lepton-pair-production processes alone.

Furthermore, the data are also compared with extended gauge models containing more than one neutral weak boson. Stringent lower limits can be placed on the masses of such bosons.

Certain results described in this section were presented by Böhm at the Wisconsin High-Energy Physics Conference (Böhm, 1980).

B. Tests of QED and universality of leptons

The momentum, energy, and angular resolution for the QED processes

$$e^+e^-\to e^+e^-\,, \tag{2}$$

$$e^+e^-\to\mu^+\mu^-\,, \tag{3}$$

$$e^+e^-\to\tau^+\tau^-\,, \tag{4}$$

$$e^+e^-\to\gamma\gamma \tag{5}$$

are shown in Table II for the various experiments.

(a) The first-order QED photon propagator produces an s^{-1} dependence in the $e^+e^-\to e^+e^-$ cross section. Thus when radiative corrections have been taken into account in the data, the quantity

$$s\frac{d\sigma}{d\Omega}$$

should be independent of s. This distribution is plotted for the TASSO data at $\sqrt{s}=12$, 30.7, and 35.2 GeV in Fig. 27. Data for the Bhabha events at $\sqrt{s}=34.4$ GeV from the CELLO group (Behrend *et al.*, 1981a) are shown in Fig. 28. Excellent agreement with the QED predictions is seen in both figures.

To express this agreement analytically, the data are compared with the QED cross section in the following form (Hofstadter, 1975):

$$\frac{d\sigma}{d\Omega}=\frac{\alpha^2}{s}\left[\frac{q'^4+s^2}{q^4}|F_s|^2+\frac{2q'^4}{q^2s}R_e(F_sF_T^*)+\frac{q'^4+q^4}{s^2}|F_T|^2\right][1+C(\theta)]\,, \tag{10}$$

where

$$F_s=1\mp q^2/(q^2-\Lambda_\pm^2) \tag{11}$$

is the form factor of the spacelike photon,

$$F_T=1\mp s/(s-\Lambda_\pm^2) \tag{12}$$

is the form of the timelike photon, $q^2=-s\cos^2(\theta/2)$, $q'^2=-s\sin^2(\theta/2)$, Λ is the cutoff parameter in the modified photon-propagator model (Drell, 1958; Lee and Wick, 1970) and $C(\theta)$ is the radiative correction term as a function of θ. The lower limits of Λ at a 95% confidence level for the Bhabha events are shown in Table III for various PETRA groups (CELLO, Behrend *et al.*, 1981a; JADE, Bartel *et al.*, 1980c; MARK-J, Barber *et al.*, 1979a,f, 1980d; PLUTO, Berger *et al.*, 1980c, g; TASSO, Brandelik *et al.*, 1980b,d). One can conclude from this table that QED is valid for reaction (2) down to small distances.

TABLE III. Lower limits of cutoff parameters Λ (in GeV) at 95% C.L. for various QED processes.

	$\gamma\gamma$		e^+e^-		$\mu^+\mu^-$		$\tau^+\tau^-$	
	Λ_+	Λ_-	Λ_+	Λ_-	Λ_+	Λ_-	Λ_+	Λ_-
CELLO	43	48	83	155				
JADE	50	52	118	138	146	126	111	93
MARK-J	51	49	106	193	194	153	126	116
PLUTO	46	46	80	234	107	101	79	63
TASSO	34	42	150	136	80	118	88	103

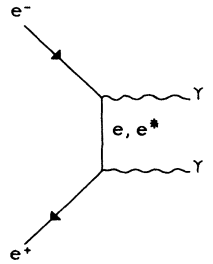

FIG. 29. Diagram for the process $e^+e^-\to\gamma\gamma$. The e^* indicates the diagram for the exchange of a heavy electron.

(b) The two-photon annihilation $e^+e^-\to\gamma\gamma$ (Fig. 29) is well suited for testing the validity of QED at high energies, since the contributions from electroweak interference effects are expected to be absent in first-order perturbation theory (Capdequi-Peyranere *et al.*, 1978). Two possible modifications of the standard QED cross section can be used:

(i) A vertex modification (Kroll, 1966; Ringhofer and Salecker, 1975) which modifies the differential cross section as

$$\frac{d\sigma}{d\Omega}=\frac{\alpha^2}{2s}\left[\frac{q'^2}{q^2}|F(q^2)|^2+\frac{q^2}{q'^2}|F(q'^2)|^2\right][1+C(\theta)]\,, \tag{13}$$

where

$$F(q^2)=1\pm q^4/\Lambda^4\,,$$

$$F(q'^2)=1\pm q'^4/\Lambda^4\,,$$

and q^2 and q'^2 are defined as above. The $C(\theta)$ is the radiative correction as a function of the scatter angle θ.

(ii) To test exchange of a hypothetical heavy electron the differential cross section can be written as (Litke, 1970)

$$\frac{d\sigma_{e^*}}{d\Omega}=\frac{\alpha^2}{2s}\left[\frac{q'^2}{q^2}+\frac{q^2}{q'^2}\pm\frac{2s^2-4q^2q'^2}{\Lambda^4_{e^*_\pm}}\right][1+C(\theta)]\,. \tag{14}$$

The value of $\Lambda_{e^*_\pm}$ can be interpreted as the mass of a heavy electron assuming its coupling strength is the same as that of the electron (see Fig. 29).

Figure 30 shows the angular distribution normalized with the predicted QED cross sections for $e^+e^-\to\gamma\gamma$ obtained by the five PETRA groups in the energy range $27.4<\sqrt{s}<36.7$ GeV (Dittmann and Hepp, 1981). The agreement between the data and the QED expectation (dashed line in the figure) is good. The data were fitted to above expressions (13) and (14) of the differential cross section. The results of these fits for the cutoff parameters are collected in Table III. The lower limits for the cutoff parameters are about 50 GeV (95% C.L.). At the highest PETRA energies the lower bounds are raised by a factor 4 to 5 over the values obtained with the lower energy e^+e^- colliding beam machines (Bacci *et al.*, 1971; Hanson *et al.*, 1973; Beron *et al.*, 1974; Hilger *et al.*, 1977).

The integrated cross section over the measured angular range of the PLUTO detector is shown in Fig. 31 as function of the c.m. energy $E_{\text{c.m.}}$ in order to check the $1/s$ behavior of the $e^+e^-\to\gamma\gamma$ reaction. The agreement between the data and the QED predictions is good.

To conclude, a heavy electron with a mass smaller than $\sim$50 GeV is ruled out by the measurements. It is interesting to note that the ratio of the excited electron mass over the electron mass is greater than 10^5, while the excited proton—the Δ, for example—is very close in mass to the proton.

The PETRA detectors are able to distinguish muons from electrons and hadrons and to eliminate cosmic-ray muons as a source of background for the back-to-back muon pairs.

I will describe in detail the criteria used by the MARK-J collaboration for the μ- and τ-pair-production identification (Barber *et al.*, 1979f; 1980d). Single

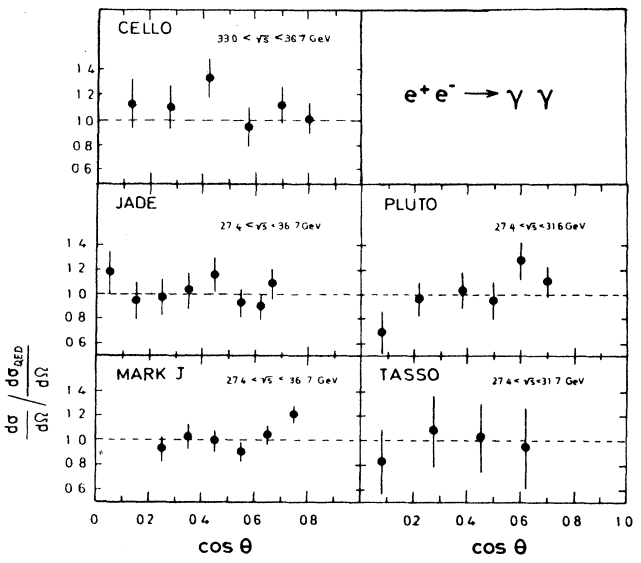

FIG. 30. The differential cross section normalized with the QED cross section as a function of $\cos\theta$ for the process $e^+e^-\to\gamma\gamma$.

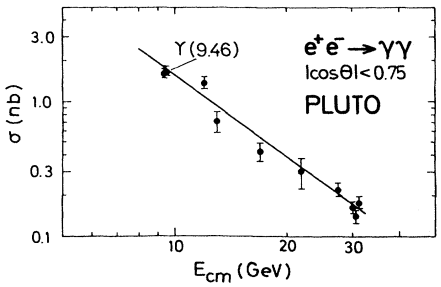

FIG. 31. The cross section for reaction $e^+e^-\to\gamma\gamma$ for $|\cos\theta|\leq 0.75$. The curve is the QED prediction including the effects of radiation and angular resolution.

muons are identified as particles which

(i) are reconstructed in the inner drift chambers to come from the interaction region;

(ii) leave minimum ionizing pulse heights in the seven layers of counters of the calorimeter; and

(iii) leave a track in the outer drift chamber (P) and thus fall into an angular range $45° \leq \theta_\mu \leq 135°$.

In addition, back-to-back muon pairs from reaction (3) are distinguished from cosmic rays by the requirements that

(i) the D counter timing signals be coincident with one another (and not relatively off time as in the case for cosmic rays traversing the detector), and

(ii) the muons be collinear and coplanar and pass through the intersection region.

A Monte Carlo study shows that $\mu^+\mu^-$ acceptance, which is dominated by the geometrical acceptance of the outer drift chambers, is $41\% \pm 3\%$ independent of beam energy. τ leptons from reaction (4) are identified by detecting μ-hadron and μ-electron final states. The cross section is determined using the known branching ratio of $\tau \to \mu\nu\nu$ (16%) and $\tau \to (e$, hadron, or multihadrons$) + \nu$ (84%) (Fluegge, 1979a; Brandelik *et al.*, 1980b). The measured muon momentum and hadron energy for the $\tau^+\tau^-$ candidates are in agreement with calculations based on the known decay properties of the τ lepton.

The acceptance is calculated using a Monte Carlo method to generate $\tau^+\tau^-$ production from reaction (4) including radiative corrections. A detection efficiency of $\sim 10\%$ for τ pairs at various energies, when requiring one decay muon to be detected in association with a single electron, or one or more hadrons, is obtained with the MARK-J detector.

The selection criteria for the τ leptons for the PLUTO (Fluegge, 1979b) and TASSO (Brandelik *et al.*, 1980b) groups are different from the ones mentioned above. PLUTO identifies one charged particle and neutrals recoiling against one or more charged particles for the decay of the τ, and TASSO requires at least three charged and neutral particles, recoiling against one charged particle.

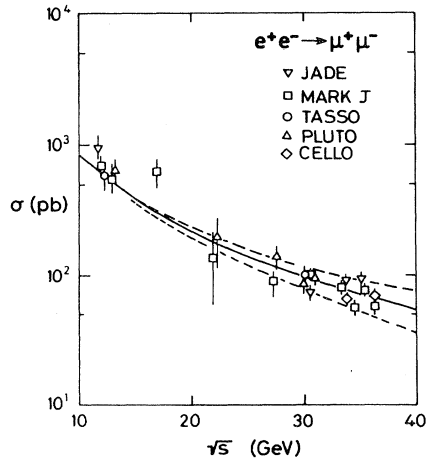

FIG. 32. Observed cross section for the reaction $e^+e^- \to \mu^+\mu^-$ compared to the predictions of QED (solid curve). The dotted curves are the QED cross sections modified by cutoff parameters $\Lambda_\pm = 100$ GeV.

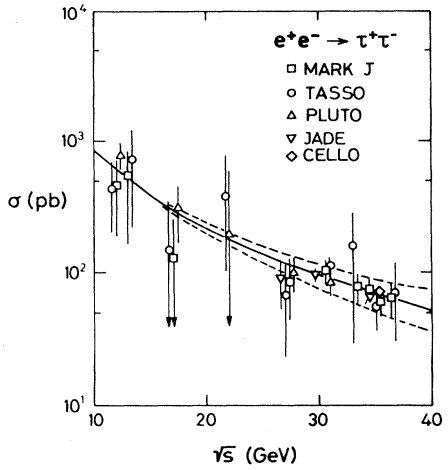

FIG. 33. Observed cross section for the reaction $e^+e^- \to \tau^+\tau^-$ compared to the predictions of QED (solid curve). The dotted curves are the QED cross sections modified by cutoff parameters $\Lambda_\pm = 100$ GeV.

The CELLO group uses essentially the same criteria as those used by the PLUTO collaboration, including one charged particle recoiling against one other charged particle. The muon pairs and the Bhabha events are removed from their τ sample.

The resultant $e^+e^- \to \mu^+\mu^-$ and $\tau^+\tau^-$ cross sections as a function of $\sqrt{s}$ are plotted in Figs. 32 and 33. We see that from $q^2 = s = 169$ to $q^2 = 1225$ GeV^2 the data agree well with the predictions of QED for the production of a pair of pointlike particles. In particular, Fig. 33 represents the evidence that the τ lepton is a pointlike particle over a large range of q^2, and demonstrates that it belongs in the same family as the electron and muon. To parametrize the maximum permissible size (radius) of the particles, one uses the form factor

$$F(s) = 1 \mp s/(s - \Lambda_\pm^2) .$$

By comparing the data with the cross sections including this form factor, one can calculate lower limits on the cutoff parameters at the 95% confidence level. These limits are summarized in Table III.

Thus, from Heisenberg's uncertainty principle, all the known charged leptons are pointlike particles in their electromagnetic interactions, with characteristic radii $\leq 10^{-16}$ cm.

C. Measurements of the asymmetry in the production of $\mu^+\mu^-$ pairs

Within the framework of the standard GWS model the differential μ-pair cross sections can be written as

$$\frac{d\sigma}{d\Omega} = \frac{\alpha^2}{4s}[(B+1)(1+\cos^2\theta) + A\cos\theta] ,$$

where

$$B = 8sgg_V{}^2 \frac{M_Z{}^2}{s - M_Z{}^2} + 16s^2g^2(g_V{}^2 + g_A{}^2)\left[\frac{M_Z{}^2}{s - M_Z{}^2}\right]^2,$$

$$A = 16sgg_A{}^2 \frac{M_Z{}^2}{s - M_Z{}^2} + 128s^2g^2g_V{}^2g_A{}^2\left[\frac{M_Z{}^2}{s - M_Z{}^2}\right]^2,$$

$$g = \frac{G_F}{8\sqrt{2}\pi\alpha} = 4.49 \times 10^{-5}\ \text{GeV}^{-2},$$

and g_A and g_V are the axial end vector coupling constants of the neutral weak current. In the standard model $g_A = 0.5$ and g_V is related to $\sin^2\theta_W$ according to $g_V = (1 - 4\sin^2\theta_W)$.

The term B is for a value of $\sin^2\theta_W = 0.23$ at $\sqrt{s} = 35$ GeV very small ($B \sim 3.5 \times 10^{-3}$). As a result the change in the total muon pair cross section due to weak effects is not noticeable at PETRA energies. As the term $A = -0.26$, at $\sqrt{s} = 35$ GeV the asymmetry effect becomes detectable. Defining θ as the angle between the incident e^- and the outgoing muon in the forward hemisphere, the asymmetry is

$$A_{\mu\mu} = \frac{N_- - N_+}{N_- + N_+},$$

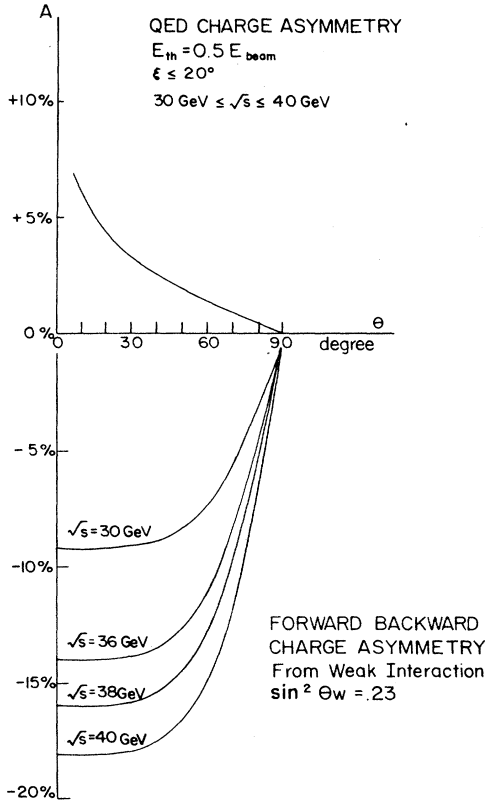

FIG. 34. The calculated asymmetries due to QED and weak effects as a function of the scattering angle θ for various energies. The weak effects are calculated within the standard model using $\sin^2\theta_W = 0.23$.

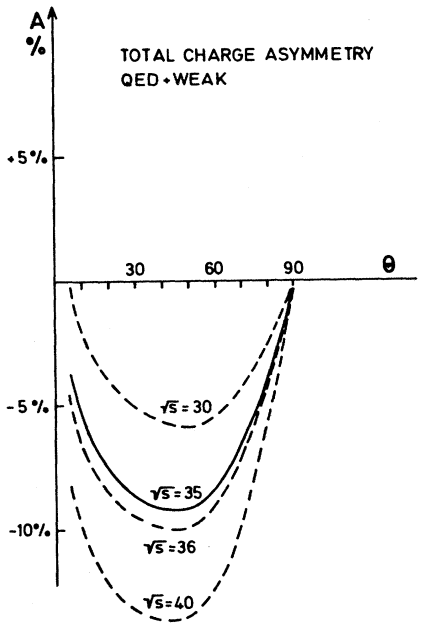

FIG. 35. The total asymmetry due to QED and weak effects as a function of θ for different energies.

where N_- (N_+) is the corrected number of events with the negatively (positively) charged muon in the forward hemisphere, integrated over the accessable angular range.

In first order $A_{\mu\mu}$ is directly related to $g_A{}^2$ according to

$$A_{\mu\mu} = 6gg_A{}^2 s \frac{M_Z{}^2}{s - M_Z{}^2}.$$

Due to the propagator term $M_Z{}^2/(s - M_Z{}^2)$ the asymmetry is negative below the Z^0. A positive asymmetry is, however, introduced by the interference between QED loop diagrams ($C = +1$) and the first-order annihilation amplitude ($C = -1$).

In Fig. 34 the asymmetries due to the QED and weak effects are plotted (Revol, 1981) separately as functions of

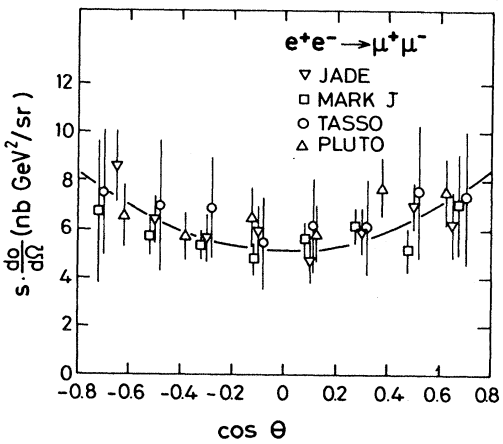

FIG. 36. The $\cos\theta$ distributions as measured by the PETRA experiments for muon pair production. The solid line is the $1 + \cos^2\theta$ expectation.

TABLE IV. The values for the muon asymmetry for the various experiments. The expected values from the GWS model are also given.

	JADE	MARK II	MARK-J	PLUTO	TASSO
$A_{\mu\mu}$%	-11 ± 4	-4.7 ± 4.2	-3 ± 4	7 ± 10	-11.3 ± 5.0
Expected	-7.8	-4.0	-7.1	-5.8	-8.7

the scattering angle θ. Due to bremsstrahlung effects, cuts are introduced on the energy of the muons and the acollinearity angle (ζ) between them. The energy variation for the QED asymmetry is very small (within the thickness of the line). The weak effects show a considerable energy dependence, and this effect is linear in s. In Fig. 35 the sum of QED and weak asymmetry is plotted as a function of θ. It has to be noted that in all practical cases the experiments do not measure muons below a scattering angle θ of 30°. The statistics so far do not allow measuring the asymmetry as a function of θ at different energies and the measurements for $A_{\mu\mu}$ are integrated over the available θ range.

The PETRA results for the $\cos\theta$ distribution (Pohl, 1981; Branson, 1981) are summarized in Fig. 36 and Table IV. The asymmetry averaged over the four experiments is

$$A_{\mu\mu}=(-7.7\pm2.4)\% ,$$

while -7.8% is expected. The value for the axial-vector coupling obtained from this average is

$$|g_A|=0.50^{+0.07}_{-0.09} .$$

D. Tests of electroweak interaction models with one neutral boson

1. Measurement of $\sin^2\theta_W$

The theory of Glashow-Weinberg-Salam is characterized by a parameter denoted $\sin^2\theta_W$. Neutrino-nucleon scattering experiments (Langacker *et al.*, 1979; Liede and Roos, 1979; Sakurai, 1979; Sehgal, 1979), which yield a value of $\sin^2\theta_W=0.234\pm0.011$, are characterized by the following experimental conditions:

(a) Relatively low c.m. energy, namely, $s\sim300$ GeV^2;

(b) Relatively low momentum transfer $q^2\sim-100$ GeV^2 in the spacelike region; and

(c) Use of nuclear targets.

At several e^+e^- machines complementary experiments have been performed measuring electroweak parameters from the reactions

$$e^++e^-\rightarrow(\gamma+Z^0)\rightarrow l^+l^- \quad (l=e,\mu,\tau) \tag{15}$$

and

$$e^++e^-\rightarrow(\gamma+Z^0)\rightarrow\text{hadrons} , \tag{16}$$

where the production of final-state leptons and hadrons is via both virtual photons (γ) and neutral intermediate vector bosons (Z^0).

In comparison with neutrino experiments, these experiments have the following unique properties:

(a) High c.m. energy, namely, $s\sim1300$ GeV^2;

(b) Most data at the large-momentum transfer $q^2\sim1300$ GeV^2 and in both the spacelike and the timelike region; and

(c) Purely pointlike particles in the initial state. In the framework of the parton model, the present neutrino experiments are viewed as lepton scattering on u and d quarks, whereas at PETRA one uses either purely leptonic reactions such as in reaction (15) or a mixture of five quarks with substantial contributions from the heavy c and b quarks as in reaction (16). First we will look at the derivation of $\sin^2\theta_W$ with the lepton pair data.

The measurements consist of the already discussed data on μ and τ pair production. In addition, the measurements of the angular distribution of the Bhabha scattering events are used. In Fig. 37 the available $e^+e^-\rightarrow e^+e^-$ data (Dittmann and Hepp, 1981) at the highest PETRA energies are shown. The differential cross section $d\sigma/d\Omega$ is normalized with the first-order QED cross section $d\sigma_{QED}/d\Omega$ and is plotted as a function of $\cos\theta$.

The results of the determination of $\sin^2\theta_W$ are summarized in Table V. The values obtained range from 0.23 to 0.25 for the different experiments. As no deviations

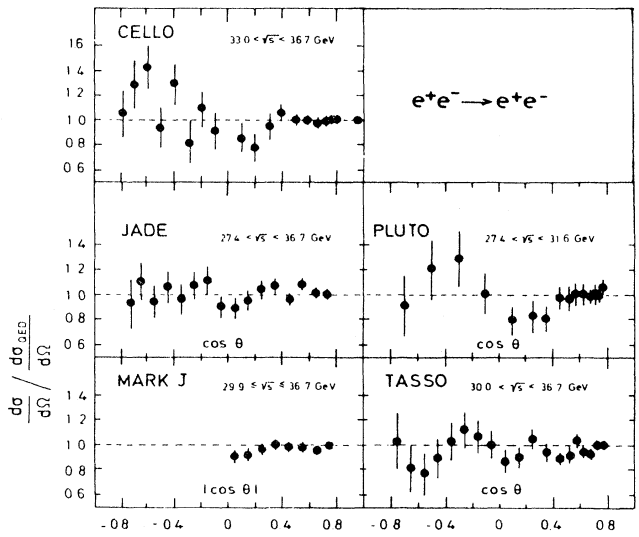

FIG. 37. The differential Bhabha cross sections $d\sigma/d\Omega$ normalized with the pointlike QED cross section. The dashed lines are the expected distribution from QED.

TABLE V. The values for $\sin^2\theta_W$ obtained by the various experiments.

	$\sin^2\theta_W$	Leptons
CELLO	$0.22^{+0.15}_{-0.10}$	e^+e^-, $\tau^+\tau^-$, $A_{\mu\mu}$
JADE	0.25 ± 0.15	e^+e^-, $\mu^+\mu^-$, $A_{\mu\mu}$
MARK-J	0.25 ± 0.11	e^+e^-, $\mu^+\mu^-$, $\tau^+\tau^-$, $A_{\mu\mu}$
PLUTO	0.23 ± 0.17	e^+e^-, $\mu^+\mu^-$
TASSO	0.25 ± 0.10	e^+e^-, $\mu^+\mu^-$, $A_{\mu\mu}$

are seen from QED so far (see Table III for the cutoff parameters for $e^+e^-\to e^+e^-$), the values for $\sin^2\theta_W$ naturally fall into this region, as the smallest effects are expected at $\sin^2\theta_W=0.25$.

The next step is to use the hadron data to determine $\sin^2\theta_W$. In reaction (16) above, if one takes weak neutral-current effects into account, one can write the hadronic cross section as (Ellis and Gaillard, 1976)

$$R_f=\frac{\sigma(e^+e^-\to\gamma,Z^0\to f\bar{f})}{\sigma_p}$$

$$=Q_f{}^2-8sQ_f\cdot g_V\cdot g_{V_f}\cdot p(s)$$

$$+16s^2g^2(g_V{}^2+g_A{}^2)(g_{V_f}{}^2+g_{A_f}{}^2)\cdot p'(s)\ ,$$

where $\sigma_p=4\pi\alpha^2/3s$ is the pointlike QED cross section, Q_f=charge of the final-state quark f, g_{V_f} and g_{A_f} are the weak vector and axial-vector coupling constants of quark f, and $g=4.47\times10^{-5}$ GeV^{-2} is related to the Fermi coupling constant. Additionally,

$$p(s)=\left[\left(\frac{s}{m_Z{}^2}-1\right)+\frac{\Gamma_Z{}^2}{s-m_Z{}^2}\right]^{-1}$$

for γ and Z^0 interference ,

and

$$p'(s)=\left[\left(\frac{s}{m_Z{}^2}-1\right)^2+\frac{\Gamma_Z{}^2}{m_Z{}^2}\right]^{-1}$$

for pure Z^0 exchange .

In the framework of the GWS model, assuming e-μ universality, the weak coupling constants are given by

$$g_{V_f}=T^L_{3f}-2Q_f\sin^2\theta_W\ ,$$

$$g_{A_f}=T^L_{3f}\ ,$$

where T^L_{3f} is the weak isospin of the left-handed quark. The mass of the Z^0 can be expressed as

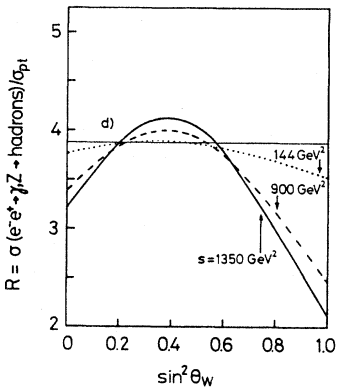

FIG. 38. The variation of the total cross section R with s and $\sin^2\theta_W$ as predicted by the GSW model. The horizontal line at $R=3.87$ corresponds to γ exchange only.

$m_z=37.28/\sin\theta_W\cos\theta_W$ GeV, and the width is taken to be constant: $\Gamma_Z=2.3$ GeV.

The electroweak hadronic cross section R_T is given in the quark model by the incoherent sum over all final-state quarks, including a color factor of 3 and QCD corrections (Chetyrkin *et al.*, 1979; Dine and Sapierstein, 1979; Celmaster and Gousalves, 1980).

$$R_T=3\cdot\Sigma_f R_f\left[1+\frac{\alpha_s(s)}{\pi}+(1.98-0.115\cdot N_f)\frac{\alpha_s^2(s)}{\pi^2}\right],$$

where α_s is the coupling constant of the strong interaction, which has been measured at PETRA energies to be 0.18 for $\sqrt{s}$ in the 30–36 GeV range (Barber *et al.*, 1979d, g; Bartel *et al.*, 1980a; Berger *et al.*, 1979d; Brandelik *et al.*, 1979b, 1980e), and which changes slowly with energy. $N_f=5$ is the number of different quark flavors.

Figure 38 shows the dependence of R on $\sin^2\theta_W$ for different values of the center-of-mass energy squared s (Bartel *et al.*, 1981e).

The measurement of R of the JADE collaboration is ~4. At the highest PETRA energy ($s=1350$ GeV^2) large deviations are expected for values of $\sin^2\theta_W$ at ~0

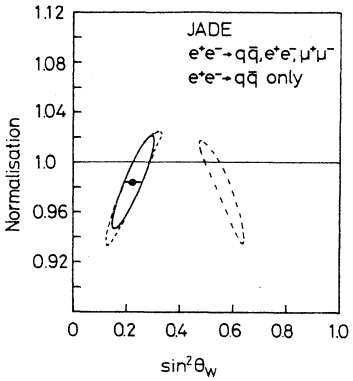

FIG. 39. The logarithm-likelihood function contour (68% C.L.) in the $\sin^2\theta_W$ normalization plane. The dashed curves show the solution from the fit to the hadron data; the solid curve is the solution for the combined data.

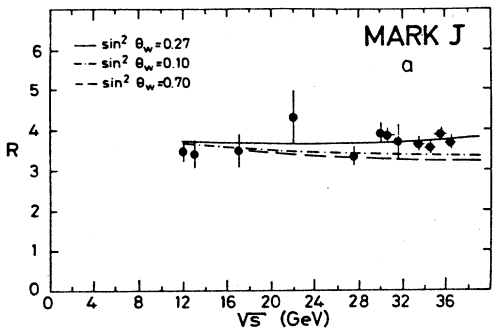

FIG. 40. Experimental results on R with statistical errors as a function of c.m. energy $\sqrt{s}$. The solid line shows the theoretical prediction R_T for the best fit to the data ($\sin^2\theta_W=0.27$ using $\alpha_s=0.18$ at $\sqrt{s}=30$ GeV). The dependence of R_T on $\sin^2\theta_W$ is also shown for two extreme values ($\sin^2\theta_W=0.70$ and 0.10).

and ~ 1. The solid curve intersects the value of R at $\sin^2\theta_W \sim 0.2$ and ~ 0.55. As the systematic error in the determination of R is $\sim 7\%$, a normalization parameter is introduced in a fit to the data. The result of the fit is displayed in Fig. 39, where the 1σ contours are plotted in the $\sin^2\theta_W$ normalization plane (dashed contours). Two values for $\sin^2\theta_W$ are obtained, namely,

$$\sin^2\theta_W = \begin{cases} 0.22\pm 0.03 \text{ (statistical)} \\ 0.56\pm 0.03 \text{ (statistical)} \end{cases} \pm 0.10 \text{ (systematic)} .$$

Also indicated in the figure is the result if one combines the hadron data with the lepton pair results (solid contour), yielding

$$\sin^2\theta_W = 0.22\pm 0.08.$$

The MARK-J collaboration (Barber *et al.*, 1981) makes a quantitative comparison by using a χ^2 method, where χ^2 is defined as

$$\chi^2 = \frac{(F-1)^2}{\sigma_{\text{syst}}{}^2} + \sum_i \frac{(FR^i - R_T{}^i)^2}{\sigma_i{}^2} ,$$

where the sum runs over all measurements at different c.m. energies, and where σ_i and σ_{syst} are the statistical and systematic errors, respectively. The systematic error σ_{syst} is estimated to be 10%. The scaling factor F is used in order to take into account the overall normalization uncertainties. The theoretical cross section R_T is compared with the experimental result R for different values of $\sin^2\theta_W$ in Fig. 40 (Rykaczewski, 1981). The results of the fit are

$$0.12 \le \sin^2\theta_W \le 0.65 \quad (95\% \text{ C.L.})$$

and

$$\sin^2\theta_W = 0.27^{+0.34}_{-0.08}$$

with a minimum χ^2 per degree of freedom $=1.14$.

The limits on $\sin^2\theta_W$ change by $\lesssim 0.02$ for relatively large changes in α_s (0 to 0.24) and σ_{syst} (8% to 12%). The values for the coupling constant α_s and the scaling factor F are correlated; i.e., changes in α_s are compensated for by an appropriate change in F. This demonstrates that the method applied is sensitive to the behavior of R as a function of energy and not to the absolute R values.

A combined analysis of MARK-J data for leptonic [reaction (15)] and hadronic final states [reaction (16)] yields

$$0.13 \le \sin^2\theta_W \le 0.42 \quad (95\% \text{ C.L.})$$

and

$$\sin^2\theta_W = 0.27\pm 0.08 .$$

In conclusion, the determination of $\sin^2\theta_W$ is in good agreement with the value obtained from neutrino scattering experiments. The two types of experiments are done in entirely different kinematic regions. The good agreement in $\sin^2\theta_W$ obtained in two types of experiments gives important support to the validity of the GWS theory and to its applicability in the timelike region up to $q^2=1300$ GeV^2.

2. Determination of g_A and g_V

Since the first experimental observation of the weak neutral-current interaction in $\nu_\mu + e^- \to \nu_\mu + e^-$ (Hasert *et al.*, 1973; Blietschau *et al.*, 1976) several neutrino-electron scattering experiments have obtained important constraints on the structure of the weak neutral currents (Baltay, 1979; Winter, 1979; Büsser, 1980). A unique determination of the leptonic coupling constants g_V and g_A, however, was possible only in a more general framework incorporating lepton-lepton and lepton-quark neutral current interactions (Sehgal, 1978; Hung and Sakurai, 1977, 1979). The analysis involved the use of data from neutrino-nucleon scattering and the scattering of polarized electrons on deuterium (Prescott *et al.*, 1978, 1979), as well as the neutrino-electron scattering results, and depended on factorization relations to relate the lepton-quark to the purely leptonic couplings.

By combining the recent results on e^+e^- elastic scattering, $\mu^+\mu^-$ and $\tau^+\tau^-$ production over the center-of-mass energy range $12 \le \sqrt{s} \le 36$ GeV, with the neutrino-electron scattering data, one is able to determine g_V and g_A uniquely without the complications which arise from the use of hadronic targets. In the general framework of SU(2)×U(1), with a single Z^0 mediating the weak neutral current the sole assumptions required for this determination are (1) e,μ,τ universality, (2) an effective interaction Hamiltonian which is a sum of products of vector and axial-vector currents, and (3) the pointlike nature of leptons.

The data used to test electroweak theories consist of measurements of the angular distribution of Bhabha scattering, μ- and τ-pair production cross section as a function of $\sqrt{s}$, and $\mu^+\mu^-$ forward-backward asymmetry.

In comparing the data on $e^+e^- \to l^+l^-$ ($l=e,\mu,\tau$) with the predictions of electroweak theories, one subtracts the

order α^3 radiative corrections, as well as the contribution from hadronic vacuum polarization (Berends *et al.*, 1973a, b, 1976). The resulting cross sections are defined as σ^{exp} and $d\sigma^{\text{exp}}/d\Omega$. Both weak-electromagnetic interference and pure weak effects are included by using the Hamiltonian (Hung and Sakurai, 1977, 1979; DeGroot and Schildknecht, 1980a, 1980b):

$$H_t = -4\alpha\bar{e}\gamma_\lambda e\bar{l}\gamma^\lambda l - 2\frac{G_F}{\sqrt{2}}\left[\bar{e}\gamma_\lambda(g_V+g_A\gamma_5)e\frac{m_z^2}{m_z^2-s}\bar{l}\gamma^\lambda(g_V+g_A\gamma^5)l\right] \quad \text{for } l=\mu,\tau$$

and

$$H = H_t + 4\pi\alpha\bar{l}\gamma_\lambda e\frac{1}{q^2}\bar{e}\gamma^\lambda l + \frac{2G_F}{\sqrt{2}}\left[\bar{l}\gamma_\lambda(g_V+g_A\gamma_5)e\frac{m_z^2}{m_z^2-q^2}\bar{e}\gamma^\lambda(g_V+g_A\gamma_5)l\right] \quad \text{for } l=e\ .$$

In the above formula, g_V and g_A are the coupling constants of the weak neutral current to leptons and $G_F = 1.02\times10^{-5}/m_p^2$.

The cross section for $e^+e^-\to e^+e^-$ has been calculated (Budny, 1975) to second order in the weak interaction coupling strengths. The modification of the Bhabha scattering angular distribution by weak effects is not immediately apparent in the distributions of $d\sigma(e^+e^-\to e^+e^-)/d\Omega$ commonly used in tests of pure QED. This is shown in Fig. 41(a), where the combined cross section from 29.9 to 36.7 GeV is compared with the predictions of QED. The sensitivity to weak effects is, however, demonstrated in Fig. 41(b), which shows the deviation of the combined data from the QED predictions as a function of $\cos\theta$. The errors shown in Fig. 41(b) include both statistical errors and an estimated point-to-point 3% systematic uncertainty. Also shown in Fig. 41(b) are the predictions of the electroweak theory in terms of the values of vector and axial-vector coupling constants g_A and g_V. The best-fitted curve obtained from Bhabha scattering, as well as $\mu^+\mu^-,\tau^+\tau^-$ production and $\mu^+\mu^-$ asymmetry, is also included. It has to be noted that it is the Bhabha data that are mainly sensitive to the vector coupling. The constraint on the axial coupling is mainly obtained from the asymmetry measurement.

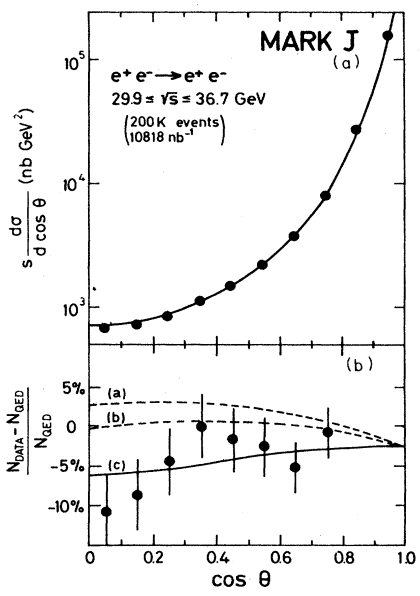

FIG. 41. (a) The differential cross sections $s\,d\sigma/d\cos\theta$ for $e^+e^-\to e^+e^-$. (b) The deviation of the QED predictions from the combined data is plotted as a function of $\cos\theta$. The error includes both statistical and 3% point-to-point systematic uncertainties. The curves a, b, and c represent the prediction of the electroweak theory with $(g_A^2=\frac{1}{4},\ g_V^2=0.16)$, $(g_A^2=\frac{1}{4},\ g_V^2=\frac{1}{4})$, and the best-fitted result $(g_A^2=0.21,\ g_V^2=-0.05)$, respectively. The best-fitted results require that the normalization of the curves a, b, and c be scaled down by 2.5% as shown (the normalization uncertainty is 3%).

The results for the vector and axial-vector couplings squared h_{VV} and h_{AA} are shown in Fig. 42 (Pohl, 1981; Duinker, 1981). In the $h_{VV}-h_{AA}$ plane the GWS model is represented by a line parallel to the h_{VV} axis and intersecting the h_{AA} axis at 0.25. The MARK-J group converted these results (Barber *et al.*, 1980c; 1981), including correlations into an allowed region in the g_V-g_A plane, as shown in Fig. 43. Also shown in the figure are neutrino-electron scattering data $\nu_\mu e^-\to\nu_\mu e^-$, $\bar{\nu}_\mu e^-\to\bar{\nu}_\mu e^-$, $\nu_e e^-\to\nu_e e^-$, which limit the possible value of g_A and g_V in two regions in the g_V-g_A plane around $(g_V=0,\ g_A=-\frac{1}{2})$ and $(g_V=-\frac{1}{2},\ g_A=0)$ (Faiss-

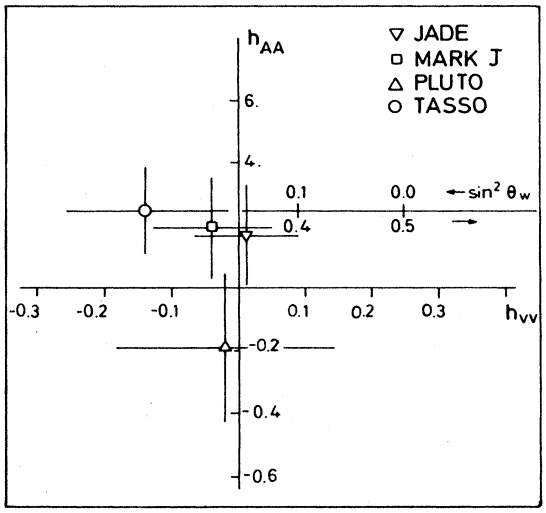

FIG. 42. Best-fit values for h_{VV} and h_{AA} and their uncorrelated 1σ errors from the PETRA experiments.

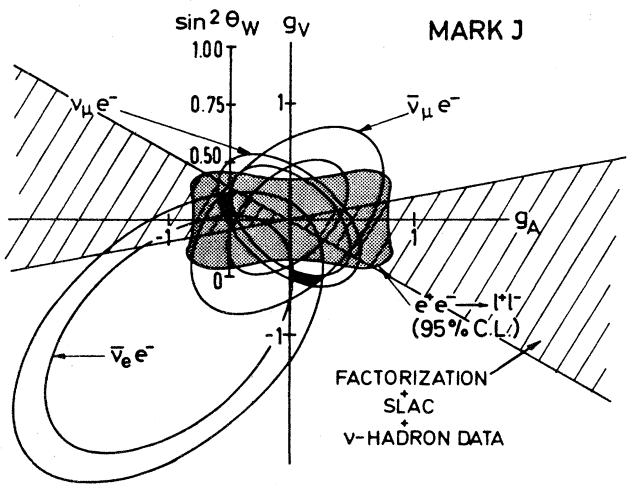

FIG. 43. Results obtained from neutrino experiments and the MARK-J experiment expressed in terms of limits on g_V and g_A. The region in between the concentric ellipses corresponds to 68% C.L. limits from the neutrino electron scattering experiments. The two black areas indicate the two allowed regions for g_V and g_A from the combined neutrino data. The shaded area represents the 95%-C.L. contour from the MARK-J experiment. The hatched area is the allowed region obtained from deep-inelastic neutrino nuclear scattering and polarized electron deuterium scattering data.

ner, 1979; Reithler, 1979; Heisterberg *et al.*, 1980). Combining the MARK-J and the neutrino scattering data, we can rule out the second solution with more than 95% confidence. Similar results have been obtained by other PETRA groups (Bartel *et al.*, 1981b; Branson, 1981).

This confirms the conclusion drawn on the basis of deep-inelastic neutrino nuclear scattering and polarized electron deuterium scattering data. The allowed region from these experiments plus the additional requirement of factorization relations is shown in the figure as the hatched area (Hung and Sakurai, 1979). It has to be noted, however, that the MARK-J result is obtained without having recourse to models of hadron production by the weak neutral current.

E. Tests of models of the electroweak interaction with more than one neutral boson

Georgi and Weinberg (1978) and Bjorken (1979) have suggested that the standard model can be naturally extended to models based on an enlarged symmetry group $SU(2)\times U(1)\times G$, where G stands for a general symmetry group, without changing any of the predictions which have been made for the low-q^2 range covered by lepton-nucleon scattering data. The generalized models differ from the $SU(2)\times U(1)$ model in the high-q^2 region, because they have more than one neutral weak boson. The lowest-mass neutral boson in these models has a mass smaller than the Z^0 mass in the standard model.

To first order in s/m_z^2 the deviation of the multiple Z^0 models from the standard model can be described by an additional term $Cj_{\rm em}^2$ to the effective Hamiltonian of the standard model. The effective Hamiltonian contains three parameters h_{VV}, h_{VA}, and h_{AA}, where the parameter C modifies only h_{VV} (Hung and Sakurai, 1977, 1979),

$$h_{VV}=\tfrac{1}{4}(1-4\sin^2\theta_W)^2+4C,\quad C\geq 0$$

$$h_{VA}=\tfrac{1}{4}(1-4\sin^2\theta_W)=g_V\cdot g_A\ ,$$

while the term containing the axial-vector current remains the same as in the standard model,

$$h_{AA}=g_A{}^2=\tfrac{1}{4}\ ,$$

where g_V and g_A are the vector and axial-vector coupling constants in the standard model, respectively. In the case where C vanishes, h_{VV} reduces to $g_V{}^2$ as expected in the standard model. This term appears not only in the gauge models of the type of $SU(2)\times U(1)\times G$ but also in general electroweak mixing schemes (Bjorken, 1979). The parameter C can therefore be used as a universal quantity independent of the details of the models. Since this term is proportional to the electromagnetic currents which couple to charge and is parity conserving, it contributes neither to the neutrino scattering processes nor to polarized e-D scattering. On the other hand, the reactions $e^+e^-\to l^+l^-$ ($l=e,\mu,\tau$) at present PETRA energies $\sqrt{s}=35$ GeV begin to be sensitive to the effects of an additional Z^0 with a mass below that of the standard model Z^0 and provide an opportunity to set stringent limits on C. The corrections due to the Z^0 propagator are incorporated in the calculation of the cross sections.

From the limit of C, limits on the masses of Z^0's in specific models can be obtained. As an illustration, we consider the case of two Z^0's with masses m_1 and m_2. In models based on $SU(2)\times U(1)\times U(1)$, with one doublet of charged and two neutral gauge bosons, we have the relation (De Groot *et al.*, 1979, 1980a,b; De Groot and Schildknecht, 1980b)

$$C=\cos^4\theta_W\left[\frac{m_z^2}{m_1^2}-1\right]\left[1-\frac{m_z^2}{m_2^2}\right],$$

while the models based on $SU(2)\times U(1)\times SU(2)$, with two doublets of charged and neutral gauge bosons, we have (Barger *et al.*, 1980a,b,c)

$$C=\sin^4\theta_W\left[\frac{m_z^2}{m_1^2}-1\right]\left[1-\frac{m_z^2}{m_2^2}\right].$$

With $\sin^2\theta_W=0.23$, for the same mass m_1 and m_2, C in the $SU(2)\times U(1)\times U(1)$ model is about eleven times greater than the C in $SU(2)\times U(1)\times SU(2)$ model. These two models thus represent approximately the extreme cases of the strength of coupling constants of this type of models. In comparing the data on $e^+e^-\to l^+l^-$ ($l=e,\mu,\tau$) with the predictions of electroweak theories the radiative corrections are subtracted. The weak-electromagnetic interference and pure weak effects are included.

The cross sections for $e^+e^-\to l^+l^-$ ($l=e,\mu,\tau$) have

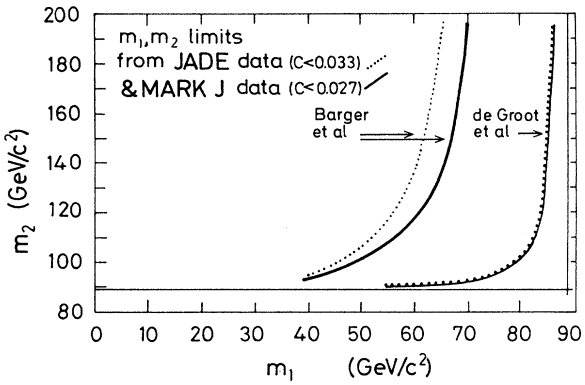

FIG. 44. The 95% C.L. contours for fits to the two gauge boson models by the MARK-J and JADE collaborations.

been calculated in terms of $\sin^2\theta_W$ and the parameter C. Using the measured values of $\sin^2\theta_W=0.23$, the MARK-J group makes a one-parameter fit to all of the ee, $\mu\mu$, and $\tau\tau$ data, while the normalization is allowed to vary within $\pm 3\%$ due to the uncertainty in the luminosity (Böhm, 1980). They find $-0.04 \leq C \leq 0.027$ at the 95% confidence level. A similar result was obtained by the JADE Collaboration, whose value of C was found to be ≤ 0.033 at 95% confidence level (Marshall, 1980).

The upper limit on C can be converted in a limit in the m_1-m_2 plane for the two models, as shown in Fig. 44. In all these models there is a constraint that $m_1 \leq m_z \leq m_2$. Therefore, the two lines $m_1=m_z$ and $m_2=m_z$ are the natural boundaries of the allowed region. The data put severe limits on the SU(2)×U(1)×U(1) model, constraining the masses of the two Z's in a small region. The limits on the SU(2)×U(1)×SU(2) are less stringent but significant.

V. TWO-PHOTON RESULTS FROM PETRA

A. Introduction

A high-energy e^+e^- storage ring like PETRA offers the possibility to study the two-photon exchange reactions in a detailed and systematic way. The reaction under study is

$$e^+e^- \rightarrow e^+e^-X \,, \tag{17}$$

where X can be a lepton-antilepton pair or hadrons.

Several of the PETRA detectors have built measuring devices in the forward direction to determine the angle and energy of the scattered electron or positron emerging at small angles from reaction (17). One of these tagging systems, the one belonging to the PLUTO detector, has been described in some detail in Sec. III.B.

When system X of reaction (17) is a lepton-antilepton pair, tests of QED can be performed. When system X consists of hadrons, several interesting studies on resonance production in the two-photon exchange reaction have been carried out. Total cross-section measurements have been performed, and results on comparisons between a $q\bar{q}$ production model with the vector dominance model (VDM) for events with high-transverse momentum jets have been made.

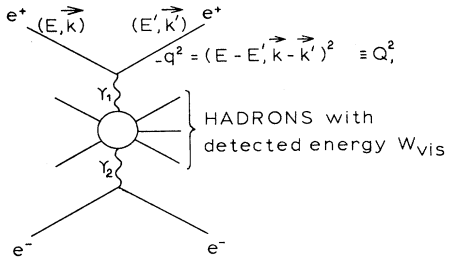

FIG. 45. Schematic view of a two-photon annihilation event $e^+e^- \rightarrow e^+e^-$ + hadrons.

A structure function for the photon has been extracted by the PLUTO collaboration from the deep-inelastic electron-photon scattering events.

Review talks by Ch. Berger (1980) and Wagner (1980) of the PLUTO collaboration and by Hilger (1980) of the TASSO collaboration cover the topics of the two-photon physics in detail.

Figure 45 shows a schematic view of a two-photon exchange reaction producing hadrons in the final state. When we define $(E,\mathbf{k})$ as the four momentum of the incoming electron and $(E',\mathbf{k}')$ as the four momentum of the outgoing electron, the momentum transfer squared to the virtual photon γ is given by

$$-q^2=\{(E-E',\mathbf{k}-\mathbf{k}')\}^2 \equiv Q_1{}^2 \,.$$

When both the outgoing electron and positron are detected in the tagging systems, one speaks of a double tagged event. These events are rare, owing to the very limited solid angle, and no results have been obtained so far for this type of configuration. In case only the electron or positron is detected (a single tagged event), one of the virtual photons will have a very small Q^2. Events of this type can be pictured as the scattering of an electron on a quasireal photon. For the no-tag events only lepton-antilepton pairs or hadrons are measured in the central detectors and none of the scattered electrons and positrons.

A common feature of all the two-photon events is the limited energy for the lepton-antilepton pairs or the hadronic system. The total visible energy in the central detectors is small because of the small amount of energy transferred to the virtual photons from the incoming electron and positron beams. The separation of the two-photon exchange events and the one-photon annihilation events is therefore straightforward and can be readily made by cuts on the visible energy and the sum of the transverse momenta of the particles in the central detector (Berger *et al.*, 1979e).

B. Tests of QED in two-photon processes

The relevant diagrams for tests of QED in the two-photon exchange channels are shown in Fig. 46(a). The following reactions are studied

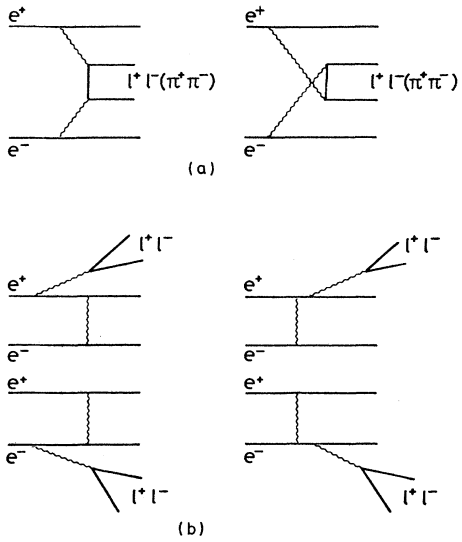

FIG. 46. Feynman diagrams for pair production via (a) the two-photon exchange process and (b) the bremsstrahlung process ($l^{\pm}=e^{\pm},\mu^{\pm}$).

$$e^+e^-\rightarrow e^+e^-+e^+e^- , \tag{18}$$

$$e^+e^-\rightarrow e^+e^-+\mu^+\mu^- . \tag{19}$$

Higher-order corrections in the single-photon annihilation channel due to the conversion of a radiated photon in a lepton-antilepton pair [shown in Fig. 46(b)] give rise to the same final states as processes (18) and (19).

The results obtained by the JADE collaboration for $e^+e^-\rightarrow e^+e^-+\mu^+\mu^-$ are shown in Fig. 47. The comparison with QED was performed by using a Monte Carlo program written by Vermaseren. The prediction of QED includes an exact calculation of the diagrams of Fig. 46(a) plus their interference with the bremsstrahlung terms of Fig. 46(b). The agreement between data and predictions is good.

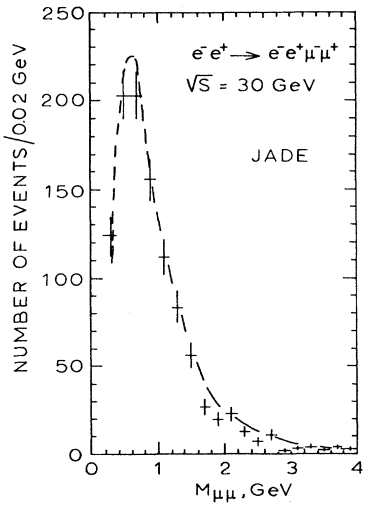

FIG. 47. The distribution of the $\mu^+\mu^-$ effective mass from the events $e^+e^-\rightarrow e^+e^-\mu^+\mu^-$ as measured by the JADE detector. The solid line is the QED prediction.

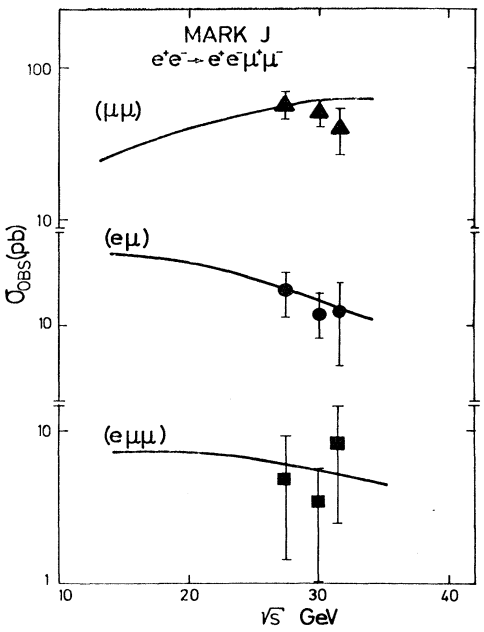

FIG. 48. The observed cross section of $e^+e^-\rightarrow e^+e^-\mu^+\mu^-$ in the MARK-J detector as functions of $\sqrt{s}$ when the observed particles are (a) two μ's, (b) one μ and one e, (c) two μ's and one e. The solid lines are Monte Carlo calculations of the yield from two-photon diagrams, and the points are the measurement.

The calculated cross sections in the MARK-J detector for reaction (19), when the observed particles are (a) two μ's only, (b) only one μ and one e, and (c) two μ's and one e, are shown in Fig. 48.

The cross sections for each of these configurations were computed by using the same Monte Carlo program as above. The measured cross sections, also shown in Fig. 48, agree well with the calculations in all cases.

C. The exclusive reactions $\gamma\gamma\rightarrow f^0$ and $\gamma\gamma\rightarrow\rho^0\rho^0$

1. The reaction $\gamma\gamma\rightarrow f^0$

The Pluto and TASSO collaborations have measured the final state

$$e^+e^-\rightarrow e^+e^-+\text{two charged particles}$$

without tagging the forward electron and positron. By studying only those events with low visible energy in the central detector and demanding that the two tracks reconstruct the crossing point of the colliding beams, the processes $e^+e^-\rightarrow e^+e^-e^+e^-$, $e^+e^-\rightarrow e^+e^-\mu^+\mu^-$, and $e^+e^-\rightarrow e^+e^-\pi^+\pi^-$ are selected with little background from beam gas interactions. The background is reduced event further by selecting the events for which the two charged tracks are coplanar but acollinear. The dominant part of the final-event sample contains lepton-antilepton pairs from reactions (18) and (19). The

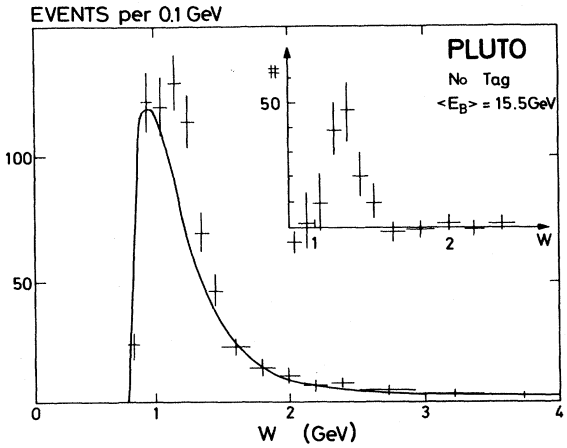

FIG. 49. The effective-mass spectrum of the two opposite charged particles from the reaction $e^+e^-\to e^+e^-+2$ charged particles at $\sqrt{s}=31$ GeV for events where the outgoing e^+ and e^- go undetected. The solid curve is the expectation for the QED processes $e^+e^-\to e^+e^-+e^+e^-$ and $e^+e^-\to e^+e^-+\mu^+\mu^-$. The insert shows the difference between the measured histograms and the solid curve.

$\gamma\gamma\to\pi^+\pi^-$ final state was calculated to contribute $\sim 16\%$ to the events.

The invariant mass distribution of the two-prong events for average beam energies of 15.5 GeV obtained in the PLUTO detector (Berger *et al.*, 1980a) is shown in Fig. 49. The agreement with the QED calculation below 1 GeV and above 1.5 GeV is good; however, a clear excess of events is seen in the region between 1 and 1.5 GeV. The insert in Fig. 49 shows the difference between the data and the QED prediction: a resonance behavior is seen at the mass of the f^0 resonance. In order to extract the decay width of $f^0\to\gamma\gamma$ a helicity amplitude of $\lambda=2$ is assumed and a value for the width $\Gamma(f^0\to\gamma\gamma)=2.3\pm0.5$ KeV with an additional systematic error of $\pm 15\%$ is obtained.

The distribution of the difference between the measured invariant mass of the two charged particles and the QED background of the TASSO collaboration (Hilger, 1980) is shown in Fig. 50. A very clear f^0 signal is observed. The curve shown in the figure is the result for the f^0 contribution using the model of Krasemann and Vermaseren. A preliminary value for $\Gamma(f^0\to\gamma\gamma)=4.1\pm0.4$ KeV with a systematic uncertainty of 15% has been derived.

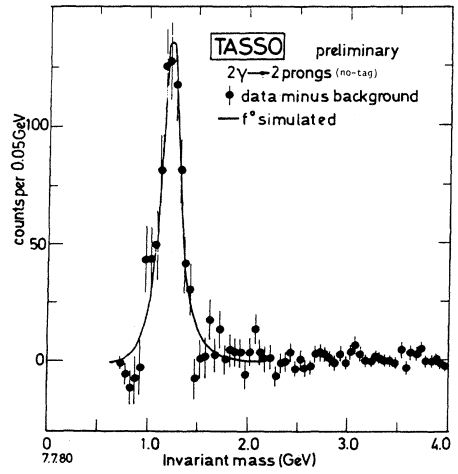

FIG. 50. The f^0 signal of the TASSO collaboration, together with the fit of the model (Hilger, 1980).

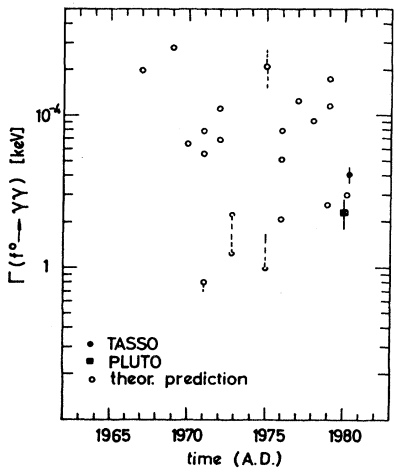

FIG. 51. Data and predictions for the radiative width $\Gamma(f^0\to\gamma\gamma)$.

The results for the width $\Gamma(f^0\to\gamma\gamma)$ of the two groups is compared with the theoretical predictions in Fig. 51. The calculations with the nonrelativistic quark model are in reasonable agreement with the data; the predictions of the other models, however, clearly disagree (Fil'kov 1967; Radutskii, 1967, 1969; Renner, 1971; Bramón and Greco, 1971; Kleinert *et al.*, 1972; Schierholz and Sundermeyer, 1972; Berger and Feld 1973; Novikov and Éĭdel'man, 1975; Faiman *et al.*, 1975; Levey *et al.*, 1976; Grassberger and Kögerler, 1976; Babcock and Rosner, 1976; Greco, 1977; Greco and Srivastava, 1978; Budnev and Kaloshin, 1979; Cottingham and Dunbar, 1979).

2. The reaction $\gamma\gamma\to\rho^0\rho^0$

The first observation of the reaction

$$\gamma\gamma\to\rho^0\rho^0 \tag{20}$$

has been reported by the TASSO collaboration (Brandelik *et al.*, 1980g). Events with two negative and two positive tracks in the central detector originating from the interaction point are the candidates for reaction (20). Additional requirements are that the energy of the two-photon system be in the region $1.5\le W_{\gamma\gamma}\le 2.3$ GeV and that the P_T, defined as the vector sum of the transverse momenta of the four charged particles be smaller than 0.15 GeV/c. Application of the above criteria leave an event sample of 89 events for further study. Assuming these events to be

$$e^+e^-\to e^+e^-\pi^+\pi^-\pi^+\pi^- ,$$

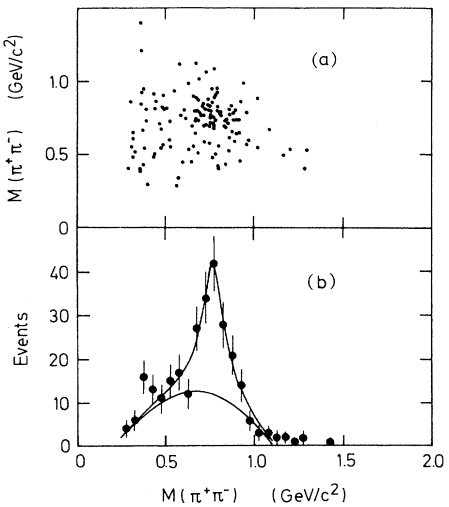

FIG. 52. Mass distributions of $\pi^+\pi^-$ pairs for events with $1.5 \leq W_{\gamma\gamma} \leq 2.0$ GeV. (a) Two-dimensional mass distribution of a $\pi^+\pi^-$ combination vs the opposite one, and (b) distribution of the $\pi^+\pi^-$. The curves are the result of a fit (Brandelik *et al.*, 1980g).

one can calculate the invariant-mass distribution of the $\pi^+\pi^-$ combination. Figure 52(a) shows the two-dimensional mass distribution of one such combination versus the opposite one for $1.5 \leq W_{\gamma\gamma} \leq 2.0$ GeV. The pronounced enhancement when both mass values are near the ρ mass is evidence for the $\rho^0\rho^0$ final state. Figure 52(b) gives the projection onto the $\pi^+\pi^-$ mass axis.

The curves in Fig. 52(b) are the results of a fit including photon flux calculations and contributions from noninterfering $\rho^0\rho^0$ production, ρ^0 + nonresonant $\pi^+\pi^-$ production, and contributions from phase space. The result of this fit indicates that the four-charged pion states results mainly from the production of $\rho^0\rho^0$ at low $W_{\gamma\gamma}$.

The cross sections for $\rho^0\rho^0$ production are determined using the results of the above-mentioned fit by calculating the acceptance for the events. The results are shown in Fig. 53 together with the prediction of a VDM model calculation. At large $W_{\gamma\gamma}$ this model could be correct, but the disagreement for $W_{\gamma\gamma} \leq 2$ GeV indicates the presence of a threshold enhancement in the process $\gamma\gamma \to \rho^0\rho^0$.

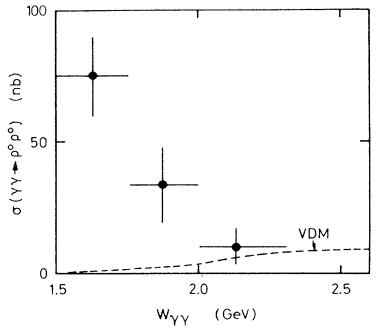

FIG. 53. Cross section for the reaction $\gamma\gamma \to \rho^0\rho^0$. The curve is the prediction of the VDM model.

D. Total cross-section measurement for multihadron production

The total cross section for the two-photon exchange reactions producing hadrons

$$\gamma\gamma \to \text{hadrons} \tag{21}$$

has been measured by the PLUTO (Berger *et al.*, 1981a) and TASSO collaborations (Hilger, 1980) using the single-tagged events. The measurement is a difficult one, because several assumptions and approximations have to be made in order to extract from the data the relevant quantities.

I will describe the procedure followed by the TASSO group in some detail. The luminosity for the photon-photon collisions is calculated by this group using the functions of Field (1980). According to the TASSO group the photon-photon luminosity at low total photon-photon energy $W_{\gamma\gamma}$ is considerably higher than the one obtained when using the Weizsäcker-Williams approach (Carimalo *et al.*, 1979a,b, 1980). To derive values for the $\gamma\gamma$ cross section for real photons the measurements at finite Q_1^2 values are extrapolated to $Q^2=0$. The functional form for this extrapolation is in the spirit of the VDM. Form factors for the virtual photons are included and the cross section is written as

$$\sigma_{\text{tot}}(W_{\gamma\gamma},Q_1^2,Q_2^2) = A + \frac{B}{W_{\gamma\gamma}} \left[\frac{1}{1+(Q_1^2/m_\rho^2)}\right] \left[\frac{1}{1+(Q_2^2/m_\rho^2)}\right], \tag{22}$$

where A and B are parameters to be determined and the last two expressions in brackets are the form factors. The other assumptions put into a model to describe the hadron events are the following:

(a) The hadronic system is generated according to a phase-space model with limited transverse momentum with respect to the photon-photon axis,

$$\langle P_T^{\gamma\gamma} \rangle = C \ .$$

(b) The ratio between charged to neutral particles is 2:1.

(c) The mean charged multiplicity is a function of $\ln W_{\gamma\gamma}$,

$$\langle n_{\text{ch}} \rangle = D + E \ln W_{\gamma\gamma} \ .$$

The Monte Carlo events thus generated are compared to the data. The measured distributions of Q_1^2, the charged multiplicity, and the visible energy in the central detector are used to fit the five parameters A to E. The results of the fit are

$$\langle P_T^{\gamma\gamma} \rangle = 0.298 \text{ GeV}/c \ ,$$

$$\langle n_{\text{ch}} \rangle = 2.1 + 1.5 \ln W_{\gamma\gamma} \ ,$$

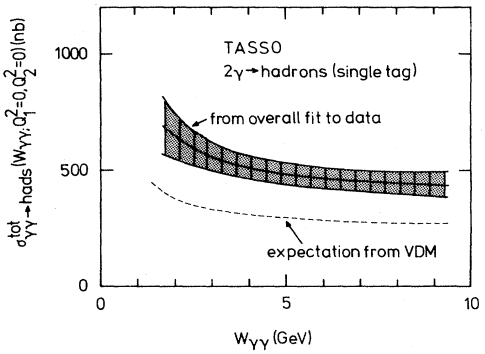

FIG. 54. The hadronic cross secction for scattering of two real photons vs the c.m. energy of the two-photon system as obtained from the fit to the data under the assumption stated in the text. The hatched area indicates the range of the statistical error.

and

$$\sigma_{\gamma\gamma\to\text{hadrons}}=(380+520/W_{\gamma\gamma})\text{nb} .$$

Figure 54 shows the result of the total cross-section measurements of the TASSO group.

The above expression for $\sigma_{\gamma\gamma\to\text{hadrons}}$ corresponds to the central line in the figure. An overall systematic error of $\sim 25\%$ has to be taken into account.

The cross-section behavior as a function of the total photon-photon energy for $W_{\gamma\gamma}\geq 3$ GeV is, as far as the shape of the distribution is concerned, in agreement with the VDM prediction; the absolute scale, however, disagrees with the measurements. This effect can be resolved only if the systematic errors become less than the 25% at present.

The PLUTO results (Berger *et al.*, 1981a) are shown in Fig. 55. Figures 55(a) and 55(b) show the cross-section behavior as a function of Q^2 for two visible invariant-mass bins W_{vis}. The solid lines in these graphs are the predictions from a ρ meson dominance model calculation.

To extract the total cross section an additional term is introduced in expression (22), and the ansatz for the fit to the data is

$$\sigma_{\text{tot}}(W_{\gamma\gamma})=A\sigma^{\text{VDM}}(W_{\gamma\gamma})+B/W_{\gamma\gamma}{}^2 ,$$

where

$$\sigma^{\text{VDM}}(W_{\gamma\gamma})=(240+270/W_{\gamma\gamma})\text{nb} .$$

The best fit to the invariant-mass distribution is achieved for $A=0.97\pm 0.16$ and $B=2250\pm 500$ nb GeV^2. The result is shown in Fig. 55(c). The dramatic rise at low $W_{\gamma\gamma}$ can be described by the fit only if a $B/W_{\gamma\gamma}{}^2$ is introduced. This term is expected if there are contributions of quark-antiquark production in the two-photon exchange channel.

The discrepancy between the results at low $W_{\gamma\gamma}$ between the PLUTO and TASSO groups is unresolved at the moment. The PLUTO group notes (Berger *et al.*, 1981a) that one should take into account the following:

(1) The triggering efficiency of a hadronic event is

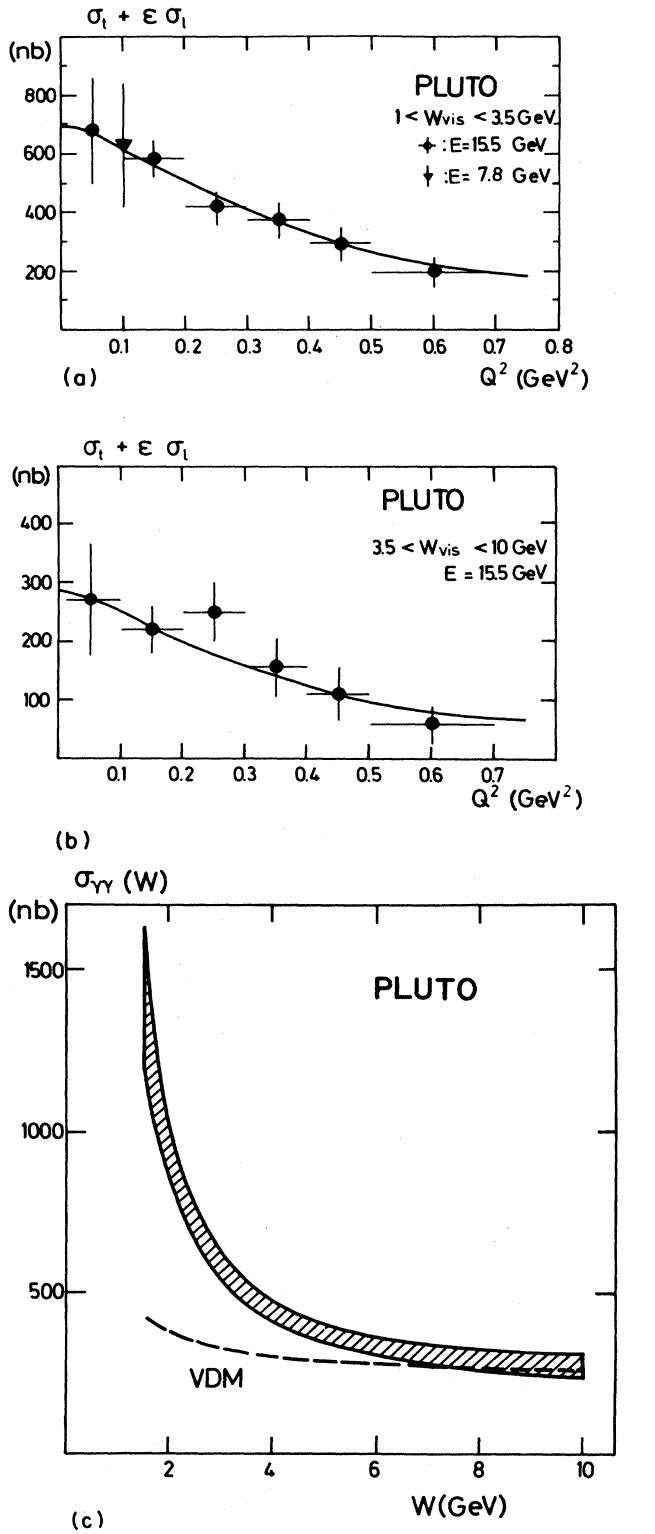

FIG. 55. The total cross section $\sigma_t + \epsilon\sigma$, as a function of Q^2 for (a) $W_{\text{vis}}\leq 3.5$ GeV and for (b) $W_{\text{vis}}\geq 3.5$ GeV. The solid line is the prediction from ρ-meson dominance. (c) The total photon-photon cross section extrapolated to $Q^2=0$ vs the true invariant mass W. The hatched band represents the 1σ limits as obtained from the fit. The VDM prediction is given by the dashed line.

about 25%, quite in contrast to the events from single-photon annihilation, where the efficiency is 80 to 90%.

(2) Due to the limited solid angle in the central regions the visible invariant mass is always smaller than $W_{\gamma\gamma}$ due to losses of particles. The correction $W_{\rm vis}\rightarrow W_{\gamma\gamma}$ is done in both cases by unfolding procedures.

(3) There are two major differences in the analysis of the two experiments: (a) PLUTO uses single-tagged events only, but TASSO includes the double-tagged events, and (b) TASSO uses the charged particles only, but PLUTO includes the neutrals, leading to a smaller correction $W_{\rm vis}\rightarrow W_{\gamma\gamma}$.

Results on hard-scattering processes and deep-inelastic $e\gamma$ scattering have been reported and can be found in Berger (1980) and Wagner (1980).

VI. GENERAL CHARACTERISTICS OF HADRON EVENTS

A. Total hadronic cross sections

The final selection of the hadronic events from the single-photon annihilation process

$$e^+e^-\rightarrow\text{hadrons}$$

is made by scanning the events on an interactive graphics display system after a preselection which includes cuts in the charged multiplicity, visible energy, and momentum balance. Beam-gas events not coming from the interaction region are recognized by reconstructing the event vertex (Bartel *et al.*, 1979a; Orito, 1979; Barber *et al.*, 1979b, 1980b; Berger *et al.*, 1979a, c; Brandelik *et al.*, 1979a, 1980i).

The total cross section for $e^+e^-\rightarrow$hadrons was measured over a wide range of center-of-mass energies from 12 to 36.7 GeV, including results obtained by extended periods of running at a fixed beam energy and by fine energy scans (Barber *et al.*, 1980b; Bartel *et al.*, 1980b, 1981c; Berger *et al.*, 1980b; Brandelik *et al.*, 1979c) covering the ranges of 29.92 to 31.46 GeV and 33.00 to 36.70 GeV^2. The results are expressed in terms of R:

$$R=\sigma(e^+e^-\rightarrow\text{hadrons})/\sigma(e^+e^-\rightarrow\mu^+\mu^-)\ .$$

In the naive quark-parton model, the cross section for the hadron production process is simply given by the sum over flavors of the pointlike $q\bar{q}$ pair cross sections. Using this picture with spin-$\frac{1}{2}$ massless quarks and with three colors gives

$$R_0=3\Sigma e_q{}^2\ ,$$

where e_q is the charge of the quark with flavor q. Considering the five known quarks (u, d, s, c, and b), and correcting the naive model for gluon emission as predicted by QCD, one expects $R\approx 4$, over the entire PETRA energy range, with only a slight decrease in R with increasing beam energy.

The experimental R values have to be corrected for initial-state radiative corrections, for contamination of the sample by hadronic events produced by the two-photon process $e^+e^-\rightarrow e^+e^-+$hadrons, and for the contribution of $e^+e^-\rightarrow\tau^+\tau^-\rightarrow$hadrons ($+$ leptons). In addition to the statistical errors, there is additional systematic uncertainty due to the model dependence of the acceptance calculations of $\sim 10\%$. The measurements of R from four PETRA Groups are averaged and plotted in Fig. 56 (Timm, 1980; Cords, 1980; Ryckaczewski, 1981). Some recent results from CELLO and MARK-J at PETRA and MARK II at PEP are also included (Duinker, 1981). Above $\sqrt{s}=12$ GeV there is a large range up to

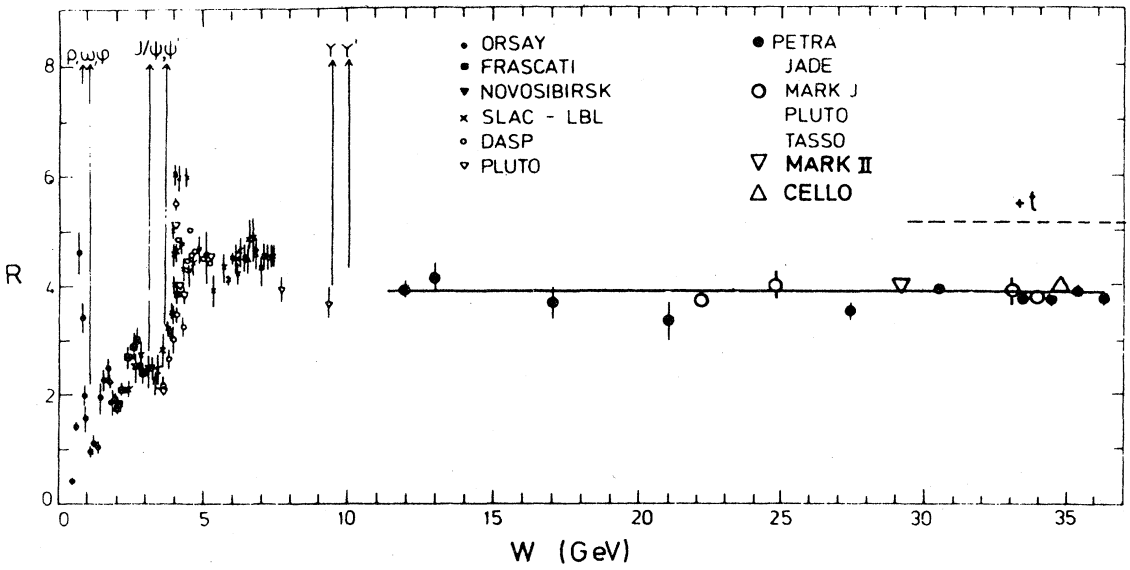

FIG. 56. The total relative hadronic cross section R as a function of W, the c.m. energy. The drawn line is a straight line fit to the PETRA data. Also indicated are the recent measurements from the CELLO and MARK-J groups at PETRA and the MARK II group at PEP.

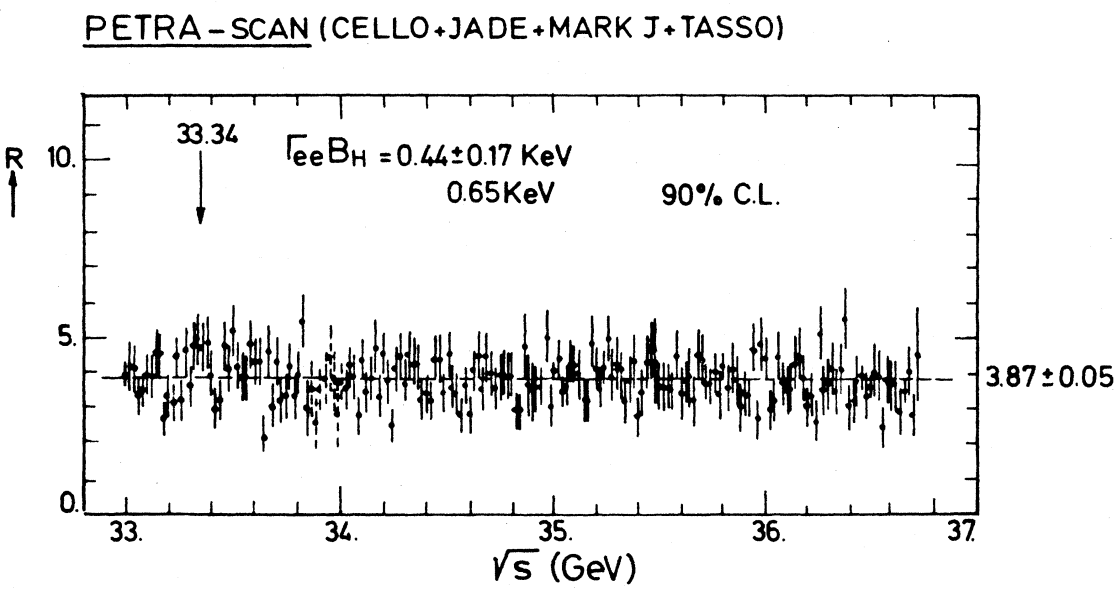

FIG. 57. Average R values measured by the PETRA experiments during the energy scan between 33.00 and 36.70 GeV.

36 GeV where the R values vary only a little. The error weighted average of the combined PETRA data above $\sqrt{s}=12$ GeV yields a value $R=3.84\pm0.04$ (solid line in Fig. 56). This value rules out the production of $t\bar{t}$ quarks, as the expected value for R would be ~ 5.

In addition to the $t\bar{t}$ contribution to the hadronic continuum, the toponium system should form one or more bound states, with the number of such states depending on the shape of the binding potential (Rosner *et al.*, 1978; Quigg, 1979; Greco, 1978). Interpretation of the vector mesons ρ, ω, ϕ, J, ψ', Υ, Υ', and Υ'', as nonrelativistic $q\bar{q}$ bound states or "quarkonia" leads to the prediction that the gap between the lowest bound state and the continuum is probably ~ 1 GeV and very likely ≤ 2 GeV.

In order to check for the existence of $t\bar{t}$ bound states lying below 36.7 GeV, the energy scans mentioned earlier were performed in 20-MeV center-of-mass energy steps (matching the rms energy spread of PETRA), with an average of ~ 25 nb^{-1} to 50 nb^{-1} per point and per experiment. The combined result of the highest energy scan is shown in Fig. 57. The figure shows that the data are entirely consistent with the predictions of QCD for u, d, s, c, and b quarks, that is, with constant values of R over the regions of the scans. There is no indication of an upward slope with increasing energy signaling the onset of a new contribution to the continuum. The value of R averaged over the energy range of the scan is 3.87 ± 0.05.

In order to set a quantitative upper bound on the possible production of a narrow resonance, the data in Fig. 57 were fitted by a constant plus a Gaussian. Using the relation between the resonance strength, the width into $e^+e^-(\Gamma_{ee})$, the hadronic width (Γ_h), the total width (Γ), and the hadronic branching ratio ($B_h \equiv \Gamma_h/\Gamma$), one obtains 0.65 KeV as an upper limit for $B_h\Gamma_{ee}$ (90% C.L.).

From the experimental observation that the reduced width Γ_{ee}/e_q^2 is approximately constant for the vector meson ground states ρ, ω, ϕ, J, and Υ [predicted also by duality arguments (Applequist and Georgi, 1973; Zee, 1973; Dine and Sapirstein, 1979)], and assuming the branching ratio for the lowest-mass meson in the toponium family to hadrons to be $B_h \geq 0.7$, upper limits for $q\bar{q}$ bound states for quark charges $\frac{2}{3}e$ and $\frac{1}{3}e$ can be derived. This is illustrated in Fig. 58, where the reduced width Γ_{ee}/e_q^2 is plotted as a function of the mass of the known vector mesons. The upper limit derived for $q\bar{q}$ bound states where the quark charge is $\frac{2}{3}e$ is clearly excluded. The upper limit for the production of a state with a quark charge $q=\frac{1}{3}e$ is also indicated.

B. Jet analysis

1. Thrust and sphericity distributions

Data at lower energies from SPEAR (Schwitters, 1975; Hanson *et al.* 1975), have shown that the final-state hadrons from the process $e^+e^- \rightarrow$ hadrons are predom-

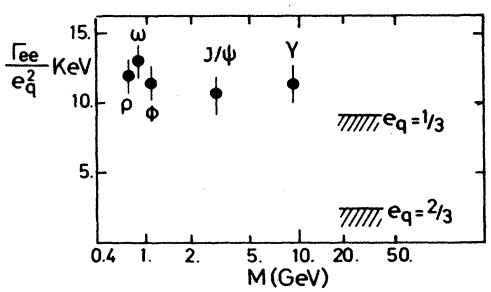

FIG. 58. The reduced width Γ_{ee}/e_q^2 as a function of mass. The 90% C.L. upper limits for the production of a $t\bar{t}$—bound state with either $\frac{2}{3}e$ or $\frac{1}{3}e$ charge are indicated.

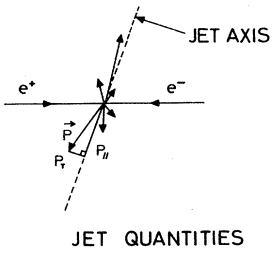

FIG. 59. Schematic drawing of a two-jet event.

inantly collimated into two back-to-back "jets" in agreement with the expectations of simple models in which the timelike photon materializes initially into a quark-antiquark pair. It is thus necessary to develop kinematic quantities which describe the jetlike nature of the hadronic events.

A jet analysis has been devised using the spatial distribution of the measured-momenta of charged and neutral particles for the track detectors and the distribution of the deposited energy in the case of a calorimetric detector. A schematic view of a two-jet event is drawn in Fig. 59. The vectors drawn stand for either the measured momenta p_i of individual particles or the vector energy flow E_i for one or more particles emitted closely together. The aim of the jet analysis is to determine the jet axis and the related quantities like momentum p_T or transverse energy flow E_T and the longitudinal momentum $p_{//}$ or longitudinal energy flow $E_{//}$. Other parameters describing the general shape of the individual events are the sphericity (S) and thrust (T). The sphericity is defined as $S=\frac{3}{2}\min\Sigma p_T^{i2}/\Sigma p^{i2}$ (Bjorken and Brodsky, 1970a), where p_T^i is the transverse component of p^i along a given axis and the minimum is found by varying the direction of this axis. The resultant direction is thus the direction along which the $p_T{}^2$ is minimized. The parameter thrust (T) is defined (Farhi, 1977; Brandt *et al.*, 1964; Brandt and Dahmen, 1979) as

$$T=\max(\Sigma\,|p^i_{//}|\,/\Sigma\,|p^i|\,)$$

for the track detectors and as

$$T=\max(\Sigma E^i_{//}/\Sigma\,|E^i|\,)$$

for the MARK-J detector (Barber *et al.*, 1979b, c). The resultant direction found in this case is the direction along which the sum of the longitudinal momenta or projected energy flow is maximized. Both quantities S and T simultaneously define the jet axis, and it has been found that by applying these two methods to the same event sample the axis coincides within a few degrees for both methods.

The $\cos\theta$ distribution of the MARK-J data shown in Fig. 60, where θ is the angle between the beam and the jet axis, is compared with the expectation from QCD. The agreement with the essentially $1+\cos^2\theta$ distribution multiplied by the angular acceptance of the detector is very good, supporting the idea that the underlying e^+e^- annihilation process proceeds via the production of two spin-$\frac{1}{2}$ particles, the quark and the antiquark. Spin-zero

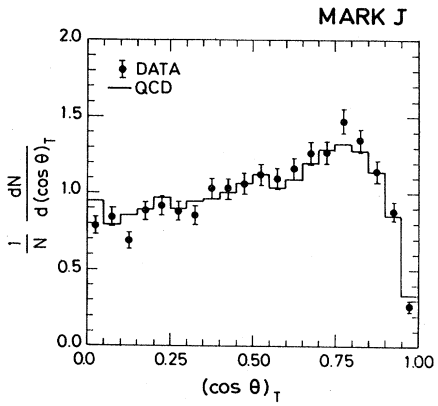

FIG. 60. Angular distribution of the jet axis. The angle θ is defined as the angle between the beam axis and the jet axis. The drawn histogram is the expectation from QCD multiplied by the angular dependent acceptance of the MARK-J detector.

particles would give a $\sin^2\theta$ distribution, which is clearly excluded by the data.

The mean longitudinal $\langle p_{//}\rangle$ and transverse momentum $\langle p_T\rangle$ of charge particles with respect to the thrust axis [measured by the PLUTO and TASSO detectors (Berger *et al.*, 1979a, b, c; Brandelik *et al.*, 1979a, c)] is shown in Fig. 61 as a function of the c.m. energy. Both the increase of $\langle p_{//}\rangle$ and the constancy of $\langle p_T\rangle$ indicate that the jet structure is getting more and more pronounced, most of the particles are emitted in narrower back-to-back cones, as expected in the naive quark

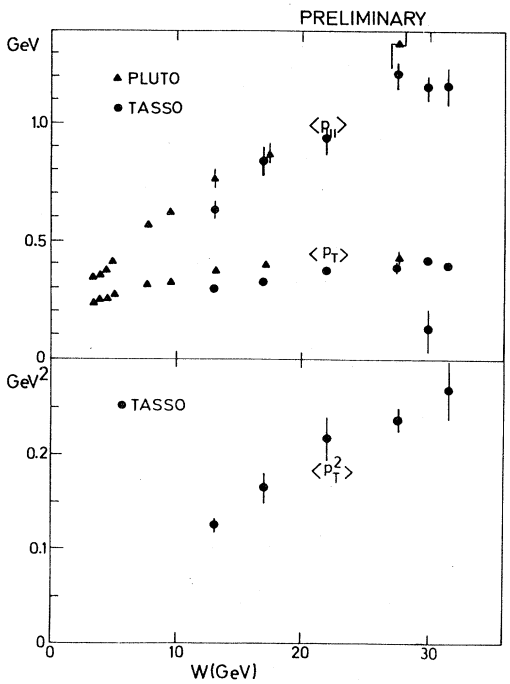

FIG. 61. The mean transverse and longitudinal momentum components $\langle p_t\rangle$, $\langle p_{||}\rangle$, and $\langle p_T{}^2\rangle$ for charged particles produced in hadronic events, plotted as function of the c.m. energy W.

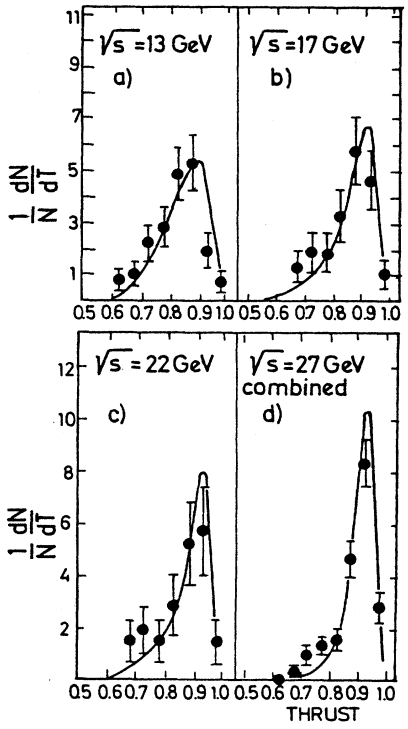

FIG. 62. Thrust distribution observed by the MARK-J group at $\sqrt{s}=$ (a) 13, (b) 17, (c) 22, (d) 27 GeV (see text). The solid line is the quark model prediction for u, d, s, c, and b quarks with no gluon emission.

model. The behavior of $\langle p_T{}^2\rangle$, a higher moment of the p_T distribution, is, however, in disagreement with the expectations of this model. The $\langle p_T{}^2\rangle$ rises with increasing energy by a factor of almost 2 over the energy range, while the naive quark model predicts an almost constant energy dependence.

For events in which the spatial momentum or energy distribution is isotropic, S and T are expected to approach 1 and 0.5, respectively. This would be the situation if, for example, the virtual photon materialized into two very heavy quarks, each with a mass close to the beam energy. Such quarks would be produced almost at rest. On the other hand, pairs of light quarks would

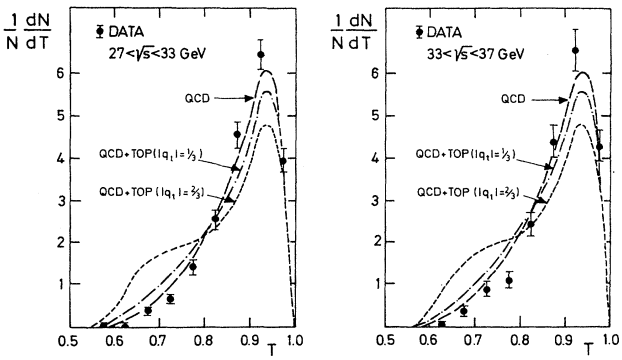

FIG. 63. The thrust distributions with a 70% energy cut for $\sqrt{s}\sim 30$ GeV and $\sqrt{s}\approx 35$ GeV. The curves are predictions for various models as described in the text.

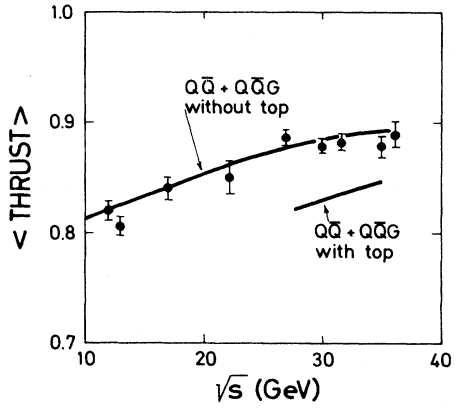

FIG. 64. Average value of thrust as a function of $\sqrt{s}$ together with the QCD prediction (solid line). The values expected from a QCD model with a top quark are also shown.

move at high speed and the Lorenz boost of their hadronic fragmentation products would result in the hadrons being produced in narrow jets collimated around the initial quark directions. Higher beam energies would result in narrower jets, so that S and T should approach the value 0 and 1, respectively. Thus, sphericity and thrust measurements can be used as sensitive methods to detect the presence of a new threshold due to new heavy quarks. Production of a new heavy quark would also result in increasing the average S and decreasing the average T as the energy is raised and the threshold passed.

The normalized thrust distributions of the MARK-J

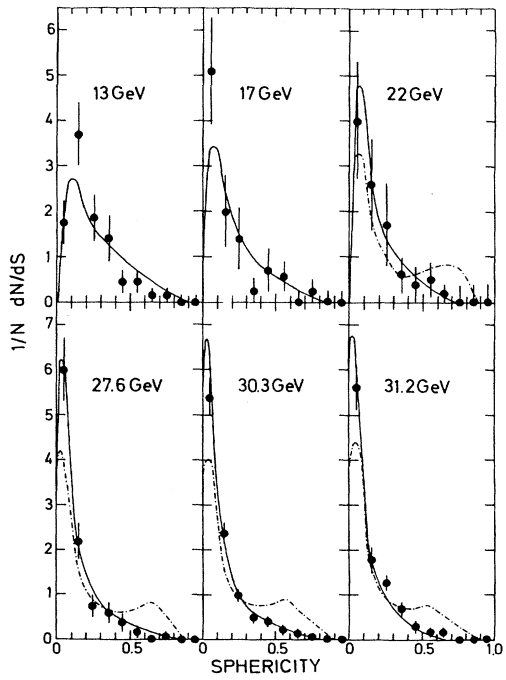

FIG. 65. Sphericity distributions for the energies $\sqrt{s}=13$ to 31.2 GeV. The solid line is the prediction of the QCD model with u,d,s,c,b quarks. The dashed-dotted curve includes a heavy-charge $\frac{2}{3}$ quark.

group $1/N$ (dN/dT) for 13, 17, 22, and the combination of 27.4 and 27.7 GeV data (labeled 27 GeV combined) are shown in Figs. 62(a)–62(d) along with the Monte Carlo predictions of a quark-parton model with u, d, s, c, and b quarks and no gluon emission (Barber *et al.*, 1979c,e, 1980b).

As expected for production of final states with two jets of particles, the distributions become narrower and shift toward high thrust with increasing energy.

Figure 63 shows the normalized thrust distributions (MARK-J) for combined data $27 \leq \sqrt{s} \leq 33$ GeV and $33 \leq \sqrt{s} \leq 37$ GeV. The curves show the Monte Carlo predictions with inclusion of gluons and also calculations which include charge $\frac{2}{3}$ and $\frac{1}{3}$ quarks produced as described previously. The QCD model without a top quark describes the data very well. One can also conclude that there is no evidence for production of a new heavy quark with charge $q = \frac{2}{3}e$.

Figure 64 shows the average thrust $\langle T \rangle$ plotted at nine PETRA energies. The solid curves are from Monte Carlo calculations which include u, d, s, c, and b quarks with gluon emission. The energy dependence of the data is smooth and shows none of the steps which would have appeared at new quark thresholds. The sphericity measurements of the TASSO collaboration in the energy range $\sqrt{s} = 13-31.2$ GeV are shown in Fig. 65. A top quark contribution (dashed-dotted curve in the figure) is clearly ruled out, and the data are well described by the quark model with u, d, s, c, and b quarks plus glon corrections. The average sphericity $\langle S \rangle$ measured at DORIS and PETRA by PLUTO and at PETRA by the JADE (Bartel *et al.*, 1979b) and TASSO groups is shown

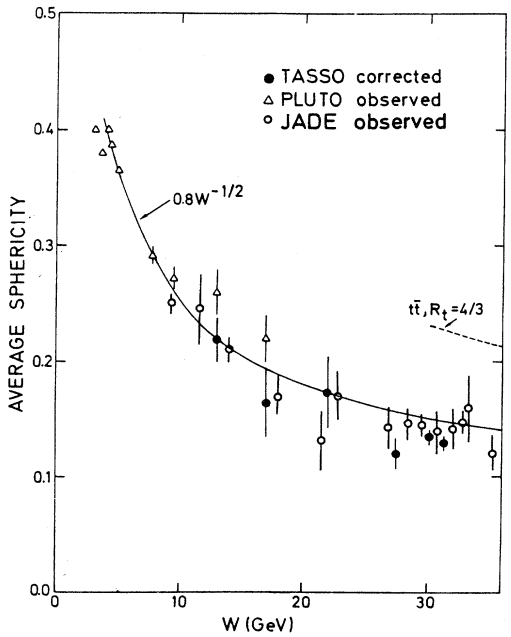

FIG. 66. Average sphericity $\langle S \rangle$ as function of the total c.m. energy W. The dashed line shows the expected $\langle S \rangle$ behavior when the threshold for the production of heavy t quarks is passed.

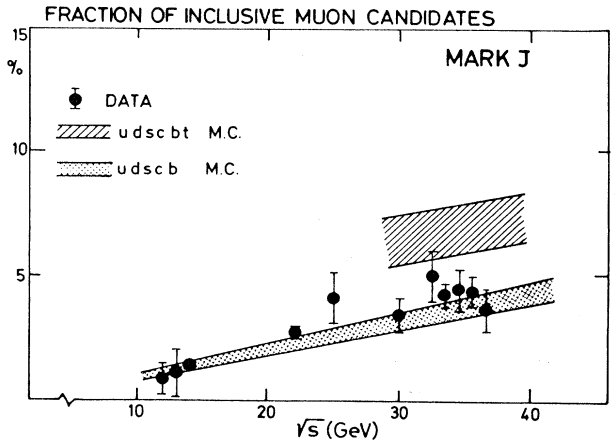

FIG. 67. Relative production rate of hadronic events containing muons as a function of the c.m. energy $E_{\text{c.m.}}$ The hatched areas are the predictions containing five and six quarks.

in Fig. 66 as function of $\sqrt{s}$. The quantity S is related with the jet cone half-opening angle δ by $S \approx 3/2\langle \delta^2 \rangle$. The solid line is the expectation from the naive model with five quarks. The dotted curve shows the expected threshold behavior after the appearance of the $t\bar{t}$ continuum, and the data clearly once again rule out their production.

2. Inclusive muons in hadronic events

In the framework of the six-quark model for the weak decays of heavy quarks, (c, b, and t) copious muon production is expected from the cascade decays $t \to b \to c$ (Kobayashi and Maskawa, 1973; Ali *et al.*, 1980a Ali, 1979). The onset of the production of a new heavy lepton would also lead to an increase in muon production. Thus, in addition to indications based on thrust and R

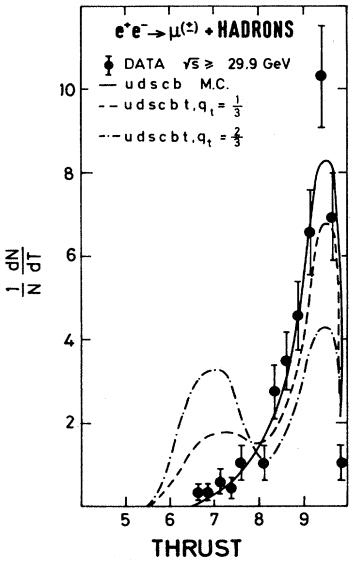

FIG. 68. Thrust distributions of inclusive muon events compared with all hadronic events from MARK-J (solid line).

measurements, a measurement of inclusive muon production in hadronic final states should provide a clear indication of the formation of top quarks or new leptons. All the hadron data for $\sqrt{s}$ from 12 to 36.7 GeV have therefore been analyzed and scanned in a search for muons.

Figure 67 summarizes the result of the MARK-J group (Duinker, 1981) for the relative production rate of hadronic events containing muons as a function of the c.m. energy. The figure demonstrates once again the absence of new heavy mesons containing t quarks up to 36.7 GeV. The observed rate agrees with the Monte Carlo predictions for five quark flavors but is more than five standard deviations away from the prediction which includes the top quark. Figure 68 shows the thrust distribution of the hadronic events containing muons compared with all the hadronic events. The scarcity of events at low thrust in the figure also rules out the existence of the top quark. The agreement between the data and the Monte Carlo prediction containing five quarks is good. With this distribution the production of a new quark with charge $q=\frac{1}{3}e$ is also ruled out. Below a thrust value of 0.75, 14 events are observed, and 13.8 are prediced by the QCD model containing five quarks and gluon bremsstrahlung. The calculation including an additional quark predicts 163 or 60 events for a charge of $\frac{2}{3}e$ or $\frac{1}{3}e$, respectively.

C. Weak decays of bottom quarks

The main source of prompt muons in hadronic events is decay products of bottom and charm quarks. Background contributions to the muon signal, arising from hadron punchthrough and decays in the flight of pions and kaons, have been calculated using a Monte Carlo simulation (Ali *et al.*, 1980a) to be ~2% of the hadronic events. The contribution of $\tau^+\tau^-$ events to the $\mu^\pm$ hadron sample becomes negligible when the total energy cuts and energy balance cuts are applied. The question can be asked whether it is possible to obtain event samples where the secondaries originate from the fragmentation of either $c\bar{c}$ or $b\bar{b}$ quark pairs. Figure 69 shows a calculation for the transverse momentum of the muons, P_t (transverse with respect to the thrust axis of the jet not containing the muon).

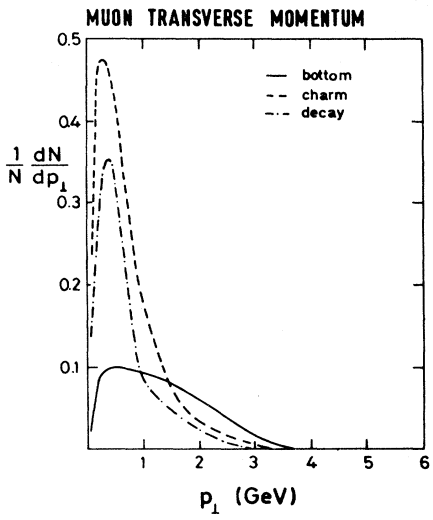

FIG. 69. Muon transverse momentum distributions as calculated by a Monte Carlo program for different sources of muons as indicated.

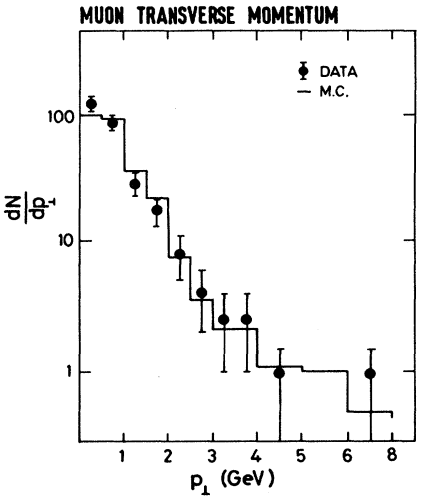

FIG. 70. The muon transverse momentum distribution as measured by the MARK-J group. The drawn histogram is a Monte Carlo calculation.

The P_t distribution for muons from c quark decays is peaked at relatively low momenta, while the distribution for muons from b decay is stretched out to higher values. Also indicated in this graph is the P_t distribution of the muons from π or K decay. By making a cut at 1 GeV, one obtains a sample of events dominated by muons from the decay of the b quark.

Figure 70 shows the muon P_t distribution for 234 events as measured by the MARK-J collaboration. A cut at 1.2 GeV leaves 48 events, of which ~45% are estimated to be due to b-quark decay. The preliminary result (Duinker, 1981; Branson, 1981) for the semileptonic branching ratio for mesons with a b quark denoted by B is found to be

$$\frac{(B\to\mu+x)}{(B\to\text{all})}=9.0\%\pm2.8\%\ (\text{stat.})\pm2.0\%(\text{syst})\ .$$

The large systematic error is due to the uncertainty of the punchthrough contribution. This result compares well with the results obtained at CESR (Bebek *et al.*, 1981; Chadwick *et al.*, 1981):

$$\frac{(B\to\mu+x)}{(B\to\text{all})}=9.4\%\pm3.6\%$$

and

$$\frac{(B\to e+x)}{(B\to\text{all})}=13.0\%\pm4.0\%\ .$$

Using their jet chambers, the JADE group has searched for secondary decay vertices near the primary

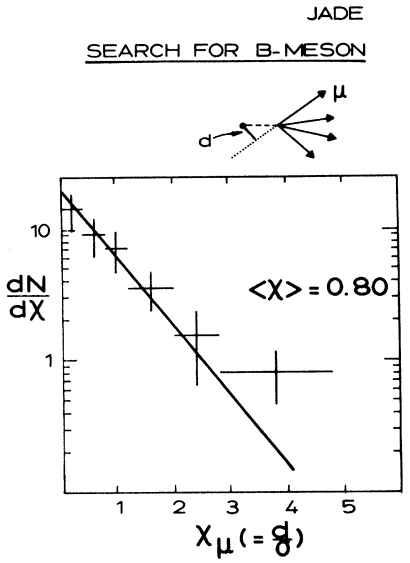

FIG. 71. Event distribution of the quantity χ_μ for the events containing a prompt muon.

vertex of the hadronic events containing a prompt muon (Bartel *et al.*, 1981a; Eichler and Haidt, 1981). By demanding that the muon momentum be greater than 1.8 GeV/c, they obtained an enriched sample of events from $b\bar{b}$ production.

The shortest distance d of the muon track to the primary vertex is a sensitive parameter to find a possible secondary vertex. In Fig. 71 the quantity $\chi_\mu = d/\sigma$ is plotted where σ is the resolution of the method derived by studying the tracks of pure hadron events. No change in slope is seen in this distribution, and $\langle \chi_\mu \rangle$ is found to be 0.80. From this average value of χ_μ an upper limit for the length $d_\mu < 790$ μm at 90% C.L. is derived. This result can be converted into an upper limit of the lifetime of mesons containing a b quark. The JADE group finds

$$\tau_b < 5.10^{-12} \text{ sec} \quad (90\% \text{ C.L.}) .$$

In the standard six-quark model of Kobayashi and Maskawa the mixing of the three left-handed quark doublets

$$\begin{bmatrix} u \\ d \end{bmatrix}, \quad \begin{bmatrix} c \\ s \end{bmatrix}, \quad \text{and} \quad \begin{bmatrix} t \\ b \end{bmatrix}$$

is related to three angles α, β, and γ, where α is the normal Cabibbo angle. The transition rate of $b \to u$ quarks is proportional to $\sin\beta$ in this model, and the transition $b \to c$ to $\sin\gamma\cos\beta$. The lifetime of the b quark can be expressed as a function of the angles β and γ according to (Eichler and Haidt, 1981)

$$\tau_b = \frac{10^{-14}}{2.74\sin^2\gamma + 7.7\sin^2\beta} \text{ sec} .$$

This relation will be represented in the $\sin\beta$-$\sin\gamma$ plane by an ellipse, as is shown in Fig. 72. The bound on $\sin\beta$ in this figure is derived from the existing knowledge of the Cabibbo angle. The bound on $|\sin\gamma|$ is determined

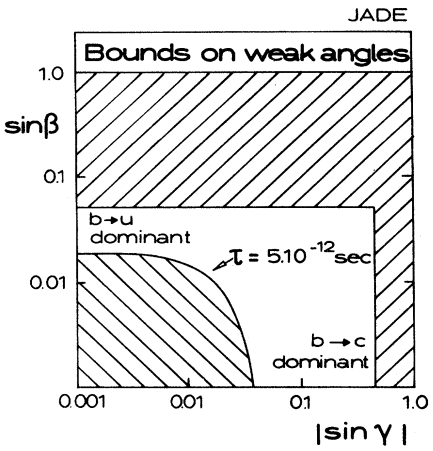

FIG. 72. The $\sin\beta$-$\sin\gamma$ plane with the existing bounds on these angles. The ellipse $\tau_b = 5.10^{-12}$ sec is also indicated.

by the error on the value of the mass difference between the K_S^0 and the K_L^0. Also indicated in the plot are the regions where the transition $b \to c$ or $b \to u$ would be dominant. The hatched area at small angles is the bound found by the JADE group.

D. Free quark searches

The MARK II group (Weiss *et al.*, 1979) at SPEAR has searched in their 1.4×10^6 e^+e^- annihilation events for particles with a mass in the range 1 to 3 GeV/c^2 and charge $q = -1e$ and $-\frac{2}{3}e$. Particles originating from the interaction point have their time of flight measured by a system of trigger counters. Combining the time measurement with the apparent momentum measurement P_q, one can determine a mass

$$m_T^2 = \frac{P_q^2}{q^2}(1/\beta^2 - 1) = \frac{m_q^2}{q^2} ,$$

where $\beta = v/c$. Figures 73(a) and (b) display the observed spectrum of time-of-flight masses m_T^2 for positively and negatively charged particles. In the positive

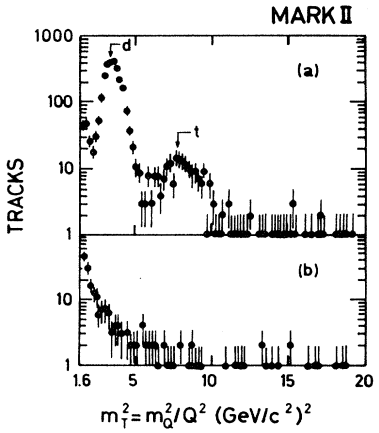

FIG. 73. The apparent mass squared m_T^2 for (a) positive and (b) negative particles as measured by the MARK II detector.

particle spectrum, deuterons and tritons are observed produced in beam-gas collisions. This spectrum can serve as a calibration for the detection of negatively charged particles ($\bar{d}$ and $\bar{t}$ are not observed). Upper limits can be derived in the mass regions of $1-3$ GeV/c^2 for the production of $q=-1$ particles, assuming an exponential momentum distribution. Expressing the limits in terms of $R_q=\sigma(e^+e^-\to q\bar{q})/\sigma(e^+e^-\to\mu\mu)$, the MARK II group finds for

$$m_q=1.7-2.3\ \text{GeV}/c^2,\quad R_q\leq 3.1\times10^{-4}$$

and

$$m_q=2.3-3.0\ \text{GeV}/c^2,\quad R_q\leq 1.9\times10^{-3}$$

at the 90% C.L.

In the search for $q=\frac{2}{3}e$ particles use is made of the pulse-height measurements of the trigger counters. The calibration is done with muon pairs and electrons from Bhabha scattering. Two sets of limits are found for the production of quarks: (1) the exclusive production of quark-antiquark pairs, giving rise to two nearly collinear tracks in the detector, and (2) the inclusive production of quarks, in which case a quark within a hadron jet is searched for. The limits found, expressed as the fraction of the pointlike muon pair cross section R_q are shown in Fig. 74 as function of mass.

The JADE group, using their jet chamber, a cylindrical drift chamber filled with an argon, methane, isobuthane mixture at a pressure of 4 atm, is able to identify particles by a simultaneous measurement of the mean energy loss and the apparent momentum (Bartel *et al.*, 1980d). The inclusive production of quarks with $q=\frac{2}{3}e$ and $\frac{1}{3}e$ is studied. The limits found by this group are shown in Fig. 74 for the two cases. For each case two limits are presented, one for an exponential and another for a flat momentum distribution for the produced quarks.

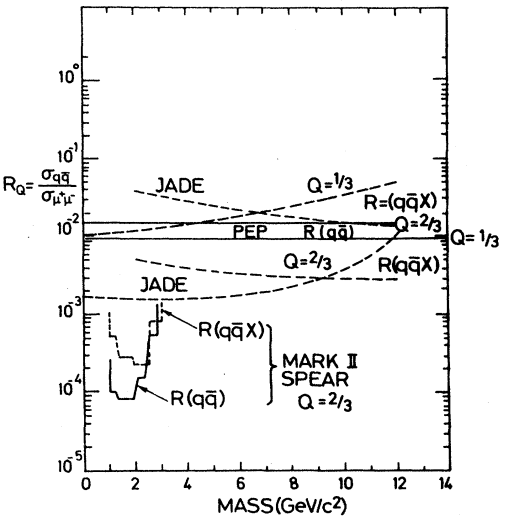

FIG. 74. The 90°-C.L. upper limits from various quark searches expressed in R_q as a function of mass.

At the 1981 Lisbon conference the first results of an experiment at PEP especially devised for quark searches, were presented by Ely (Marini *et al.*, 1981). These limits are also shown in Fig. 74.

E. Searches for new particles

1. Heavy leptons

Following the initial searches (Bernardini *et al.*, 1973; Orito *et al.*, 1974) for the τ lepton, the discovery (Perl *et al.*, 1975; Feldman *et al.*, 1977) and further study of its properties (Burmester *et al.*, 1977a, b; Fluegge, 1979a; Brandelik *et al.*, 1980b), there has been great interest in searching for a new heavy lepton, which would extend the series e, μ, τ. One assumes that, analogous to the τ lepton, a new heavy lepton HL will couple universally to leptons and quarks according to the standard $V-A$ weak-interaction theory and have the following decay modes (in percentages): $\tau^-\bar{\nu}_\tau\nu_{\text{HL}}$ (9.2), $\mu^-\bar{\nu}_\mu\nu_{\text{HL}}$ (10.6), $e^-\bar{\nu}_e\nu_{\text{HL}}$ (10.6), and hadrons $+\nu_{\text{HL}}$ (69.6). The branching ratios (Tsai, 1979), which are mass dependent, are given here for a heavy-lepton mass of 14 GeV. Owing to their large mass and low velocity, the decay products would be expected to have large angles with respect to the HL line of flight. This contrasts to the decay products of the τ at PETRA energies, which are tightly collimated.

Heavy-lepton production is recognized in the MARK-J detector for events in which one lepton decays into a muon and neutrinos and the other lepton decays into hadrons and neutrinos. Hadrons are detected by their energy deposit, E_{vis}, in the calorimeter (Barber *et al.*, 1980b).

Heavy-lepton candidates with masses greater than 6 GeV are selected by applying criteria involving cuts on the total deposited energy, the acoplanarity, the charge multiplicity of the events, and the total amount of hadronic energy and its direction. No events were observed

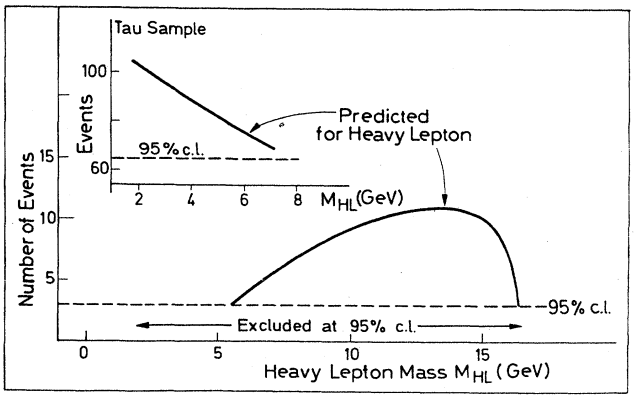

FIG. 75. Number of events expected by the MARK-J group for the production of a new (sequential) heavy lepton as a function of mass. The inset shows the number of events expected in the τ sample from τ and heavy-lepton production. A total of 52 τ events is observed. The dashed line corresponds to the 95% confidence upper limit for τ events.

in the data with $33 < \sqrt{s} < 36.7$ GeV, corresponding to a time-integrated luminosity of 6.9 pb^{-1}. The number of events predicted by a Monte Carlo calculation as a function of the heavy-lepton mass M_{HL} is shown in Fig. 75 along with the 95% confidence level upper limit from the data. Figure 75 demonstrates that the existence of a sequential heavy lepton with a mass between 6 and 16 GeV is excluded.

Heavy leptons with $M_{HL} < 6$ GeV would decay into final states similar in appearance to those from τ decay, and would tend to be included in the sample of $e^+e^- \to \tau^+\tau^-$ events. The inset in Fig. 75 shows the Monte Carlo prediction for the total number of events in the sample from $e^+e^- \to \tau^+\tau^-$ (Barber *et al.*, 1980d) and from heavy-lepton production, as a function of M_{HL}. The inset demonstrates that the predicted number of heavy-lepton events exceeds by more than two σ the number of observed τ events. Therefore, with more than 95% confidence they exclude the existence of the heavy lepton with mass $M_{HL} < 6$ GeV. One is thus able to rule out the existence of a new heavy lepton for a $M_{HL} < 16$ GeV.

The criteria employed by the PLUTO group (Berger *et al.*, 1981c) for finding heavy leptons are very similar to the ones mentioned above, and they find a limit for M_{HL} of 14.5 GeV.

The TASSO group (Brandelik *et al.*, 1981) searches for a single charged particle recoiling against many hadrons. The angle between the single or "lone" track and the nearest neighbor is plotted in Fig. 76. A new heavy lepton would give an excess of events in this plot at large angles. From the actual observed number, taking into account the background from hadron production, an upper limit on the mass is found to be $M_{HL} < 15.5$ GeV at 90% C.L.

The JADE group concentrates on the possible hadronic decays of the heavy leptons. They calculate the direction of the two hadron jets and demand that the jets be very acoplanar, excluding by such criteria the events produced by quark-antiquark pairs which give rise to two back-to-back jets. They expect for a 17-GeV lepton $\sim$ 10 events, and they find none (Cords, 1980).

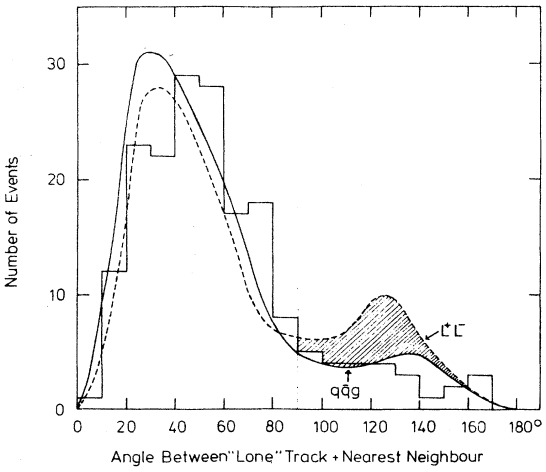

FIG. 76. The distribution of the angle between the lone track and the nearest neighbor as measured by the TASSO collaboration. The prediction of the production of a heavy lepton is indicated by the dashed line. The QCD expectation is given by the solid curve.

2. Heavy neutral electrons

The JADE collaboration has searched for a heavy neutral partner of the electron. These particles appear in nonstandard models of the weak interaction (Bletzacker and Nieh, 1977). When the neutral current contains nondiagonal terms, they can be produced in neutrino and e^+e^- interactions. In models where only diagonal terms are present to describe the neutral current the heavy neutral leptons can be produced in e^+e^- interactions only according to

$$e^+e^- \to \bar{E}^0 + \nu_e \quad \text{and} \quad e^+e^- \to \bar{E}^0 + E^0 .$$

Depending on the coupling of the charged current to these particles, which can be either $V-A$ or $V+A$, the differential cross sections for the case of an exchange of a charged weak boson in the t channel can be written as

$$\frac{d\sigma^{V-A}}{d\Omega \bar{E}^0}_{(E^0)} = \frac{G_F^2}{32\pi^2}\left[1-\frac{M^2}{s}\right]\left[\frac{1}{1-(q^2/M_w^2)}\right]$$

$$\times[2s(1\pm\cos\theta)-(s-M^2)\sin^2\theta] ,$$

$$\frac{d\sigma^{V+A}}{d\Omega \bar{E}^0} = \frac{G_F^2}{32\pi^2}\left[1-\frac{M^2}{s}\right]\left[\frac{4s}{1-(q^2/M_w^2)}\right] ,$$

where G_F is the Fermi coupling constant, M the mass of $\bar{E}^0$ or E^0, M_w the mass of the exchanged charged weak boson, q^2 the momentum transfer in the t channel, and θ the angle between the beam direction and the produced $\bar{E}^0$. The possible decay channels for the E^0 are $E^0 \to e^+e^-\nu_e$ (10%), $e^-\mu^+\nu_\mu$ (10%), $e^-\tau^+\nu_\tau$ (10%), $e^-u\bar{d}$ (35%), and $e^-c\bar{s}$ (35%), respectively.

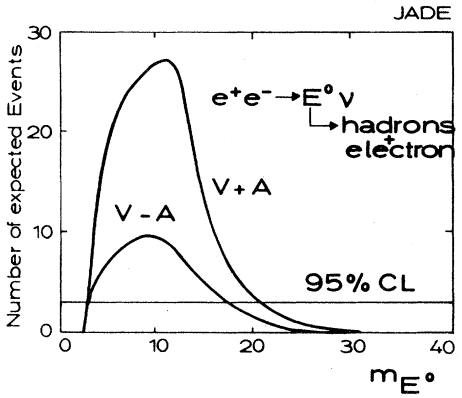

FIG. 77. The number of expected events for heavy neutral lepton production as a function of the mass. The 95%-C.L. line is also indicated.

The JADE group (Takeda, 1981) searched for the events produced via t-channel exchange and for hadronic decays of the lepton. As a ν_e is always produced in such a reaction, the signature of the events is the imbalance of energy and momentum along the line of flight of the neutrino. The experimental cuts were made such that the event had an empty cone (half-opening angle 50°) containing no charged particles or neutral energy, opposite to a hadronic jet containing one electron.

The expected number of events as a function of the mass are presented in Fig. 77 for the $V+A$ and $V-A$ case. One event was found which could be due to $\tau^+\tau^-$ production. From the 95% C.L. limit it can be concluded that the neutral heavy leptons do not exist below 18 GeV if the coupling is $V-A$ or below 20 GeV if the coupling is $V+A$.

3. Scalar electrons and muons

In the framework of supersymmetric theories (Gol'fand and Likthman, 1971; Wess and Zumino, 1974; Fayet and Ferrara, 1977; Fayet, 1977, 1979a, b; Farrar and Fayet, 1978a, b, 1980), spin-zero partners of the electron and muon are expected to decay only according to the reactions

$$s^- \rightarrow e^-(\mu^-) + \text{photino (goldstino)} ,$$

$$t^- \rightarrow e^-(\mu^-) + \text{antiphotino (antigoldstino)} ,$$

where s and t are the spin-zero partners of the electron (muon) associated with the left- and right-handed parts of the electron (muon) field, respectively, and the photino and goldstino are the spin-$\frac{1}{2}$ partners of the photon and the goldstone boson. Since s and t carry unit electric charge, they may be produced in pairs in e^+e^- annihilation according to the cross section

$$\frac{d(e^+e^- \rightarrow s^-s^+ \text{ or } t^-t^+)}{d(\cos\theta)} = \frac{\pi\alpha^2\beta^3\sin^2\theta}{4s};$$

$$\beta = \left[1 - \left[\frac{m}{E}\right]^2\right]^{1/2} ,$$

which is characteristic of spin-zero particle production. m is the mass of s or t, E is the beam energy, and θ is the scattering angle.

Because of the uniqueness of the decay reactions and the extremely short lifetimes of s and t and the prediction that the interaction cross sections of photino and goldstino are expected to be very small, only electron and muon pairs are observed in the final state. Near threshold production of s and t, the two residual electrons or muons would be produced isotropically in space. Data from SPEAR place a lower limit of 3.5 GeV (Heile *et al.*, 1978) on the mass of s and t. Thus over the PETRA energy range of 12 and 36.7 GeV an increase in the production of acoplanar electron-positron or muon pairs should be observed if a new threshold is passed.

The event selection criteria used by the PETRA groups to obtain upper limits for the production of these particles are based on the considerations mentioned above. I will describe the procedure followed by the CELLO group in some detail (Behrend *et al.*, 1981b). At an average beam energy $\langle E_b \rangle = 17.3$ GeV the events triggered by at least two charged particles were subjected to the following cuts:

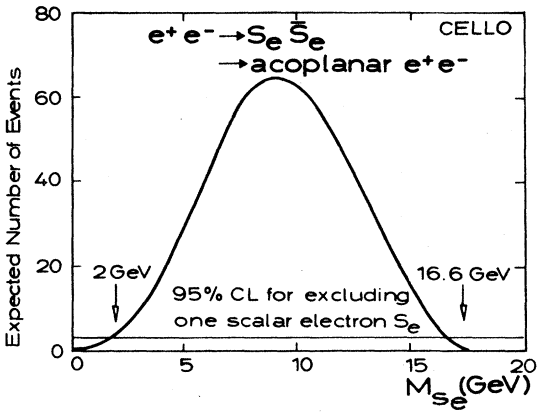

FIG. 78. Number of events expected for the production of a spin-zero partner s_e or t_e of the electron as a function of mass. The upper limit of events (95% confidence) and the mass range excluded are also indicated.

(1) The angle θ between the tracks and the beam direction was constrained to be $35° < \theta < 145°$.

(2) The acoplanarity was less than 30°.

(3) The charged track multiplicity was less than 5.

(4) Two tracks had a momentum greater than 0.8 GeV.

(5) For e^+e^- pairs the sum of the energies had to exceed 5 GeV, and for $\mu^+\mu^-$ pairs the momentum of the muon had to be greater than 20% of the beam energy.

In the CELLO detector the electrons and photons are identified with a lead-liquid argon calorimeter and the muons with proportional chambers behind 80 cm of iron. No candidates were found. Figure 78 shows the expected event rate for the e scalar leptons under the above-mentioned conditions. At the 95% C.L. the mass range $2 < M_s < 16.6$ GeV is excluded. Similar limits were obtained by the other PETRA experiments (Barber *et al.*, 1980a; Berger *et al.*, 1981c).

4. Hyperpions

In order to avoid the necessity of postulating the existence of Higgs particles, which had been introduced to give masses to gauge bosons, Weinberg (1979) and Susskind (1979) independently demonstrated the possibility of generating the W and Z° boson masses by introducing a hypercolor. Heavy quarks are introduced—e.g., U and D—which can form so-called hyperpions. These hyperpions could be produced in e^+e^- interactions (Ali and Beg, 1981; Ali *et al.*, 1981; Ali, 1981) at relatively low energies, as their masses could be quite small.

The cross-section behavior of their production is the same as that of other spin-zero particles (see Sec. VI.E.3 on scalar electrons and muons). Possible decay modes are

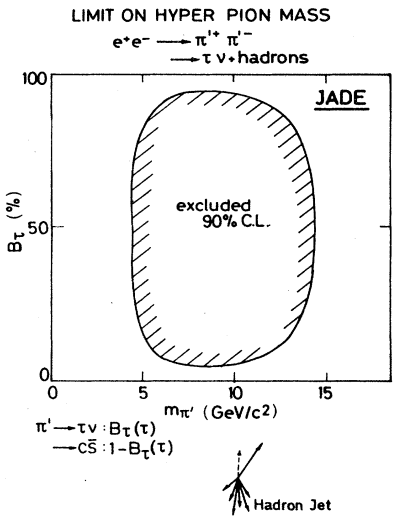

FIG. 79. Limit on the mass of the hyperpions as found by the JADE group. Plotted is the mass as a function of B_τ. The contour gives the 90% C.L. in the plane. The inside of the contour is the region ruled out by the data.

$$\pi' \rightarrow \tau\nu_\tau \text{ or } \pi' \rightarrow c\bar{s} \rightarrow \text{hadrons} .$$

As the branching ratio for these two decays is not known, the JADE group (Takeda, 1981) searched for these particles as function of the branching ratio to $\tau\nu_\tau(B_\tau)$. The events looked for are the ones where one hyperpion decays to a τ lepton, which subsequently decays to one charged particle plus neutrinos. Opposite to the charged particle but accollineair with it one searches for a hadronic jet originating from the decay of the π' to $c\bar{s}$ quarks. This method of searching breaks down if B_τ is close to one or zero. Figure 79 shows the result of the JADE group. The mass of the hyperpion is plotted as a function of B_τ. The two-dimensional region which is excluded at 90% C.L. is indicated. Hyperpion masses from 5 to 15 GeV are excluded by this search.

5. Axions

In order to give an explanation for the experimentally observed CP conservation in strong interactions (Peccei and Quinn, 1977a, b; Weinberg, 1977; Wilczek, 1978), the existence of a very light boson called the axion has been postulated. These particles could be produced in beam dump experiments (Faissner *et al.*, 1981) and also in the decay of a vector meson such as $J/\psi \rightarrow \gamma + a$.

Porter (1981) has reported the search for this decay of the J/ψ resonance using the Crystal Ball detector at SPEAR. This detector is constructed especially to detect γ rays with high accuracy.

The axion behaves like a neutrino, so it escapes direct detection. As the mass is supposed to be very small, one can look for photons at ~ 1.5 GeV without anything else being observed in the detector. The photon has of course to be in time with the crossing of the electron and positron bunches at the intersection point. The total number of J/ψ decays for this search were $1.43 \cdot 10^6$ events.

The branching ratio of $J/\psi \rightarrow \gamma + a$ was estimated to be $\sim 5 \cdot 10^{-5}$. Five candidate events were found, but they could all be attributed to cosmic-ray events' hitting the detector from the sides. The upper limit for the branching ratio $J/\psi \rightarrow \gamma + a$ was found to be $< 3 \cdot 10^{-5}$ at 90% C.L.

6. Excited states of the muon

Heavy muons, excited states of the muon, could in principle be produced in e^+e^- interactions. Their production could proceed according to

$$e^+e^- \rightarrow \mu^{*\pm} + \mu^{\mp} \text{ or } e^+e^- \rightarrow \mu^{*-} + \mu^{*+} .$$

The μ^* subsequently would decay according to $\mu^{*\pm} \rightarrow \mu^{\pm} + \gamma$.

For the simplest case of spin-$\frac{1}{2}$ the differential cross section could be written as

$$\frac{d\sigma}{d\Omega} = \lambda^2\alpha^2 \frac{(s-M^2)^2}{s^3} [(s+M^2) - (s-M^2)\cos^2\theta] ,$$

where λ is a new coupling constant, α the fine-structure constant, M the mass of the μ^*, and s the square of the center of mass energy. The MARK-J group (Branson, 1981; Duinker, 1981) has looked for events with two muons and one photon in their detector using the following criteria:

(1) Two identified and momentum-analyzed muon tracks.

(2) One hard photon with an energy greater than 20% of the beam energy.

(3) A greater than 20° angle between the photon and the beam direction.

(4) The event's satisfying a kinematical fit in order to insure energy and momentum conservation within errors.

(5) The muon tracks, acoplanarity's being greater than 20°. The data used for the search were 12.34 pb^{-1} obtained at energies ranging from $27.4 < \sqrt{s} < 36.7$ GeV. Possible background comes from radiative processes such as

$$e^+e^- \rightarrow \mu^+\mu^-\gamma$$

and from two-photon processes

$$e^+e^- \rightarrow \mu^+\mu^- e(e) ,$$

where one of the electrons stays within the beam pipe and the other is scattered into the detector and cannot be distinguished from a photon. Using Monte Carlo programs developed by Berends, Kleiss, and Vermaseren, the researchers estimated the background to be 12 events, in good agreement with the number of observed events of 11. This result can be expressed as the maximum allowed cross section for $\mu^*\mu$ production, $\sigma^{\max}_{\mu^*\mu}$ at the 90% C.L. limit. In Fig. 80 the mass of the μ^* is plotted versus the cross-section ratio $\sigma_{\mu^*\mu}/\sigma_{\mu\mu}$ (right-hand side vertical scale). The 90% C.L. line is drawn as a solid

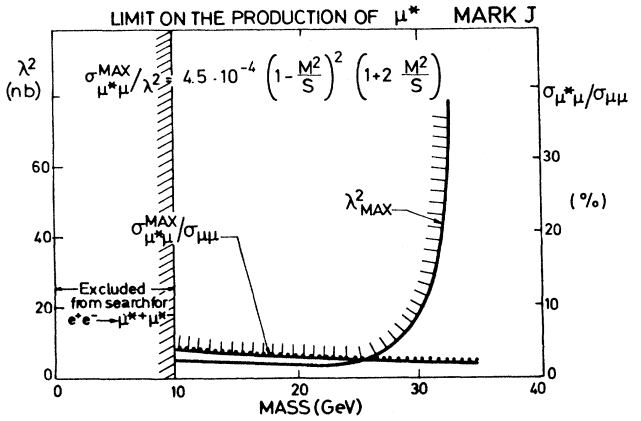

FIG. 80. Limit on the production of the μ^* from the MARK-J group. The right-hand scale is the cross section for $\mu^*\mu$ production over the $\mu\mu$ cross section in percentage. The left-hand vertical scale is the coupling strength. The solid-dotted curve is the upper limit at 90% C.L. for $\sigma_{\mu^*\mu}/\sigma_{\mu\mu}$. The solid curve is the 90% C.L. for the coupling denoted with λ_{max}^2. The region excluded below 10-GeV mass of the μ^* is also indicated.

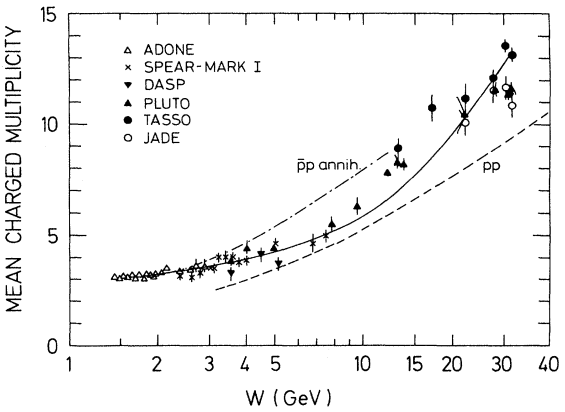

FIG. 81. Measurements of the mean charged multiplicity $\langle n_{ch}\rangle$ as a function of the c.m. energy $\sqrt{s}$.

dotted curve.

A bound on the coupling λ can be found using the relation

$$\sigma^{max}_{\mu^*\mu}/\lambda^2 = 4.5\cdot10^{-4}\left[1-\frac{M^2}{s}\right]\left[1+2\frac{M^2}{s}\right].$$

The solid line (left-hand vertical scale) shows the maximum allowed coupling for μ^* production. At the lower masses the bound on μ^* production is obtained by searching for $\mu^*\mu^*$ production in events with two muons and two photons in the final state. Figure 80 demonstrates that the existence of μ^* particles is excluded up to masses of 30 GeV if the coupling is not too small.

F. Multiplicity distributions, inclusive particle spectra, and particle yields

1. Multiplicity distributions

At low energy the charged multiplicity distributions for the hadronic events produced in e^+e^- interactions have been measured at ADONE (Bacci *et al.*, 1979), SPEAR (Siegrist, 1980), and DORIS (Berger *et al.*, 1978b; Brandelik *et al.*, 1979d). The mean charged multiplicity was found to behave in agreement with the Feynman scaling hypothesis (Feynman, 1969) and to increase logarithmically according to

$$\langle n_{ch}\rangle = a + b\ln s \qquad (23)$$

in the energy range 1.4 GeV $\leq\sqrt{s}\leq$ 7 GeV.

The first evidence from the TASSO group (Brandelik *et al.*, 1980a) indicated that the quantity $\langle n_{ch}\rangle$ was rising much faster in the PETRA energy range than expression (23) could describe. They observed an increase of $\sim$4 charged particles more than the extrapolation of the low-energy fit to the data with expression (23) could account for. The drastic change could not be due to $b\bar{b}$ production above threshold, as a change of only $\sim$0.2 is expected from the additional production of these quarks.

The data for $\langle n_{ch}\rangle$ at the lower energies combined with the measurements of the JADE, PLUTO, and TASSO (Timm, 1980; Pandoulas, 1980; Berger *et al.*, 1980a, e) groups are shown in Fig. 81. Included in the data points are the charged pions from K_s^0 decay, a contribution of $\sim$0.7 units in $\langle n_{ch}\rangle$. A possible explanation for the fast rise is the gluon effects observed at the highest PETRA energies (see Sec. VII). In QCD the multiplicity is expected (Furmanski and Pokorski, 1979; Bassetto *et al.*, 1978) to behave as

$$\langle n_{ch}\rangle = a + b\exp[c(\ln s/\Lambda^2)^{1/2}].$$

A fit to all the data (solid line in the figure) with $\Lambda=0.5$ GeV yields $a=2.38\pm0.09$, $b=0.04\pm0.01$, and $c=1.92\pm0.07$. Due to relatively large error bars other simple functions like $a(\ln s)^2$ or an exponential like as^b fit the trend of the data equally well (Timm, 1980). The question of which sort of particles, of low or intermediate momentum, causes the rise in average multiplicity will be answered in the next paragraph.

2. Single-particle spectra and particle yields

The TASSO collaboration (Brandelik *et al.*, 1980f, Pandoulas, 1980) investigated the energy behavior of the scaling cross section $s\cdot d\sigma/dx$ as a function of the Feynman variable $x=p/p_{beam}$, where p is the momentum of the produced hadron. If scale invariance holds, $s\cdot d\sigma/dx$ should be independent of the c.m. energy. The data measured at 12, 27.4–31.6, and 35.0–36.6 GeV by this group are shown in Fig. 82. For $x\geq0.2$ the data are the same within errors and agree with those measured at low energy by DASP (Brandelik *et al.*, 1979d) and SLAC-LBL (Feldman and Perl, 1977) within 30%. However, at low x values a dramatic rise for increasing c.m. energy is seen. As the only energy-dependent quantity in the in-

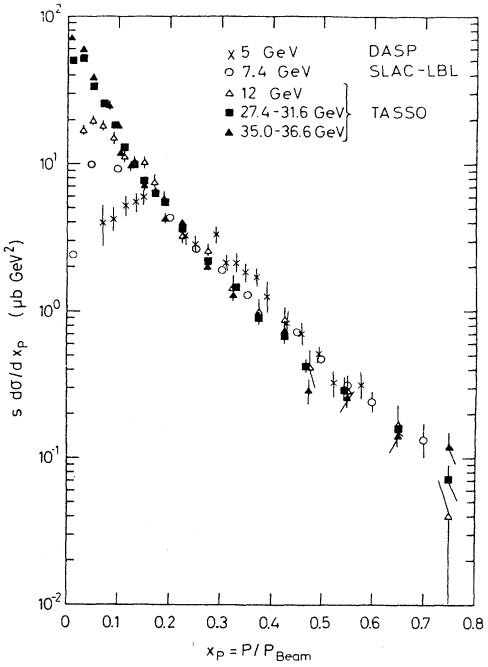

FIG. 82. The $s\,d\sigma/dx$ distribution as a function of $x=p/p_{\text{beam}}$ for charged particles in the c.m. energy range of 5 to 36.6 GeV.

tegrated function $\int s\cdot d\sigma/dx$ is the quantity $\langle n_{\text{ch}}\rangle$, this rise is related to the one seen in the average multiplicity. This scale breaking when interpreted in terms of QCD can be explained by the emission of gluons, namely, the primary momentum is now shared at low x values. This effect should become more pronounced as the energy becomes larger, and at 30 GeV one expects (Baier *et al.*, 1979; Frazer and Gunion, 1979) the data for $x=0.2$ to be 10% higher than at 5 GeV. At $x=0.7$ the data should be 20% lower compared with the low-energy data. The data at present are not precise enough to test these predictions.

With the JADE and TASSO detectors one is able to distinguish $\pi^{\pm}$ from $K^{\pm}$, protons, and antiprotons. The x spectra for the different particle types have been measured over a wide x range. In Fig. 83(a), (b), and (c) the preliminary scaling cross sections $(s/\beta)\cdot d\sigma/dx$ are shown, where $x=2E/W$, for $\pi^{\pm}$, $K^{\pm}$, and $(p,\bar{p})$. The pion and kaon data are compared to low-energy data. For $x\geq 0.2$ the 5.2 GeV pion spectra are above the high-energy ones by $\sim 30\%$, which is the expected outcome from scale breaking. The statistical error for the high-energy data, however, is still large, so this conclusion is only tentative. In Fig. 83(b), the kaon spectra are shown. The solid line represents the high energy $\pi^+ + \pi^-$ data. The yield of kaons is a factor 2 to 4 lower than the $\pi^{\pm}$ yield; at higher x values, however, the difference becomes smaller.

The particle fraction is shown in Fig. 84 as a function of the particle momentum p. The data from JADE and TASSO are combined in this graph. Results in the momentum range where the dE/dX measurements of

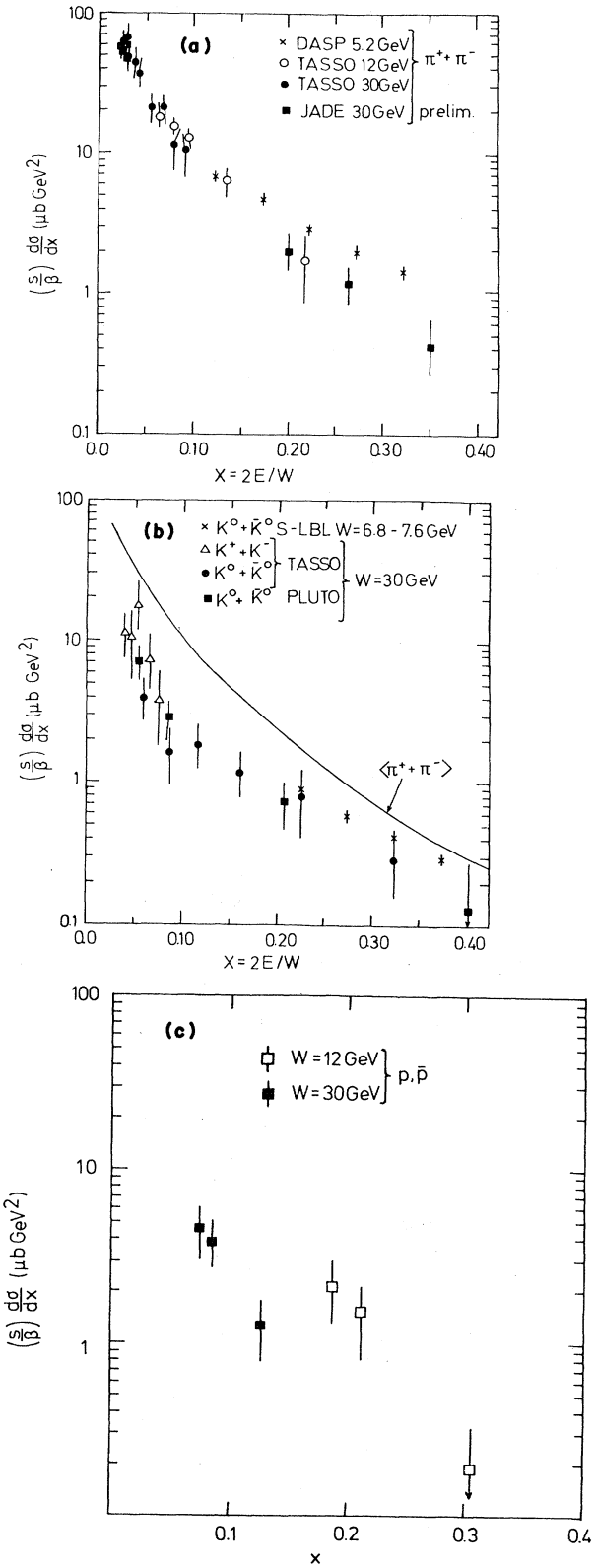

FIG. 83. (a) The $(s/\beta)d\sigma/dx$ distribution as a function of $x=2E/W$ for the pion data at several c.m. energy values. (b) As (a) but for charged and neutral kaons. The solid line is the trend of the charged pion data. (c) As (a) but for protons and antiprotons.

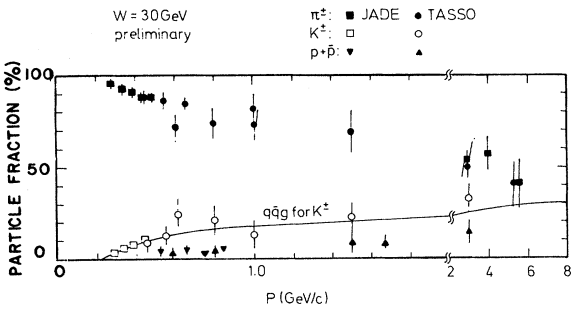

FIG. 84. The particle fraction at $\sqrt{s}=30$ GeV for $\pi^{\pm}$, $K^{\pm}$, and $p+\bar{p}$ as a function of particle momentum. The solid line is the prediction by QCD.

JADE are in the "relativistic rise" region are shown around 3–5 GeV. The first results from the TASSO Čerenkov counters are also included. At low momentum, below 1 GeV the pions completely dominate; however, at around 3 to 5 GeV the pions are reduced to ~50%, the kaons are ~35% and $(p,\bar{p})$ are ~15%. The solid line is the prediction of QCD. An average event of $\sqrt{s}=30$ GeV has approximately $11\pi^{\pm}$, 1.4 K^0, $\bar{K}^0$, 1.4 $K^{\pm}$, and 0.4 $p,\bar{p}$ in the final state (Brandelik *et al.*, 1980c,f).

VII. TEST OF QCD

A. Introduction

In the framework of QCD, the process $e^+e^- \rightarrow$ hadrons proceeds through the production of a quark-antiquark pair, which is sometimes accompanied by one or more gluons.

The consequences of gluon radiation in e^+e^- physics were seen before the advent of PETRA by the experiments at DORIS (Berger *et al.*, 1978a; Bienlein *et al.*, 1978; Darden *et al.*, 1978a) which observed the decay of the Υ. In particular, the PLUTO collaboration (Meyer, 1979) demonstrated that a variety of topological features of the events were in excellent agreement with Monte Carlo model predictions based on the direct decay of the Υ via three gluons into three broad jets. The quantity thrust is shown in Fig. 85(a) and (b) as measured on and off resonance. These distributions are clearly distinct from each other; off resonance an excellent agreement with the $q\bar{q}$ model is obtained. At resonance the three-gluon decay is favored if compared with phase-space-like decays of the Υ. Figure 86 shows the angular distribution of the thrust axis corrected for detector and hadronization effects. The data are consistent with the prediction for vector gluons (solid line) but inconsistent with the prediction of scalar gluons (dashed line). This result provides clear evidence against scalar gluons.

This analysis, however, was not able to prove unambiguously the existence of gluon jets. The Υ mass is not high enough to produce three well-collimated jets which can be clearly distinguished from other resonant decay channels, so that a statistical model including clusters of

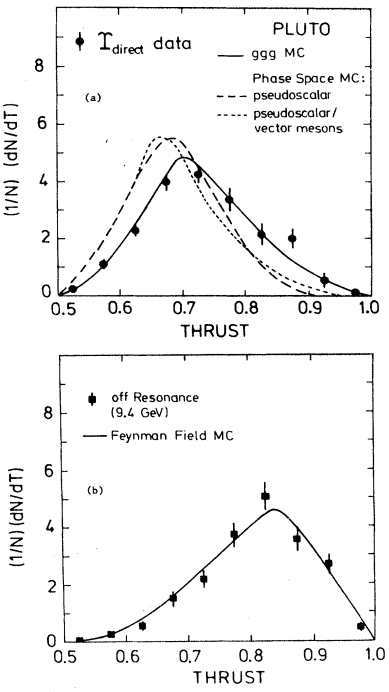

FIG. 85. Distributions of observed thrust for (a) Υ-direct and (b) off-resonance events compared with various model calculations.

resonances could not be ruled out.

The PETRA results on tests of QCD will be reviewed in the next sections for each of the groups. The chronological sequence of mounting evidence leading to the establishment of gluon effects in e^+e^- interactions has been reported elsewhere (Duinker and Luckey, 1980; Ellis, 1981; Schopper, 1981).

Some of the main features established by the summer of 1979 (Wiik, 1979; Soeding, 1979; Barber *et al.*, 1979c, d, g; Brandelik *et al.*, 1979b; Berger *et al.*, 1979d; Bartel *et al.*, 1980a) can be summarized as follows: The naive two-jet picture at the then-highest PETRA energy of $\sqrt{s}\sim 30$ GeV could no longer be maintained, as is

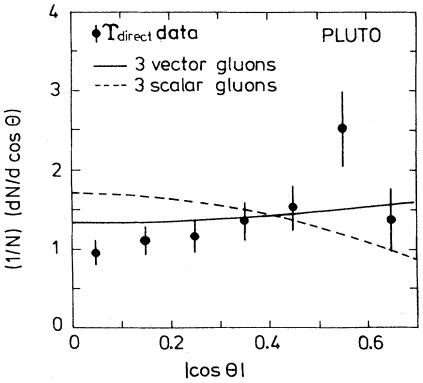

FIG. 86. Distribution of $|\cos\theta|$, corrected for detector *and* hadronization effects. θ is the angle between the thrust axis and the beam axis. The curves are predicted for Υ decay into three vector or three scalar gluons, respectively.

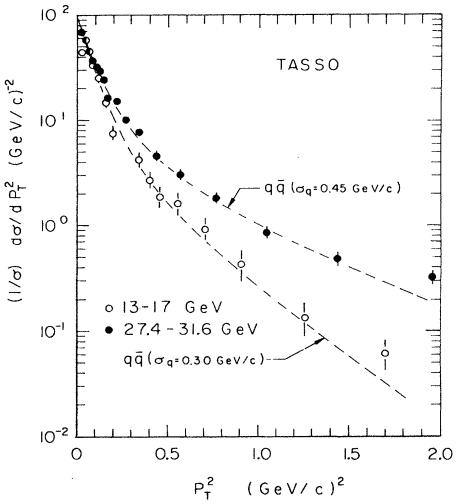

FIG. 87. The $P_T{}^2$ distribution for hadron events as $\sqrt{s}=13-17$ GeV and $\sqrt{s}=27.4-31.6$ GeV. The dashed lines are predictions for the quark-antiquark model with the average $P_T(\sigma_q)$ for the quarks 0.30 GeV/c and $\sigma_q=0.45$ GeV/c.

demonstrated in the $p_T{}^2$ distribution of the TASSO group in Fig. 87. The low-energy data $\sqrt{s}=17$ GeV can be described by the two-jet model with an average p_T of the produced hadrons with respect to the jet axis of ~ 300 MeV. The 30-GeV data, however, cannot be described in this way and the $\langle p_T \rangle$ has to be raised to ~ 450 MeV to get agreement with the measured distribution. To study the structure of the events, each event can be divided into two hemispheres using the plane perpendicular to the thrust axis. Each hemisphere can then be separately analyzed, as if it were a single jet. The jet having the smaller p_T with respect to the thrust axis is defined as the "narrow" or "slim" jet and the other as a "broad" or "fat" jet. Figure 88 shows the data from the PLUTO group for the $\langle p_T{}^2 \rangle$ of a slim and fat jet as a function of $x=p_i/p_{\text{beam}}$ for the low- and high-energy data. For both energies the slim jet can be described by

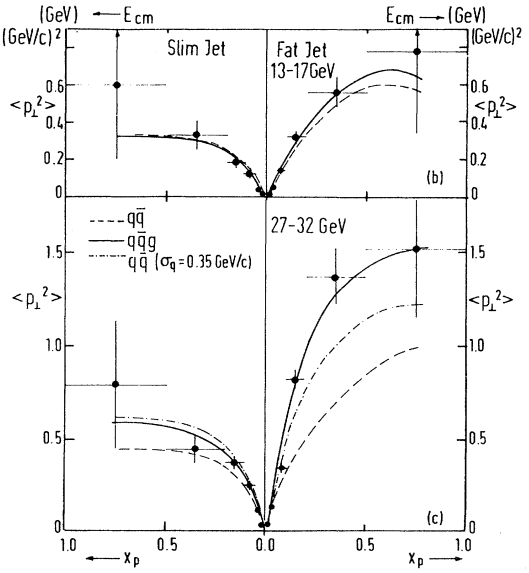

FIG. 88. The average $P_T{}^2$ plotted as a function of the normalized momentum x for the hadrons at low c.m. energy ($\sqrt{s}=13-17$ GeV) and at high energy ($\sqrt{s}=27-32$ GeV) as obtained by the PLUTO group. Ths solid curves are the QCD predictions. The dashed and dashed-dotted curves are $q\bar{q}$ model calculations with different σ_q for the quarks.

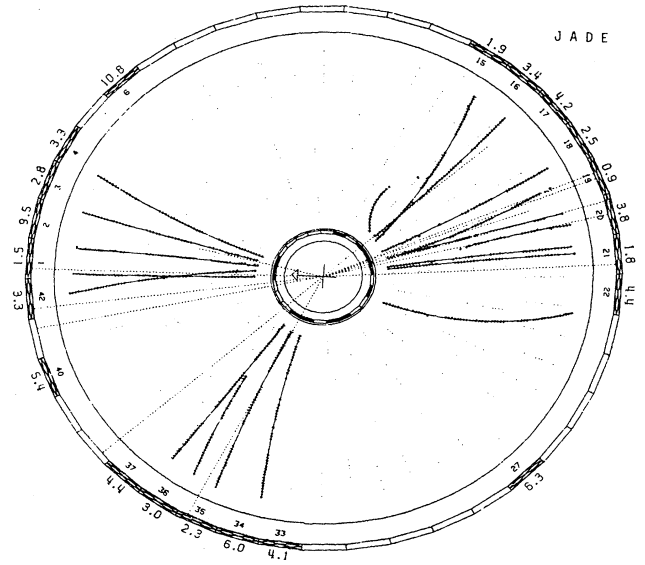

FIG. 89. A flat hadronic event in the JADE detector. The solid lines indicate the trajectories of the charged tracks. The dotted lines from the intersection point are the detected neutral particle directions.

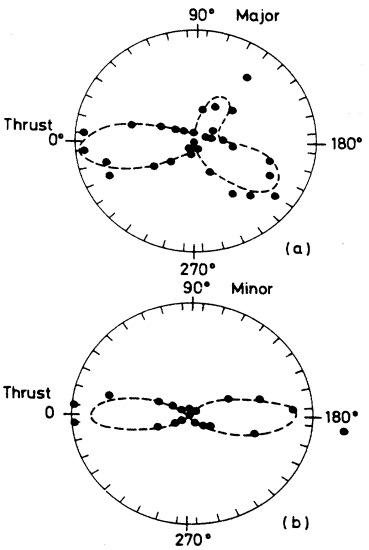

FIG. 90. (a) Energy distribution in the event plane for the events of the MARK-J group with $T \leq 0.8$ and $O_B \geq 0.1$ at $\sqrt{s}=27.4$, 30, and 31.6 GeV. The radial distance of the data points is proportional to the energy deposited in a 10° bin. The superimposed dashed line represents the distribution predicted by QCD. (b) Measured and predicted energy distribution in the plane perpendicular to the event plane.

a normal quark jet; the fat jet, however, is too broad and can be described either by an increase in $\langle p_T \rangle$ on the fat side alone or by QCD.

It was also noted that the above-mentioned effects were due to an excess of so-called planar or oblate events and that some of these showed a three-jet structure. An example of such an event is given in Fig. 89, which shows an event from the JADE group projected onto the event plane.

Statistically significant results, establishing the three-jet pattern from $q\bar{q}g$ of a sample of hadronic events, are shown in Fig. 90 of the MARK-J group, in which a sample of the events with low thrust and high oblateness, where the gluon emission effect is expected to be relatively large, is selected for detailed examination. The key feature of this figure is that it consists of the superposition of an entire event sample, and thus displays the average behavior of the energy flow for planar events at high energy. The event sample is composed of 40 events with $T<0.8$ and $O_b>0.1$ out of 446 hadronic events.

The calculated Monte Carlo predictions based on QCD in both the rate and shape of three-jet events in the figure were compatible with the data with $\chi^2=67$ for 70 degrees of freedom. The accumulated energy distribution in the lower part of the figure, showing the view in the plane perpendicular to the event plane, exhibits a flat distribution consistent with the model predictions.

These results can be contrasted to those obtained with a simple phase-space model. Using a χ^2 fit of the phase-space energy distribution to the data, one found that $\chi^2=222$ for 70 degrees of freedom. Therefore, phase space is inconsistent with the data. From the oblateness or flatness distribution it could be established that the $q\bar{q}$ contribution to these events is negligible.

B. QCD tests with the MARK-J detector

1. Energy flow method

In this section the detailed topological analysis is reviewed which was used by the MARK-J to test QCD and to isolate the three-jet events arising from the emission of hard noncollinear gluons (Barber *et al.*, 1979d, g; Newman, 1980).

In order to exclude events where leading particles have escaped down the beam pipe, or where part of a broad jet is missed, only those events are selected for which the visible energy $E_{\rm vis}$ is greater than or equal to $0.7\sqrt{s}$. This cut also eliminates two-photon events and events where a hard photon is emitted in the initial state. The drift tubes surrounding the beam pipe enable this group to separate more distinctly the distribution of charged particles from neutrals. Since neutral particles carry away a large portion of the total energy, they will affect not only the axes of the jets, but also the identification of individual jets. The characteristic features of hard noncollinear gluon emission in $e^+e^-\to q\bar{q}g$ are illustrated in Fig. 91. Because of momentum conservation the momenta of the three particles have to be coplanar. For events where the gluon is sufficiently energetic and at large angles with respect to both the quark and antiquark, the observed hadron jets also tend to be in a recognizable plane. This is shown in the upper part of the figure, where a view down onto the event plane shows three distinct jets—distinct because the fragmentation products of the quark and gluons have limited P_t with respect to the original directions of the partons. The lower part of the figure shows a view looking toward the edge of the event plane, which results in an apparent two-jet structure. Figure 91 thus demonstrates that hard noncollinear gluon emission is characterized by planar events which may be used to reveal a three-jet structure once the event plane is determined.

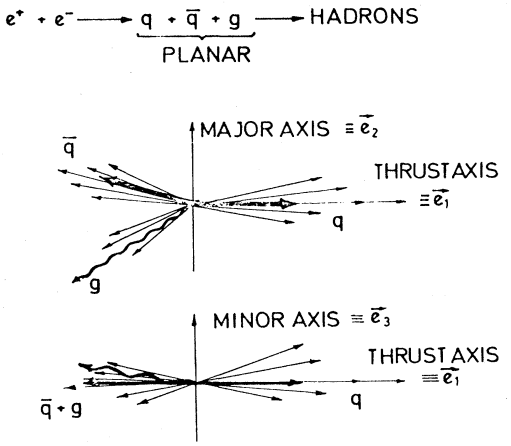

FIG. 91. A schematic view of the process $e^+e^-\to q\bar{q}g$ and the three resulting hadron jets, showing the axes used to describe the event.

The spatial energy distribution is described in terms of three orthogonal axes called thrust, major, and minor axes. The axes and the projected energy flow along each axis $T_{\rm thrust}$, $F_{\rm major}$, and $F_{\rm minor}$ are determined as follows:

(1) The thrust axis $\mathbf{e}_1$ is defined as the direction along which the projected energy flow is maximized. The thrust $T_{\rm thrust}$ and $\mathbf{e}_1$ are given by

$$T_{\rm thrust}=\max\frac{\Sigma_i\,|\,\mathbf{E}^i\cdot\mathbf{e}_1\,|}{\Sigma_i\,|\,\mathbf{E}^i\,|}\ ,$$

where $\mathbf{E}^i$ is the energy flow detected by a counter as described above and $\Sigma_i\,|\,\mathbf{E}^i\,|$ is the total visible energy of the event ($E_{\rm vis}$).

(2) To investigate the energy distribution in the plane perpendicular to the thrust axis, a second direction $\mathbf{e}_2$ is defined perpendicular to $\mathbf{e}_1$. It is the direction along which the projected energy flow in that plane is maximized. The quantity $F_{\rm major}$ and $\mathbf{e}_2$ are given by

$$F_{\rm major}=\max\frac{\Sigma_i\,|\,\mathbf{E}^i\cdot\mathbf{e}_2\,|}{E_{\rm vis}},\quad \mathbf{e}_2\perp\mathbf{e}_1\ .$$

(3) The third axis $\mathbf{e}_3$ is orthogonal to both the thrust and the major axes. It is found that the absolute sum of the projected energy flow along this direction, called

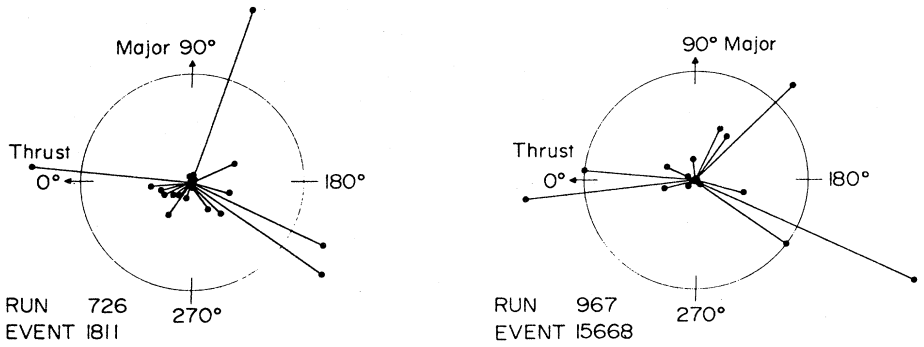

FIG. 92. Energy flow diagrams for two high-energy hadronic events viewed in the major-thrust plane.

F_{minor}, is very close to the minimum of the projected energy flow along any axis, i.e.,

$$F_{\text{minor}}=\frac{\Sigma_i\,|\,\mathbf{E}^i\cdot\mathbf{e}_3\,|}{E_{\text{vis}}}\approx\min\frac{\Sigma_i\,|\,\mathbf{E}^i\cdot\mathbf{e}\,|}{E_{\text{vis}}}\ .$$

If hadrons were produced according to phase space or a $q\bar{q}$ two-jet distribution, then the energy distribution in the plane as defined by the major and minor axes would be isotropic, and the difference between F_{major} and F_{minor} would be small. Alternatively, if hadrons were produced via three-body intermediate states such as $q\bar{q}g$, and if each of the three bodies fragmented into a jet of particles with $\langle P_t\rangle\sim 325$ MeV, the energy distribution of these events would be oblate (P_t refers to the quarks). Following the suggestion of H. Georgi, the quantity oblateness O is defined as

$$O=F_{\text{major}}-F_{\text{minor}}\ .$$

The oblateness is $\sim 2\ P_{t\text{gluon}}/\sqrt{s}$ for three-jet final states and is approximately zero for final states coming from a two-jet distribution.

As mentioned in Sec. VII.A for the study of the detailed structure of the events each event is divided into two hemispheres using the plane defined by the major and minor axes, and the energy distribution in each hemisphere is separately analyzed as if it were a single jet. The jet having the smaller P_t with respect to the thrust axis is defined as the narrow jet (n) and the other as the broad jet (b). In each hemisphere we calculate the oblateness, $O_n=2(F^n_{\text{major}}-F^n_{\text{minor}})$ and $O_b=2(F^b_{\text{major}}-F^b_{\text{minor}})$, and thrusts T_n and T_b.

One approach to analyzing the flat events for a possible three-jet structure is illustrated by Fig. 92. The fig-

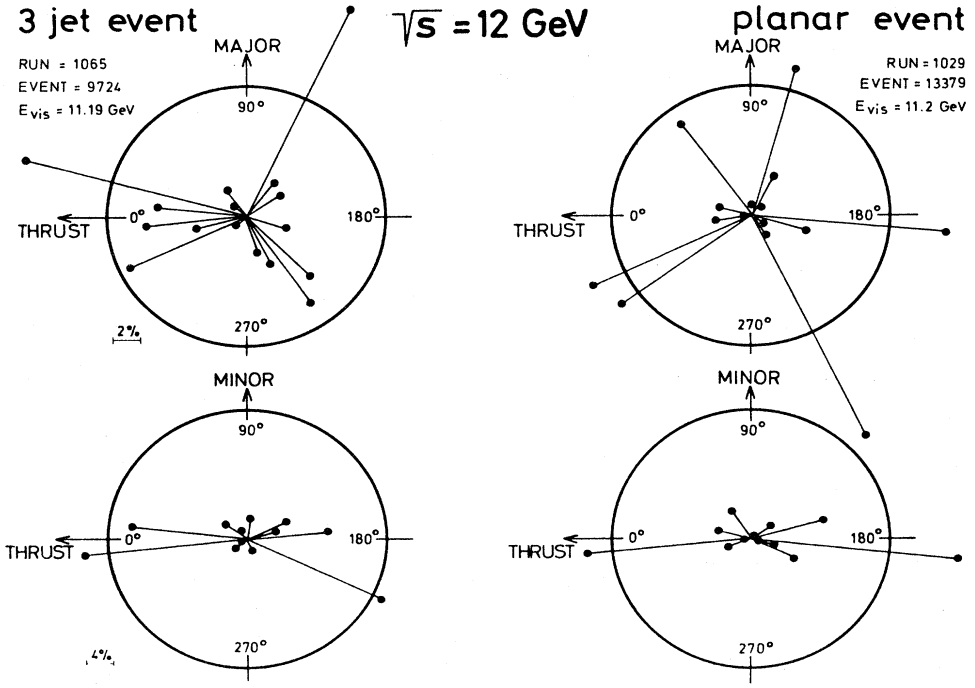

FIG. 93. Energy flow diagram. Two events measured at $\sqrt{s}=12$ GeV with the lines showing the direction and magnitude of energy deposited in the calorimeter displayed in two projections. The events appear to have a multijet structure in the thrust-major plane. The view in the thrust-minor plane shows the events are flat.

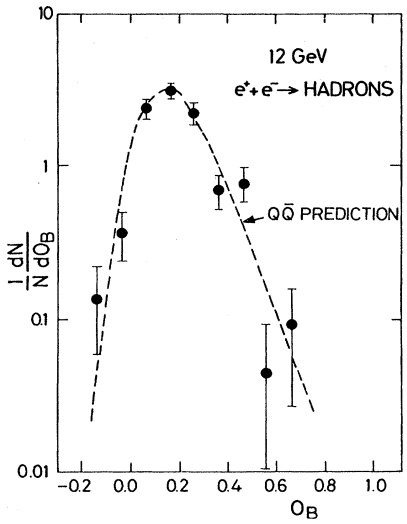

FIG. 94. The broad-jet oblateness distribution $1/N \cdot dN/dO_b$ for all hadron events at $\sqrt{s}=12$ GeV. The dotted curve is the prediction of the two-quark-antiquark model, with $\langle P_t \rangle = 350$ MeV.

ure shows the energy flow diagram for each of two high-energy hadronic events, viewed in the event plane determined by the major and thrust axes. The energy flow diagram is a polar coordinate plot in which the energy vectors $\mathbf{E}^i$ are summed in 10° intervals. Each point in the plot represents the summed energy in an angular interval, with the radius given by the magnitude, and the azimuth given by the center of the angular interval in the event plane. The two events in the figure both show an apparent three-jet structure.

However, the examination of individual event appearances cannot be used to establish the underlying three-jet structure characteristic of $q\bar{q}g$ final states. This is demonstrated by Fig. 93, which shows two low-thrust, planar events at 12-GeV center-of-mass energy. The events also show a distinct multijet structure. It should be noted that all the measured distributions at low energies (thrust, oblateness, etc.) are well described by a simple $q\bar{q}$ model (see Fig. 94), so that the suggestive event appearances are unrelated to gluon emission, but are dominated by fluctuations in the quark fragmentation process. The views of the events in the minor-thrust plane (looking at the edge of the event plane in Fig. 93) also show that the events are planar.

In the analysis discussed below, the Monte Carlo model of Ali *et al.* (Ali *et al.*, 1980b) was adopted. As discussed in Sec. III.C this model incorporates higher-order QCD effects, the q^2 evolution of the quark and gluon fragmentation functions, and the weak decays of heavy quarks.

Figures 95(a) and 95(b) show the event distribution as a function of O_n and O_b, compared to the predictions of the QCD model and of two quark-parton models with quark $\langle P_t \rangle = 300$ and 500 MeV, respectively. Figure 95(a) shows that the narrow jet distribution agrees with the various models, indicating that it comes from a single quark jet. Figure 95(b), however, shows that the quark-parton models severely underestimate the number of events with $O_b \geq 0.3$, while the QCD model correctly predicts the observed distribution.

The T_n and T_b thrust distributions of the flat events in the region $O_b \geq 0.3$ are shown in Figs. 95(c) and 95(d), along with the QCD and high-P_t $q\bar{q}$ models. The observed distribution is also compared to the "flattened" $q\bar{q}$ model, in which the quarks have $\langle P_t \rangle = 500$ MeV in the thrust-major plane and $\langle P_t \rangle = 300$ MeV in the thrust-minor plane. The T_n distribution in Fig. 95(c) is in good agreement with the QCD model predictions and has the same general shape as the thrust distribution for high-energy $e^+e^- \to q\bar{q}$ reactions shown in Figs. 62 and 63. As expected, the T_b distribution, however, is much broader than that of T_n and agrees only with the QCD predictions.

The distributions in Figs. 95(c) and 95(d) demonstrate that the relative yield of flat events, and the shape of these events as measured by T_n and T_b can be explained only by the QCD model. The distributions T_n and T_b further exclude phase space (which peaks at lower thrust values), as well as $q\bar{q}$ models, as possible explanations of the energy flow plots.

The development of the three-jet structure with decreasing thrust and increasing oblateness, as predicted by QCD (DeRujula *et al.*, 1978), is shown in a series of energy flow diagrams in Fig. 96(a)—(c).

As seen in Fig. 96(a) the events at high-thrust values are dominated by a two-jet structure characteristic of $e^+e^- \to q\bar{q}$. In Fig. 96(b), where the thrust is lower, we begin to see the appearance of the gluon jet; and in Fig. 96(c) the three-jet events are predominant. It is important to note that in all three cases the data agree with the QCD model prediction, showing the increased incidence of hard noncollinear gluon emission with decreasing thrust and increasing oblateness. The energy flow in the minor-thrust plane contains only two nearly identical lobes similar to the narrow jet in Fig. 96(a), in good agreement with QCD predictions. In Fig. 97 we unfold the energy flow diagram of Fig. 96(c) to see more clearly the comparison of the data with the predictions of QCD, $q\bar{q}(\langle P_t \rangle = 500$ MeV), and a "mixed model" consisting of a combination of $q\bar{q}$ and phase-space contributions. All models in Fig. 97 are normalized to have the same areas (as the data) before the individual cuts are imposed. The normalization for the mixed model was determined by adjusting the $q\bar{q}(\langle P_t \rangle = 300$ MeV) and phase-space contributions to agree with the measured thrust distribution. As seen in Fig. 97, only QCD can describe the observed three-jet structure.

Including the highest PETRA data, the same picture emerges as the one described above. The event sample consists of 3600 hadronic events over the range $12 \leq \sqrt{s} \leq 36.6$ GeV.

Figure 98 shows the event distribution as a function of the broad jet oblateness O_b, compared to the predictions of the QCD model and of a quark-parton $q\bar{q}$ model without gluon emission. The data agree with the QCD

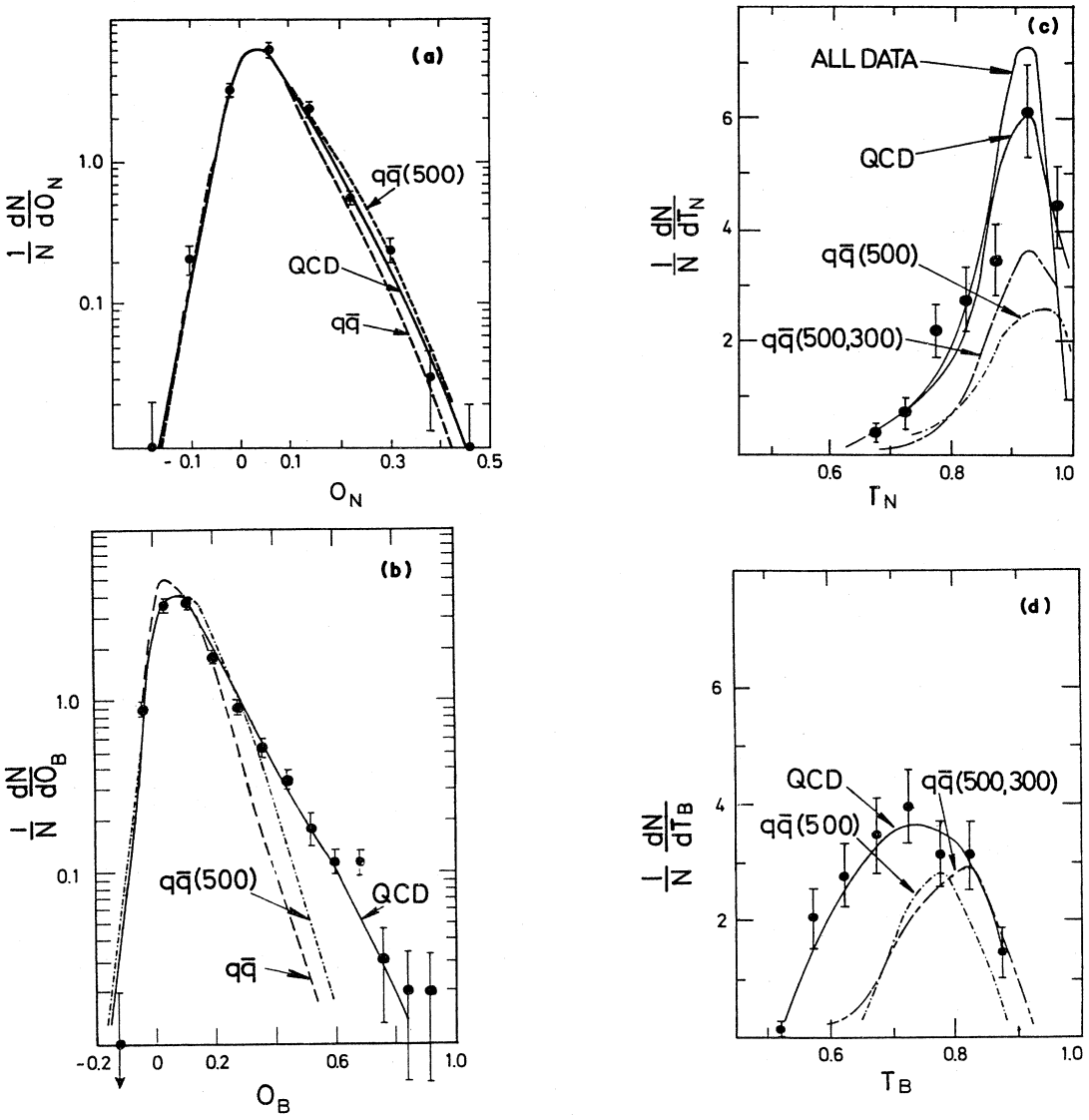

FIG. 95. (a) The narrow-jet oblateness distribution $1/N \cdot dN/dO_N$ for all hadron events with measured energy $E_{\text{vis}} \geq 07.\sqrt{s}$. The data are compared to the predictions of the QCD model and to two quark-antiquark models with $\langle P_t \rangle = 300$ and 500 MeV, respectively. (b) The broad-jet oblateness distribution $1/N \cdot dN/dO_b$ under the same condition as (a). (c) The thrust distribution of the narrow jets for events with $O_b \geq 0.3$. Also shown are the various model predictions including the flattened $q\bar{q}$ (500, 300) discussed in the text. Note that the narrow-jet thrust distribution is consistent with the thrust distribution of all the hadron events labeled "ALL DATA." (d) The thrust distribution of the broad jets for events with $O_b \geq 0.3$. The curves are discussed in the text.

predictions, but the $q\bar{q}$ model severely underestimates the rate of production of flat events, particularly for $O_b \geq 0.3$. The small contribution of $q\bar{q}$ above $O_b \geq 0.3$ consists mainly of events containing a photon radiated at large angles from the initial state.

In Fig. 99(a) the energy flow pattern of the planar event samples with $O_b \geq 0.3$ in the high-energy ($\sqrt{s} \geq 27.4$ GeV) and the low-energy ($\sqrt{s} \leq 22$ GeV) regions is compared to the predictions of QCD and to the predictions for the simple production of hadrons according to phase space. The pattern shown by the high-energy data agrees with the QCD predictions but is quite distinct from the pattern given by phase space. The low-energy data, on the other hand, gives a pattern much closer to phase space, as the presence of the jets at lower energy indicates.

To study the properties of the individual jets, the event plane is divided into three subregions bounded by the angles corresponding to the minima in the energy flow diagram. The thrust distributions of the individual jets shown in Fig. 99(a) are in excellent agreement with the QCD predictions, corresponding to the appearance of well-collimated jets. The phase-space model predicts distributions which are much broader in all three regions.

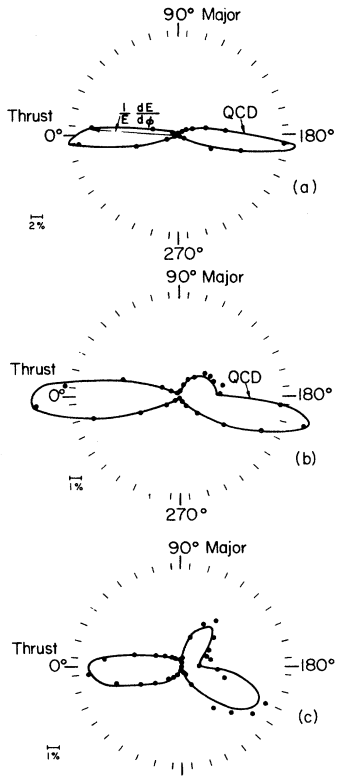

FIG. 96. (a) Energy flow diagram in the thrust-major plane for high-energy data (27−31.6 GeV) with $T \geq 0.9$. The solid line is the prediction of QCD. (b) The same as (a) for events with $0.8 \leq T \leq 0.9$ and broad-jet oblateness $O_b \geq 0.1$. (c) Same as (a) for events wth $T < 0.8$ and $O_b \geq 0.1$.

In Fig. 99(b) we unfold the energy flow diagram of Fig. 99(a) to see more clearly the comparison between the high-energy planar events and the predictions of the QCD, $q\bar{q}$, and phase-space models. All models in the figure are normalized to have equal area. Figure 99(b) demonstrates that at high energy only QCD can explain the shape of the energy flow pattern of planar events.

Figure 99(c) shows the two-dimensional distribution $d^2\sigma/d\theta_{12}d\theta_{23}$ for the planar events at high energy, where θ_{12} is the angle between the first and second jet, and θ_{23} is the angle between the second and third jets. The three jets in this analysis are ordered according to the energy

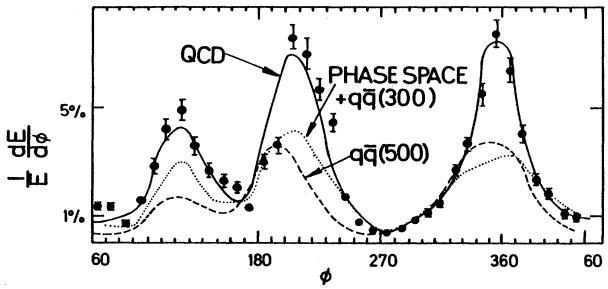

FIG. 97. The unfolded energy flow diagram of Fig. 96(c) as compared to QCD, the quark model ($\langle P_t \rangle = 500$ MeV), and a mixed $q\bar{q}$ and phase-space model (see text).

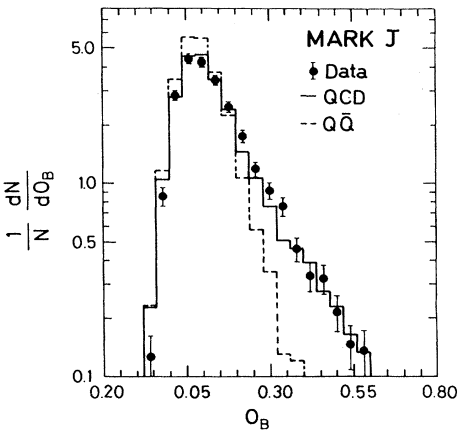

FIG. 98. The broad-jet oblateness distribution $1/N \cdot dN/dO_B$. The data are compared to the predictions of the QCD and $q\bar{q}$ models.

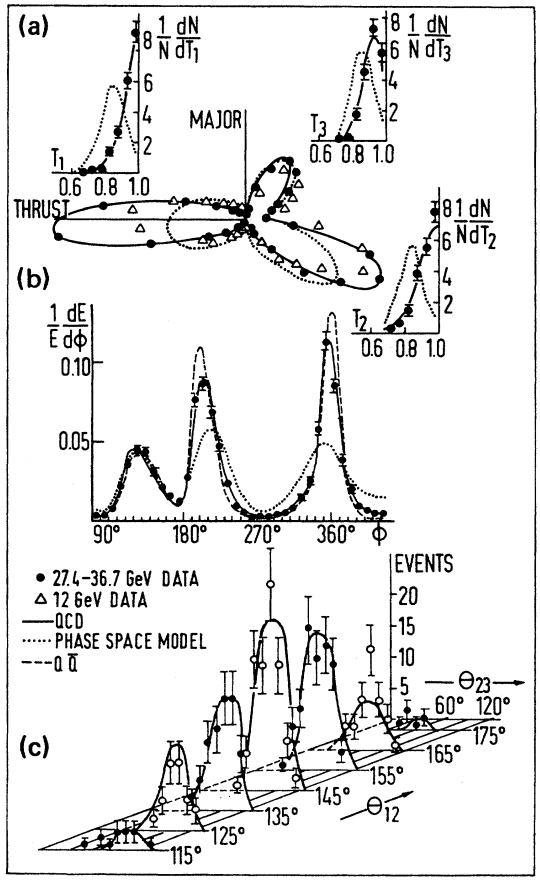

FIG. 99. (a) Energy flow diagram in the thrust-major plane for events with $O_B \geq 0.3$, for the high-energy data ($\sqrt{s} = 27.4-36.6$ GeV) and the low-energy data ($\sqrt{s} = 12-22$ GeV), compared to the predictions of QCD at high energy and of the phase-space model. The thrust distribution $1/N \cdot dN/dT$ for each individual jet is shown beside the corresponding jet in the energy flow diagram. (b) The unfolded energy flow diagram of Fig. 99(a) compared with the QCD and $q\bar{q}$ models. (c) The two-dimensional distribution in the opening angles between the jets θ_{12} and θ_{23}, compared with QCD predictions.

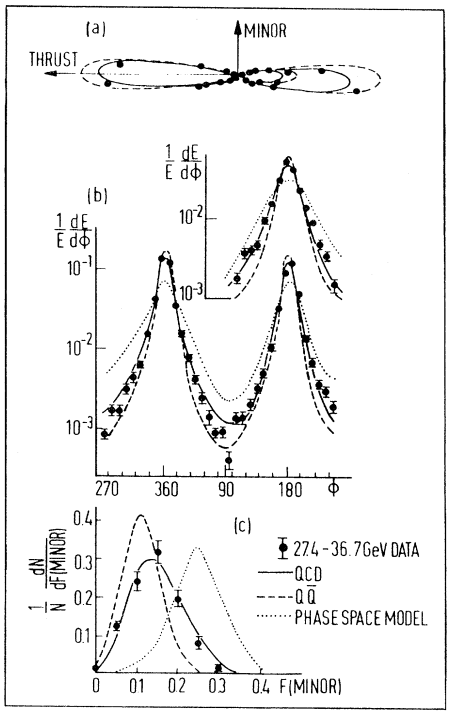

FIG. 100. (a) The energy flow diagram in the thrust-minor plane for the high-energy events (27.4—36.6 GeV) with $O_B \geq 0.3$, compared with the predictions of the QCD, $q\bar{q}$, and phase-space models. (b) The unfolded energy flow diagram of Fig. 100(a). Here the third jet is shown above the second jet at $\sim 180°$. (c) The minor distribution $1/N \cdot dN/dF_{\text{minor}}$, where F_{minor} is defined for the entire event (see text).

projected along the major axis. The data are compared to the expectations of the QCD model, absolutely normalized. This figure demonstrates that the three-jet kinematics seen in the data (which would be completely determined by θ_{12} and θ_{23} if the jets originated from massless constituents) agrees well with QCD predictions over the full range of θ_{12} and θ_{23}. The planar events in this sample show three well-defined jets with $\langle \theta_{23} \rangle \approx 70°$ and $\langle \theta_{12} \rangle \approx 145°$. From Fig. 99(a) we find more than 90% of the energy of each jet to be within $\pm 20°$. Therefore all the jets are well separated.

The structure of three-jet events viewed on edge to the event plane is shown in Fig. 100. The energy flow pattern of events with $O_b \geq 0.3$ viewed in the thrust-minor plane is given in Fig. 100(a) compared to the QCD and $q\bar{q}$ predictions. The individual jets, two of which overlap in this view, are shown separately. As seen in the figure, all three jets have approximately the same thickness, indicating that the P_t distributions relative to the axis of each jet are similar. This is seen more clearly in Fig. 100(b) where the energy flow diagram of Fig. 100(a) is unfolded, and where the data are compared to the three forementioned models. Figure 100(b) demonstrates that the individual jets are thinner than the expectations of the phase-space model, but thicker than the $q\bar{q}$ model would predict. The data agree well in all cases with the QCD predictions.

In Fig. 100(c) the distribution of the fraction of the visible energy projected along the minor axis for the entire event (defined as F_{minor}) is compared to the model predictions. Figure 100(c) shows that if the source of low-thrust oblate events were simply phase-space production of hadrons, then the events would be thicker. The figure also shows that if the underlying process were $q\bar{q}$ production, then the events would be even flatter than what is actually observed. In this case the main contribution would be the result of hard noncollinear photon emission (see Fig. 99b), where the photon contribution to F_{minor} is ~ 0. Therefore $q\bar{q}$ can at most be a small fraction of the three-jet sample. The QCD model once again provides an excellent description.

Thus the MARK-J group used an analysis of energy flow to show that the planar hadronic events produced at high energies consists of three-jet events where the individual jets are strongly collimated around the jet axes and are separated by large angles. These general topological features are not model dependent. The rate of production and the detailed shape of the events agree with the predictions of QCD.

2. Determination of the strong coupling constant α_s

Recent experiments on scaling violations in lepton inelastic scattering (Anderson *et al.*, 1978; Bosetti *et al.*, 1978; De Groot *et al.*, 1979a, b, c) on high-P_t events in dilepton production by hadrons and multijet events in e^+e^- annihilations all indicate that the results are explained naturally in the QCD theory of the strong interactions of quarks and gluons (Gross and Wilczek, 1973; Politzer, 1973; Ellis *et al.*, 1976; De Grand *et al.*, 1977; Kramer *et al.*, 1978; De Rujula *et al.*, 1978; Hoyer *et al.*, 1979; Ali, Körner *et al.*, 1979; Ali *et al.*, 1979). The strong coupling constant $\alpha_s(q^2)$ between quarks and gluons has been measured indirectly in quarkonium bound states (Krammer and Krasemann, 1978) and in deep-inelastic experiments. At PETRA, where the q^2 is much larger, computations are expected to be more reliable. In addition, high-energy e^+e^- annihilations offer a more direct way of measuring α_s and testing perturbative QCD, because they are expected to give rise to multijets which can be systematically identified.

The three-jet events discussed in the previous section, which consist of $q\bar{q}g$ fragmentation products with relatively small backgrounds from fluctuations of phase-space-like processes or quark-antiquark intermediate states, allow one to make further comparisons of the event properties with the predictions of QCD. In particular, the relative yield of three-jet events and the shape distribution give a way to measure α_s directly.

Several methods were used by the MARK-J group in determining the strong coupling constant α_s, including (1) the average oblateness $\langle O_b \rangle$, (2) the fraction of events with $O_b \geq 0.3$, and (3) the relative yield of events with $O_b - O_n \geq 0.3$, where O_n is constrained to be greater than zero.

For each quantity, α_s was allowed to vary in the QCD

model, and then the range of α_s values for which the QCD model predictions agree with the data within errors was determined. In particular, the samples obtained using criteria (2) and (3) consist predominantly of three-jet events from $e^+e^-\to q\bar{q}g$, in which the gluon emitted is both very energetic and at a large angle with respect to both the quark and the antiquark. This leads to an event sample where the number of events in the sample is a quasilinear function of α_s, and in which the influence of nonperturbative effects not calculable in QCD is minimal. For criterion (2), for example, a value of $\alpha_s=0.19\pm0.02$ was obtained matching the QCD model. The predominance of $q\bar{q}g$ in a sample with $O_b\geq0.3$ is maintained even if $\langle P_t\rangle$ is allowed to vary from 200 to 400 MeV in the model.

The methods described above yield a self-consistent set of α_s values, as illustrated in Fig. 101. On the basis of the results of the three methods they obtained

$$\alpha_s=0.19\pm0.02 \text{ (statistical error)}$$
$$\pm0.04 \text{ (systematic error)}.$$

The large systematic error was mostly due to uncertainties in QCD calculations (Ali *et al.*, 1980a). For method (2) the range of α_s due to variation in $\langle P_t\rangle$ from 200 to 400 MeV is ±0.01, and the change in α_s due to different cuts in O_b from $O_b\geq0.3$ to $O_b\geq0.2$ or cuts in O_n from no cuts to $|O_n|\leq0.1$, is -0.01. For method (2), changing the fragmentation function $zD(z)$ to $1-z$ for u, d, and s quarks and $zD(z)$ to z for c and b quarks does not change the α_s value noticeably.

3. Triplicity analysis

The triplicity method has been used by the PLUTO collaboration (Berger *et al.*, 1978b), analyzing the hadron events from the decay of the Υ, as already mentioned in Sec. VII.A. This method has been especially derived for the treatment of three-jet events and has been adapted to the particular MARK-J requirements. The energy flow is split for each event into three continuous nonoverlapping subregions, adding up to 4π. In each subregion a unit vector $\mathbf{n}_i$ $(i=1,3)$ is constructed in the direction of the energy flow vector sum $\Sigma\mathbf{e}_i$, giving the jet direction. The split into regions is then varied until the three-jet analog to thrust, the triplicity T_3, is maximized,

$$T_3=(t_1+t_2+t_3)/E_{\text{vis}},$$

where t_j is the thrust in subregion j, $t_j=\Sigma_k\mathbf{e}_k\cdot\mathbf{n}_j$.

After this procedure, the total energies and directions of the three jets $\mathbf{E}_i$ and $\mathbf{n}_i$ $(i=1,3)$ are submitted to a kinematical fit balancing the four momenta such that energy momentum conservation is respected under the assumption that all jets are massless. Monte Carlo studies show that the jet momenta reconstructed by this method reproduce the momenta of partons with good accuracy when fragmentation is described by the Feynman and Field model. In the following analysis the jets will be ordered according to their energy, jet 1 being the most energetic and jet 3 the least energetic one.

For events in which the jets are well separated from each other, the energy flow inside jets can be studied. This condition is fulfilled for jet 1 in all events at energies above 12 GeV, while jets 2 and 3 can be reliably separated only in clear three-jet events ($O_B\geq0.3$) at high energies ($\sqrt{s}\geq27$ GeV; see below).

Figure 102 shows the longitudinal energy flow $1/E_j(dE_j/d\cos\epsilon)$ for jets 1 and 3 at $\sqrt{s}\approx30$ and 35 GeV, where ϵ denotes the angle with respect to the corresponding jet axis $\mathbf{n}_j$. At these high energies even the least-energetic third jets ($\langle E_3\rangle=6.4$ and 7.1 GeV, respectively) show an exponentially falling distribution

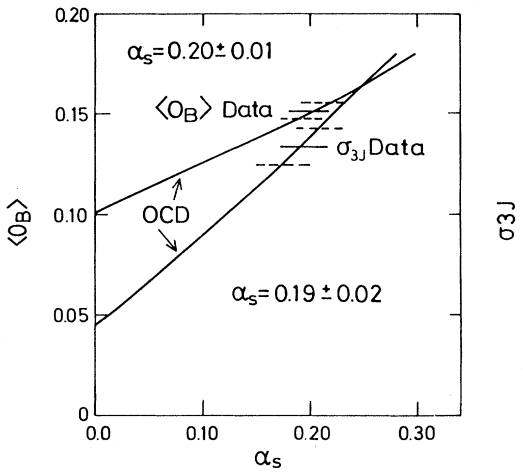

FIG. 101. The left-hand graph: the averaged value of oblateness $\langle O_b\rangle$ for all events with $E_{\text{vis}}\geq0.7\sqrt{s}$ as a function of α_s in the QCD model. The right-hand graph: the fraction of hadronic events $O_b\geq0.3(\sigma_{3j})$ as a function of α_s computed by varying α_s in the QCD model.

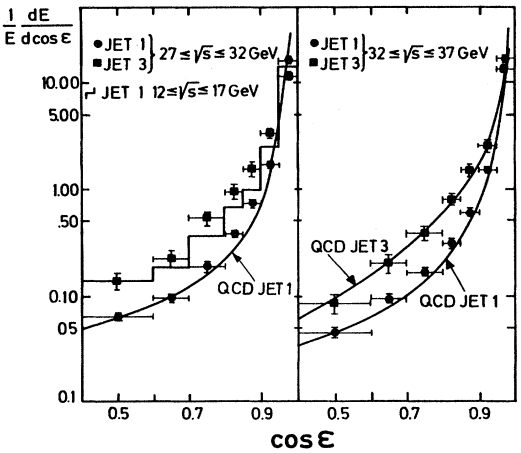

FIG. 102. (a) The quantity $1/E\cdot dE/d\cos\epsilon$ is plotted vs $\cos\epsilon$ for jets 1 and 3. ϵ is the angle between the measured energy flow element and the jet axis. The lowest-energy jet from the 30-GeV data is compared to the highest-energy jet from the 12-GeV data (histogram). The solid line is the QCD prediction. (b) The highest- and lowest-energy jets from the $\approx$35-GeV data sample, compared to QCD (solid lines).

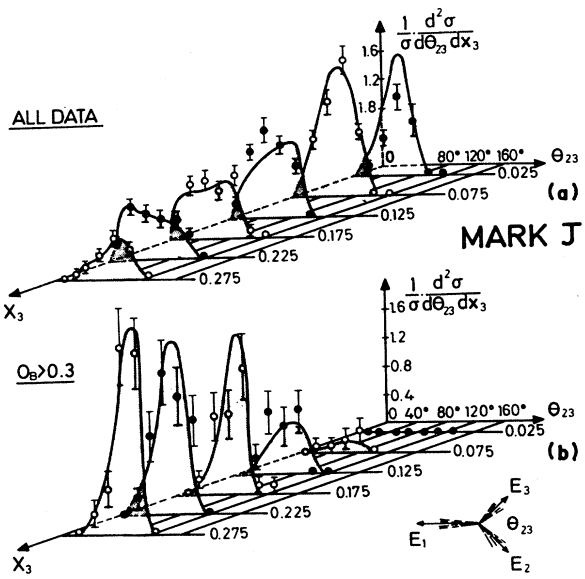

FIG. 103. The observed double differential cross section for three jets after kinematic fitting is plotted for (a) all events and (b) for events with broad-jet oblateness greater than 0.3. The two variables are θ_{23}, the angle between the second and third jet, and x_3, the normalized momentum of the third jet. The data (solid points) agree with the predictions of QCD (solid curves).

indicating their high degree of collimation around the jet axis. The longitudinal energy flow of jet 3 in the flat events at 30 GeV is compared to that of jet 1 of all the events at 12 GeV $\leq\sqrt{s}\leq$17 GeV, which has the same average energy. The two distributions agree with each other within errors, indicating that the fragmentation of gluons, forming $\sim$40% of the least-energetic jets at high energies, is not substantially different from that of quarks.

The data in Fig. 102 show that about 90% of the jet energy is contained inside a cone of half-angle $\sim$20° for a high-energy jet and $\sim$40° for a low-energy jet. For a reliable separation of jets 2 and 3 in the high-energy data it is necessary therefore that they be more than about 60° apart. This requirement is naturally met by selecting events with high oblateness in the broad hemisphere, $O_B\geq 0.3$. Figure 103 shows the double differential distribution $N^{-1}d^2N/dx_3d\theta_3$ for the whole hadron sample at high energies $27\leq\sqrt{s}\leq 37$ GeV, which is dominated by two-jet events up to an energy fraction $x_3=E_3/\sqrt{s}\leq 25\%$ contained in the third jet. Consequently, since the split-up of one jet into "jet 2" and "jet 3" is artificial, the average opening angle between these jets, $\langle\theta_{23}\rangle$ decreases with increasing energy fraction x_3, from about 65° at $x_3\approx 0$ to 55° at $x_3\approx 10\%$. In contrast to this, genuine three-jet events [$O_B\geq 0.3$, Fig. 102(b)] show an opposite behavior. While events with low x_3 or θ_{23} are cut out ($O_B\approx 2x_3\sin\theta_{13}$), the average opening angle $\langle\theta_{23}\rangle$ increases with increasing x_3, being $\sim$70° at $x_3=10\%$ and $\sim$90° at $x_3=30\%$. The three-jet events with $O_B\geq 0.3$ thus represent a sample where the two

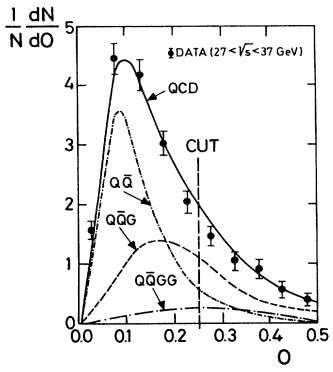

FIG. 104. The parton oblateness distribution for the hadronic events at high energy. The solid curve is the QCD prediction. The dashed and dashed-dotted curves are the parton processes as indicated.

less-energetic jets can be reliably separated and their properties studied.

Also shown in Fig. 103, as solid curves, are the double differential distributions obtained from the QCD model, in remarkable agreement with the data, especially for the three-jet sample in Fig. 103(b).

As a further consistency check, the methods of dividing up each event according to the energy flow diagram and triplicity have been compared, particularly the determination of the interjet angles θ_{12} and θ_{23} for events with $O_b\geq 0.3$; and the results are in good agreement.

The definition of broad-jet oblateness O_b is such that for events with the second and third jet well separated, $O_b\approx 2P_{t\ \mathrm{gluon}}/\sqrt{s}$, where $P_{t\ \mathrm{gluon}}$ is the gluon transverse momentum with respect to the thrust axis. In the context of the triplicity analysis, an analogous quantity

$$O\equiv 2x_3\sin\theta_{13}\approx 2P_{t\ \mathrm{gluon}}/\sqrt{s}$$

has also been used to select a clean sample of three-jet events. The distribution of O is shown in Fig. 104 for the high-energy data. The solid curve is the QCD prediction, and the dashed and dashed-dotted curves are the contributions of the different parton processes composing the solid curve. By making a cut $O\geq 0.25$, the collaboration determined the strong coupling constant α_s and as for the case in which O_B was used (Sec. VII.B.2) found a value of $\alpha_s=0.19$ with a statistical error of 0.02.

The conclusions obtained by the MARK-J collaboration from their tests of QCD can be summarized as follows:

(a) The rate and the shape of the three-jet events can be explained only by QCD and not by any of the other models they have tried.

(b) No deviations from QCD have been seen.

(c) Correlations of the energy fractions x_1, x_2, x_3, and the angles between the jets are in agreement with QCD.

(d) The strong coupling constant is determined to be $\alpha_s=0.19\pm 0.02$ (statistical), ± 0.04 (systematic).

(e) Parton energies and directions can be reconstructed using a triplicity method and a kinematic fitting procedure.

C. Tests of QCD by the PLUTO collaboration

The PLUTO collaboration (Berger *et al.*, 1980f, 1981b, 1981d) has analyzed their hadronic events obtained at DORIS and PETRA in the c.m. energy range $9.4 \leq \sqrt{s} \leq 31.05$ GeV with three different methods (Hepp, 1980). QCD predictions for hard-gluon emission and soft-gluon-quark cascades, the so-called QCD leading logarithm approximation (Konishi *et al.*, 1979), denoted in the following paragraphs as QCD LLA, are tested, and values for the strong coupling constant α_s are derived using various methods. I shall focus on two of these methods, transverse momenta in jets and a cluster analysis of the hadron events.

1. Transverse jet momentum

The aim of this analysis (Berger *et al.*, 1981d) is to find a quantity which is less sensitive to the hadronization effects of the produced quarks than the single-particle transverse momentum. The group has chosen the summed transverse momentum $K_\perp$ for the jets as the quantity to study the effect of hard-gluon bremsstrahlung. For every hadron event the thrust axis is determined using the neutral and charged particles. The transverse jet momentum is defined as

$$K_\perp = \Sigma_i \, | P_{\perp i} | \ , \tag{24}$$

where $P_{\perp i}$ is the transverse momentum of a particle with respect to the thrust axis. The summation in (24) includes only particles on one side of an arbitrary plane through the thrust axis. This plane is varied randomly, and the quantity $K_\perp$ is determined for every position of the plane. The final value for $K_\perp$ is the average $K_\perp$ obtained from the various random plane positions in order to reduce fluctuations.

The $K_\perp$ distributions at $\sqrt{s} = 9.4$, 12.0, and 17.0 GeV are shown in Fig. 105. The data are well described by the QCD LLA calculations (Curci *et al*, 1979a,b), a model which is essentially a $q\bar{q}$ model, with the addition

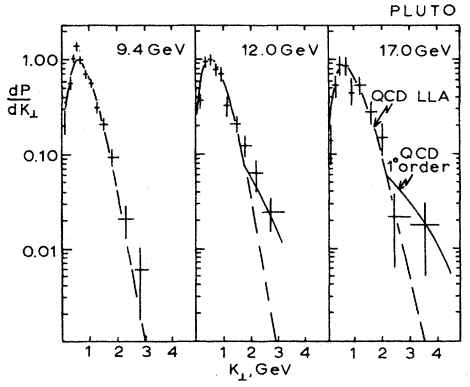

FIG. 105. The distribution $1/N \cdot dN/dK_\perp$ ($dP/dK_\perp$) at the c.m. energies, $\sqrt{s} = 9.4$, 12.0, and 17.0 GeV. The dashed curves are the predictions from the QCD LLA calculations. The curves are the predictions of the QCD LLA plus the first-order QCD corrections.

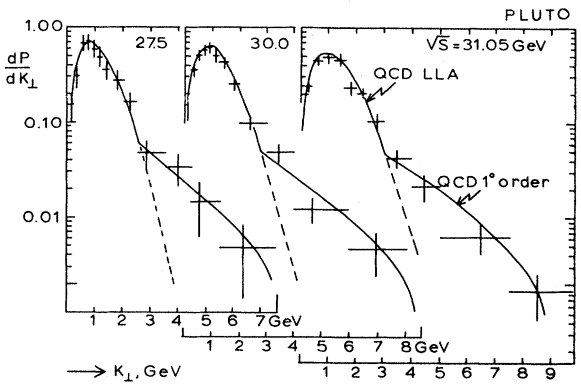

FIG. 106. The $dP/dK_\perp$ distributions at the c.m. energies $\sqrt{s} = 27.5$, 30.0, and 31.05 GeV. The curves are as in Fig. 105.

of the emission of low-energetic gluons. The average P_t in this model is able to rise slowly with increasing c.m. energy in contrast with the naive quark model. At higher energy, $\sqrt{s} = 17$ GeV, there is some evidence that hard-gluon emission is necessary to account for the high-$K_\perp$ part of the spectrum.

The $K_\perp$ distributions of the high-energy data are shown in Fig. 106. Above 2.5 GeV in $K_\perp$ the tail has become very pronounced, and this part of the distribution can be described only by first-order QCD, that is, hard-gluon bremsstrahlung. By comparing the low-energy part, which is very well described by QCD LLA, with the high-energy part of the distributions, one can determine the rate of the events where hard-gluon effects occur. The fraction of those events can be related directly to the value of the strong coupling constant α_s. This method enables the PLUTO group to determine α_s without recourse to Monte Carlo calculations involving fragmentation parameters or to counting jets. A value for $\alpha_s = 0.19 \pm 0.02$ (statistical error) ± 0.04 (systematic error) is obtained at $\sqrt{s} = 30$ GeV. The systematic error is caused by the cut defining the onset of hard-gluon effects in the $K_\perp$ distribution.

2. Cluster analysis of hadronic events

At the higher PETRA energies hadron events are characterized by jets, a stream of collimated particles;

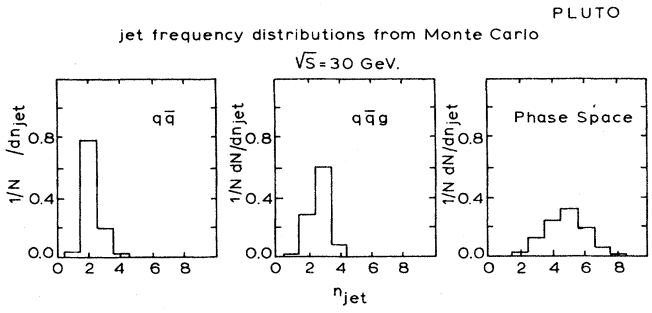

FIG. 107. The jet frequency distributions for various model calculations.

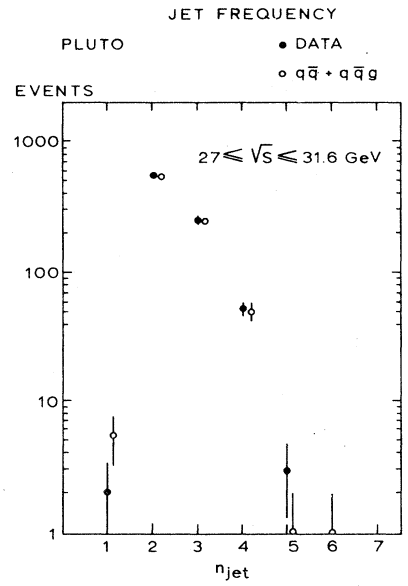

FIG. 108. The measured frequency distribution (closed circles) and the prediction for this distribution of a QCD model with a mixture of $q\bar{q}$ and $q\bar{q}g$ events (open circles).

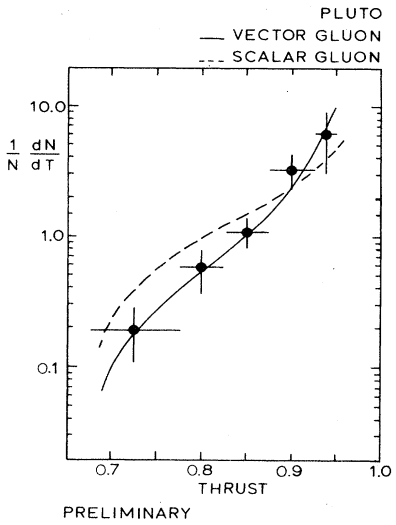

FIG. 109. The parton thrust distribution for the events with three jets. The solid curve is the absolute prediction for the spin=1 vector gluon, the dashed curve the prediction for spin=0.

and the PLUTO group has developed a pattern recognition program to identify in their detector clusters of particles (Daum *et al.*, 1981). Particles within an angle of 30° are collected into clusters. Two clusters are merged into one if they are within 30° of each other. When the energy, the sum of the energies of the individual particles contributing to a cluster, exceeds 2 GeV, it is called a jet. The experimental number of jets can then be determined for every hadronic event. The experimentally obtained jet frequency distribution can be compared with model calculations. Figure 107 shows the jet frequency distributions for some of these models, where the underlying parton processes are $q\bar{q}$, $q\bar{q}g$, and a phase-space-like production of hadrons. The $q\bar{q}$ model predicts a cluster distribution with a peak at two. The $q\bar{q}g$ model shows a slightly wider distribution peaking at three, and the phase-space calculation shows a wide distribution quite distinct from the others.

The data for the frequency distribution can be well described by a mixture of the $q\bar{q}$ and $q\bar{q}g$ distributions, as is shown in Fig. 108. From the class of two-jet events the tranverse momentum of the quarks is determined to be

$$P_t=(290\pm30)\ \text{MeV}\ .$$

The fraction of three-jet events is a measure of the strong coupling constant and determined by this method to be $\alpha_s=0.15\pm0.03$ (statistical error) ±0.03 (systematic error).

By identifying the jet with one of the underlying partons one can reconstruct the energy and direction of the quark or gluon. The parton thrust distribution can then be formed, and that distribution after subtraction of the $q\bar{q}$ background is displayed in Fig. 109. The solid curve is the absolute prediction from first-order QCD (Ellis *et al.*, 1976) for a vector gluon. The dashed curve is the spin =0 prediction normalized to the number of events. The spin-one solution is clearly favored (Berger *et al.*, 1980f).

D. Tests of QCD by the TASSO collaboration

1. Determination of the strong coupling constant α_s

The TASSO collaboration (Wu, 1980; Brandelik *et al.*, 1980e) uses in the analysis of their hadronic events the sphericity tensor (Bjorken and Brodsky, 1970b)

$$T_{\alpha\beta}=\Sigma_i P_{i\alpha}P_{i\beta}\ ,\quad \alpha,\beta=x,y,z \text{ and}$$

$$i=1,\ldots,N \text{ particles}\ .$$

The summation is over the charged particles, which have their momenta measured with the central detector. The tensor $T_{\alpha\beta}$ has eigenvectors $\mathbf{n}_1,\mathbf{n}_2,\mathbf{n}_3$ and the normalized eigenvalues

$$Q_k=\frac{\Sigma_i(\mathbf{P}_i\cdot\mathbf{n}_k)^2}{\Sigma(\mathbf{P}_i)^2}\ ,$$

which satisfy $Q_1+Q_2+Q_3=1$ and $0\le Q_1\le Q_2\le Q_3$.

The quantity sphericity S and aplanarity A can be expressed in the eigenvalues

$$S=\tfrac{3}{2}(Q_1+Q_2)\ ,$$

$$A=\tfrac{3}{2}Q_1\ ,$$

and a third quantity Y is defined as

$$Y=(\tfrac{3}{2})^{1/2}(Q_2-Q_1)\ .$$

The event plane is defined by the eigenvectors $\mathbf{n}_2$ and $\mathbf{n}_3$, and the sphericity axis is given by $\mathbf{n}_1$. As discussed

in Sec. III.C, the QCD model (Ali *et al.*, 1980a) has several parameters to describe the fragmentation of the quarks into hadrons. They are as follows:

(i) The average transverse momentum of the quarks, P_t. The distribution for the transverse momentum $k_\perp$ is assumed to be exponential and of the form $\exp(-k_\perp^2/2P_t^2)$.

(ii) The ratio of pseudoscalar (P) to vector mesons (V) produced in the fragmentation process $P/(P+V)$.

(iii) The function $D(z)$ describing the fragmentation of a quark into a hadron in the Feynman-Field model for u, d, and s quarks, depending on a parameter a_F according to

$$D(z)=1-a_F+3a_F(1-z)^2 ,$$

where $z=(E+P)_h/(E+P)_q$.

The data at $\sqrt{s}=30$ GeV was used by the TASSO group for the determination of α_s. The background from hard-photon bremsstrahlung was removed with an angular cut. The angle between $\mathbf{n}_1$ and the beam direction θ_N was required to be smaller than 80°. A total of 777 hadronic events remained, which are plotted in the triangular plot of Fig. 110 with axes S and A. The events populating the corner with small S and small A are the two-jet events; the planar events are spread out in the region of large S and small A. The region of $S\geq 0.25$ was used to determine α_s, a region dominated by the planar events due to the effects of hard-gluon bremsstrahlung. The parameters α_s and P_t were fitted for various values of the parameters $P/P+V$ and a_F. It was found that the α_s value is relatively independent of the fragmentation parameters. The average result for α_s was 0.16 ± 0.04. All the hadronic events were then fitted using this α_s value (obtained in the restricted area of $S\geq 0.25$) in order to determine the fragmentation parameters in a way which includes the two-jet events. The single-particle distribution is most sensitive to the a_F, the P_t of the quarks is most sensitive to the average squared momentum out of the event plane, and the multiplicity distribution is sensitive to $P/P+V$. The parameters obtained in this way are $a_F=0.57\pm0.20$, $P_t=0.32\pm0.04$ GeV/c, and $P/(P+V)=0.56\pm0.15$. These fragmentation parameters were used to refit α_s in the region of $S\geq 0.25$. As a final result they obtain $\alpha_s=0.17\pm0.02$ with a systematic error of 0.03 due to uncertainties of the QCD model.

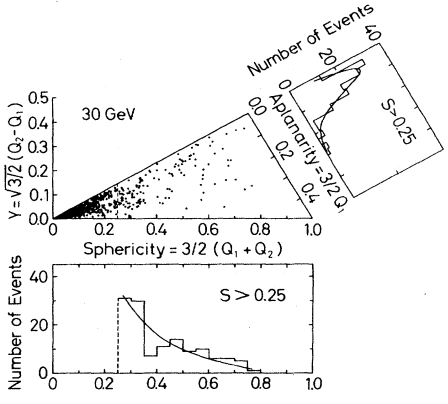

FIG. 110. Distributions of the observed events as a function of sphericity S and aplanarity A for the data at c.m. energy $W=30$ GeV. The events with $S\geq 0.25$ are projected onto the S and A axes as histograms. The curve is the result of fitting the QCD model to all the events (see text).

2. Comparison of the data with QCD

Having obtained the fragmentation parameters, one can compare the gross features of the data at $\sqrt{s}=12$ and 30 GeV with the QCD model predictions. The value of α_s at $\sqrt{s}=12$ GeV is given by

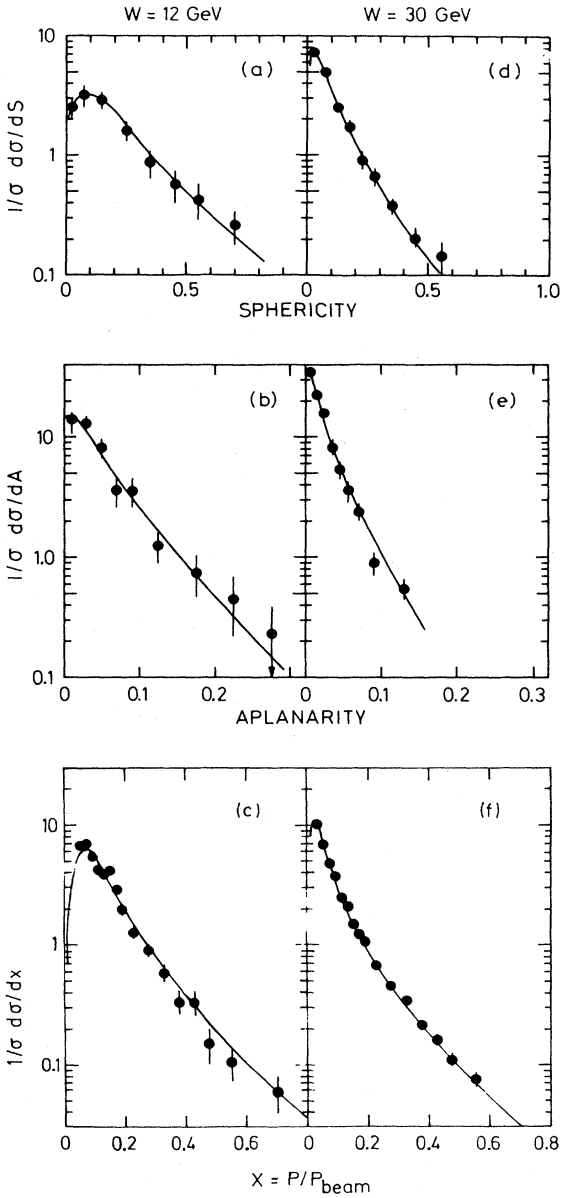

FIG. 111. Comparison of the QCD model (curves at $W=12$ GeV) for (a) sphericity, (b) aplanarity, (c) the single charged particle inclusive x distribution; and at $W=30$ GeV for (d) S, (e) A, and (f) x.

$$\alpha_s = \frac{12}{(33-2N_f)\ln^S/\Lambda^2} ,$$

where N_f is the number of flavors—taken to be five—and Λ is calculated with the α_s value obtained at $\sqrt{s}=30$ GeV. Figures 111(a)–(c) display the sphericity, aplanarity, and $x=P/P_{\text{beam}}$ distribution at $\sqrt{s}=12$ GeV, and Figs. 111(d)–(f) the data at $\sqrt{s}=30$ GeV. The agreement between the measurements and the QCD calculations is in all cases excellent.

3. Study of details of three-jet events

The 77 events with $S\geq 0.25$ and $A\leq 0.08$, the so-called planar events, are studied in detail with regard to their shape in order to investigate the detailed properties of the individual jets. The method of generalized sphericity (Wu and Zobernig, 1979) was used to analyze the three-jet structure. Instead of maximizing the triplicity as discussed in Sec. VII.B.3, Wu and Zobernig (1979) obtained an optimal separation on an event-by-event basis by minimizing the sum of the sphericities of the individual jets $(S_1+S_2+S_3)$. Having assigned with this method every charged particle to one of three jets, they could calculate the average momentum squared, P_t^2, with respect to the individual jet axis. The P_t^2 distribution of the 3×77) jets at high energy is compared with the distribution obtained for the two-jet events at low energy. At $\sqrt{s}=12$ GeV the P_t^2 is calculated with respect to the two axes found for these events. The behavior of the P_t^2 is found to be the same in both cases, and the QCD model for $\sqrt{s}=30$ GeV compares well with the data, as can be seen in Fig. 112(a). The shape of the three-jet events is expressed by the TASSO group in a

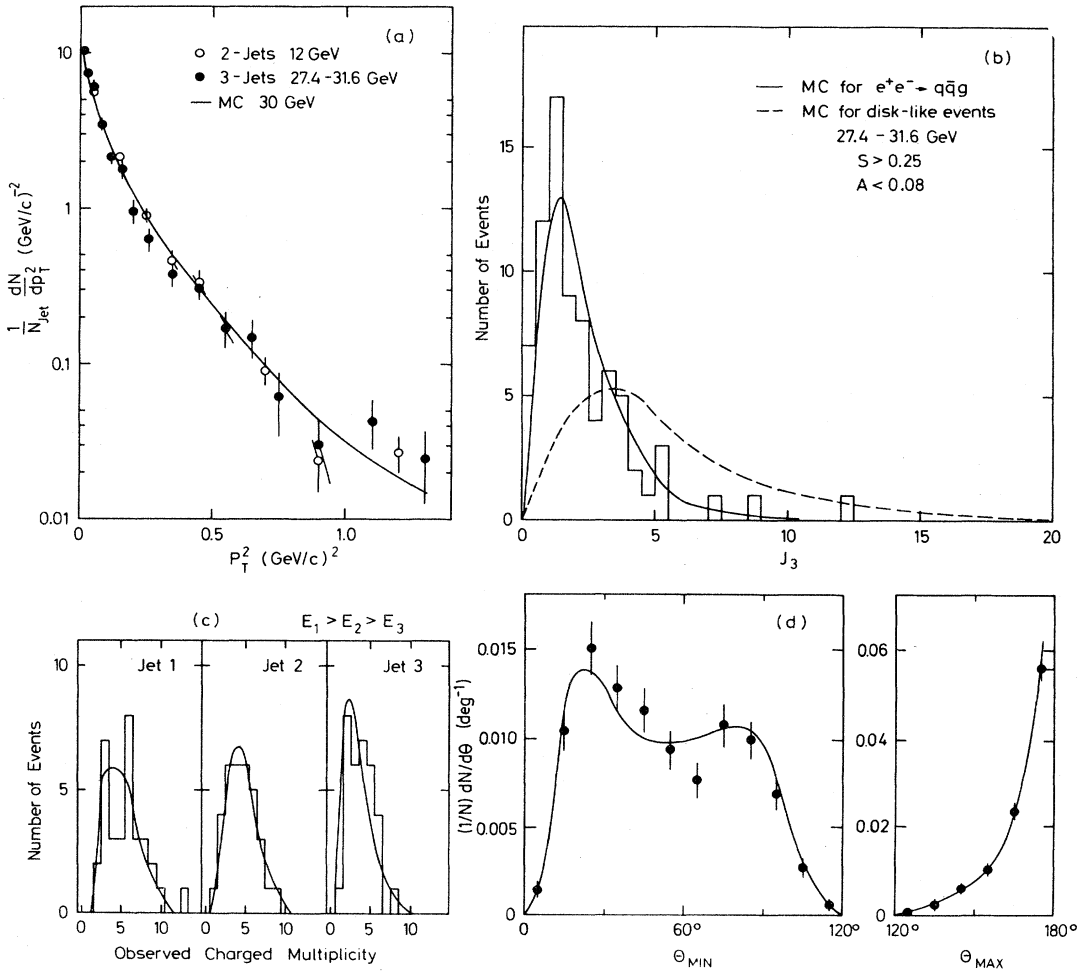

FIG. 112. (a) Observed transverse momentum distribution of hadrons from the planar region $S\geq 0.25$ and $A\leq 0.08$ with respect to three axes at $W=30$ GeV and the same quantity for all hadron events at $W=12$ GeV (open circles) with respect to two axes. The curve is the prediction of the QCD model. (b) Comparison of the trijettiness distribution for the planar events at $W=30$ GeV with the distributions of disklike events (dashed curve) and the QCD model (solid curve). The curves are normalized to the number of observed events. (c) Observed charged multiplicity distributions for the jets of highest (E_1), medium (E_2), and lowest (E_3) energy for the events in the planar region at $W=30$ GeV. (d) Distribution of the smallest and largest angles between any of the three jets for all hadron events at $W=30$ GeV. The curves are the results of the QCD model.

quantity called the "trijettiness" (Wu, 1980; Brandelik *et al.*, 1980e),

$$J_3=\frac{1}{N-3}\sum_{i=1}^{N}\frac{q_{\perp i}^2}{\frac{1}{2}P_t^2},$$

where P_t, the average quark transverse momentum is taken to be 0.33 GeV/c, and where $q_{\perp i}$ is the transverse momentum in the event plane with respect to the associated jet axis. For a genuine three-jet event, J_3 is expected to peak near 1, while for a disklike distribution J_3 is larger than 1. The J_3 distribution for the planar three-jet events is shown in Fig. 112(b). The QCD model is in good agreement with the data, but the disklike model (dashed curve) is unable to explain the distribution. The multiplicity distributions for the individual jets are shown in Fig. 112(c). The jets are ordered by their energies ($E_1\geq E_2\geq E_3$), and the data again compare well with the QCD predictions.

The energies of the jets were calculated from the angles between the jets, assuming the underlying partons to have zero mass. The minimum and maximum opening angles between the jets are plotted in Fig. 112(d) ($\theta_{\min}$ and $\theta_{\max}$) for the total hadron sample at $\sqrt{s}=30$ GeV. The $\theta_{\min}$ distribution is small for two-jet events and larger for the three-jet events. Both distributions are well described by the QCD model.

From the detailed comparisons made by the TASSO group of their data with the QCD model the conclusions are that (1) $\alpha_s=0.17\pm0.02$ (statistical error), ±0.03 (systematic errors), and (2) the shape and the detailed properties such as P_t^2, multiplicity, and angular distributions of the three-jet events are well described by QCD.

4. Evidence for a spin-1 gluon in three-jet events

As discussed in the previous section the TASSO group determines the axes of the three-jet events in the event plane with the generalized sphericity method. Having obtained the angle between the jets and knowing the total c.m. energy, they can easily calculate the energy of the individual jets. The fractional energy for each jet is defined as $x_i=E_i/E_b$, where E_i is the energy of jet i, and E_b is the beam energy. The jet can now be equated with the primordial parton, the quark or gluon. The energies of the partons are ordered such that $x_3\leq x_2\leq x_1$, and the relation $x_1+x_2+x_3=2$ follows from the definition of x_i. In addition, the quantity x_1 is equal to the thrust of the $q\bar{q}g$ system. When the masses of the quarks and gluons are neglected, the x_i are determined by the angles θ_i,

$$x_i=\frac{2\sin\theta_i}{\sin\theta_1+\sin\theta_2+\sin\theta_3},$$

[see Fig. 113(a)].

Ellis and Karliner (1979) have suggested the angle $\tilde{\theta}$ to test the vector gluon hypothesis against the scalar gluon possibility. This angle is obtained by boosting the three-parton system in such a way that partons 2 and 3 are in their rest frame [see Fig. 113(b)]. Neglecting the masses

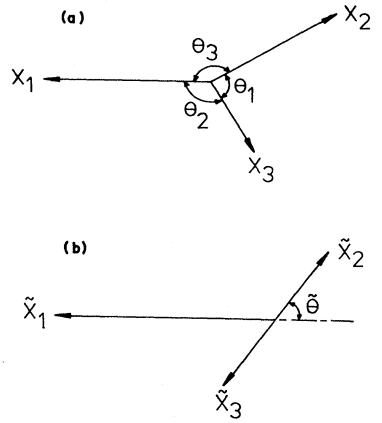

FIG. 113. (a) Momenta and angles of a $q\bar{q}g$ final state in the center-of-momentum frame. (b) The $q\bar{q}g$ final state transformed to the rest frame of particles 2 and 3.

of quarks and gluons, one can write $\cos\tilde{\theta}$ as,

$$\cos\tilde{\theta}=\frac{x_2-x_3}{x_1}=\frac{\sin\theta_2-\sin\theta_3}{\sin\theta_1}.$$

The double differential distributions for vector and scalar gluons can be expressed in terms of x_1 and x_2 as follows (Ellis *et al.*, 1976; DeGrand *et al.*, 1977; DeRujula, Ellis, Floratos, and Gaillard, 1978):

Vector:

$$\frac{1}{\sigma_0}\frac{d\sigma}{dx_1dx_2}=\frac{2\alpha_s}{3\pi}\frac{x_1^2+x_2^2}{(1-x_1)(1-x_2)}$$

$$+\cdots\text{ cycl. perm. of }1,2,3$$

Scalar:

$$\frac{1}{\sigma_0}\frac{d\sigma}{dx_1dx_2}=\frac{\tilde{\alpha}_s}{3\pi}\frac{x_3^2}{(1-x_1)(1-x_2)}$$

$$+\cdots\text{ cycl. perm. of }1,2,3$$

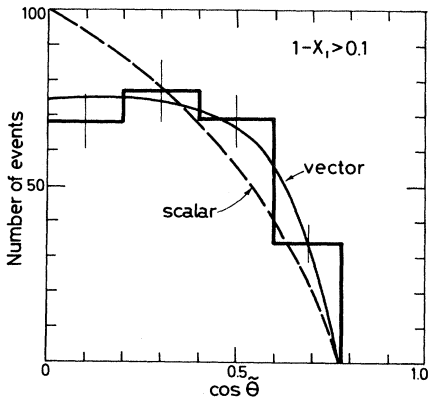

FIG. 114. Observed distribution of the data in the region $1-x_1\geq0.10$ as a function of the $\cos\tilde{\theta}$ angle. The solid line is the prediction for a vector gluon, the dashed line the prediction of the scalar gluon. Both curves are normalized to the number of events in the histogram.

In order to avoid the infrared divergencies from perturbative QCD which are expressed by the $(1-x_i)$ terms in the denominators, the events used for the determination of the spin have a thrust $x_1 < 0.90$. The number of two-jet events is reduced by this cut to about 18%.

The $\cos\tilde{\theta}$ distributions for events with $1-x_1 > 0.10$ are shown in Fig. 114. The predictions for the vector gluon (solid curve) and scalar gluon (dashed curve) are drawn normalized to the number of events. The spin-1 case describes the data very well, with a C.L. of 79% and the spin-zero case has a C.L. of only 0.2%. Various other checks have been made, such as higher moments of the $\cos\theta$ distribution and testing the thrust distribution itself against the two possibilities. In all these cases the spin-1 hypothesis has been favored (Brandelik *et al.*, 1980h).

The results of the TASSO group can be summarized as follows:

(i) The fragmentation parameters of the Feynman-Field model are determined to be $a_F = 0.57 \pm 0.20$, $P_t = 0.32 \pm 0.04$ GeV/c, and $P/P+V = 0.56 \pm 0.15$.

(ii) $\alpha_s = 0.17 \pm 0.02$ (statistical), ± 0.03 (systematic).

(iii) A good description of the data at $\sqrt{s} = 12$ and $\sqrt{s} = 30$ GeV is obtained by using these fragmentation parameters and α_s.

(iv) The three-jet data at $\sqrt{s} = 30$ GeV are consistent with the QCD model of vector gluons and exclude a scalar gluon with a confidence of about 10^{-4}.

E. QCD tests with the JADE detector

1. Three-jet events

The JADE group has used a model-independent way to test the shape of the three-jet events (Bartel and Peterson, 1980; Bartel *et al.*, 1980a). By forming the sphericity tensor (discussed in Sec. VII.D.1) in a similar way as the TASSO group, they are selecting planar events by making a cut in the quantity planarity $Q_2 - Q_1 < 0.1$, where Q_1 and Q_2 are two of the three eigenvalues of the tensor. The planar events are divided by a plane normal to the thrust axis into a narrow and broad jet (see Sec. VII.B.1). The charged and neutral particles contained in the broad jet are boosted to their combined rest system, and the details of the shape are then investigated using the boosted four vectors of the particles to calculate the quantities thrust (T^*), average transverse momentum $\langle P_T^* \rangle$, and charge multiplicity $n_{\rm ch}^*$. If the broad jet consists of two jets, these jets will appear in the boosted system well-separated and collinear. Figure 115 shows the T^* distribution of the broad jet in its own rest system. This distribution peaks at high thrust, which is indicative for a two-jet structure. For comparison the thrust distributions of all the hadron events at $\sqrt{s} = 12$ GeV are also plotted. The low-energy distribution can be completely understood as the production of quark-antiquark pairs and as a consequence is completely dominated by two-jet events. The similarity of the two distributions means that the broad jet has a two-jet structure. In Fig. 116 the quantities $\langle P_T^* \rangle$ and the multiplicity $n_{\rm ch}^*$ of the boosted broad jet are compared with the $\sqrt{s} = 12$ GeV data. Here, also, the similarity is striking. In conclusion, the data show in a model-independent way that the planar events at $\sqrt{s} = 30$ GeV exhibit the three-jet structure expected from hard-gluon bremsstrahlung.

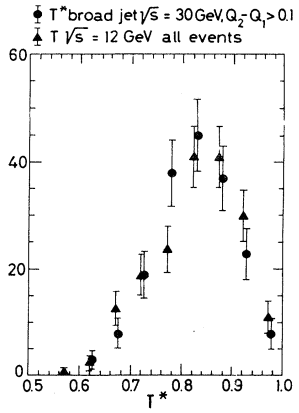

FIG. 115. The observed distribution of T^* as defined in the text for the broad jet of planar events compared with the two-jet thrust distribution at $\sqrt{s} = 12$ GeV.

2. Determination of α_s

The JADE group followed essentially the same procedure to obtain α_s as the TASSO group (Sec. VII.D.1), finding $\alpha_s = 0.18 \pm 0.03 \pm 0.03$. The fragmentation parameters were determined from the $x_i = p_i/p_{\rm beam}$, the sphericity, the planarity, and the $\langle P_T^2 \rangle_{\rm out}$ distribution. This last distribution, the average transverse momentum squared out of the event plane, is shown in Fig. 117 together with the QCD prediction (Yamada, 1980). The fragmentation parameters as defined in Sec. VII. D.1 were found to be $a_F = 0.5 \pm 0.1$, $P_t = 0.3 \pm 0.03$, and $P/(P+V) = 0.5 \pm 0.1$ in good agreement with the values found by the TASSO collaboration. The observed charged multiplicity distribution was also well reproduced by the above-mentioned parameters.

The JADE group has, in addition, investigated wheth-

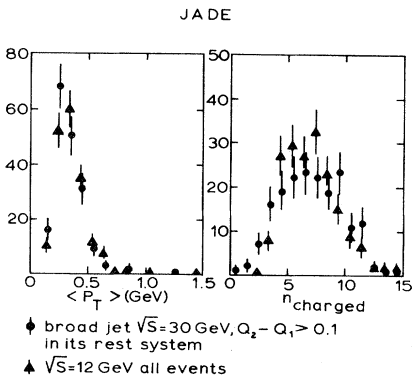

FIG. 116. The observed $\langle P_T^* \rangle$ and $n_{\rm ch}^*$ distribution of the broad jet at $\sqrt{s} \approx 30$ GeV in its rest system compared with the two-jet events as $\sqrt{s} = 12$ GeV.

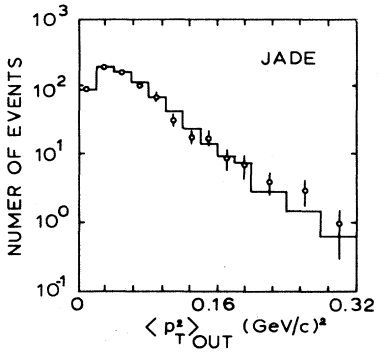

FIG. 117. The measured distribution of the $\langle P_T{}^2 \rangle$ out of the event plane. The histogram is the QCD calculation.

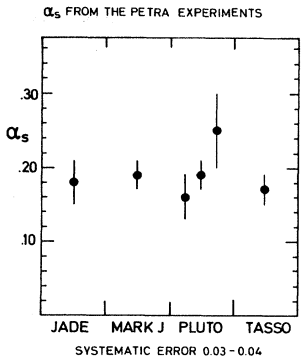

FIG. 118. The α_s values obtained by the four groups.

er the jets from the fragmentation of a quark are different from a gluon (Bartel *et al.*, 1981d). This result was first presented at the Wisconsin conference (Yamada, 1980) and they found an indication that the gluon jet produces higher yield of low-energy particles emitted at large angles to the jet axis in agreement with a prediction of Anderson, Gustafson, and Peterson (Anderson, Gustafson, and Peterson, 1978, 1980).

F. Summary of QCD tests

From the studies of the four PETRA groups the following picture emerges:

(1) The rate and the shape of the three-jet events can be explained only by QCD and not by any other model tried so far.

(2) The running coupling constant of the strong interaction ranges from 0.15 to 0.19. The values reported by the groups are shown in Fig. 118. It has to be noted that in these determinations the QCD correction to the two-jet graph is not included. The systematic error reported by the groups is 0.03 to 0.04.

(3) Parton energies and directions can be reconstructed.

(4) The PLUTO and TASSO groups have reported evidence for the vector nature of the gluon using the reconstructed directions and energies of the partons.

(5) The important non-Abelian aspect of QCD which leads to triple gluon vertices has not been tested so far.

VIII. CONCLUSIONS

After three years of experimentation the main physics results obtained at PETRA can be summarized as follows:

(1) QED is valid to a distance $< 10^{-16}$ cm. Electrons, muons, and τ leptons are pointlike with sizes smaller than 10^{-16} cm.

(2) The leptonic vector and axial-vector coupling constants of the weak neutral current are determined to be in agreement with the predictions of the standard SI(2)$\times$U(1) theory using purely leptonic interactions for the first time.

(3) Using models containing two neutral bosons, one can tightly restrict the masses of the two Z's.

(4) The first results on the measurements of the total cross section of the two-photon exchange reaction producing hadrons have been reported.

(5) The relative cross sections for the single photon annihilation reaction producing hadrons and the event distributions show that there is no new charge-$\frac{2}{3}$ quark pair production up to $\sqrt{s} = 36.7$ GeV.

(6) No evidence has been found for the production of heavy leptons, spin-zero partners of the electron and muon expected in supersymmetric theories, free quarks, or heavy long-living particles.

(7) An average hadronic event at $\sqrt{s} = 30$ GeV contains approximately $11\pi^{\pm}$, $1.4K^0$, $\bar{K}^0$, $1.4K^{\pm}$, and $0.4p,\bar{p}$ in the final state.

(8) Tests of QCD have been performed, and no deviations from this model have been observed.

(9) Three-jet events have been discovered, and the rate and the shape of these events can be explained only by the hard noncollinear gluon bremsstrahlung expected in QCD.

(10) The running coupling constant α_s has been measured and evidence has been reported for the vector nature of the gluon.

All these results have been made possible by the good performance of PETRA since its beginning.

ACKNOWLEDGMENTS

I wish to thank my colleagues of the MARK-J collaboration and to acknowledge helpful discussions with W. de Boer (CELLO), D. Cords (JADE), D. Pandoulas (TASSO), and U. Timm (PLUTO). I thank Professor H. Schopper, Professor G. Voss, Professor A. N. Diddens, Professor E. Lohrmann, Professor V. Soergel, and Dr. G. Soehngen for their valuable support. I thank Professor Samuel C. C. Ting for his continuous support and encouragement.

REFERENCES

Abrams, G. S. V., *et al.*, 1979, Phys. Rev. Lett. **43**, 477.
Ali, A., 1979, Z. Phys. C **1**, 25.
Ali, A. 1981, DESY Report No. 81/032 (unpublished).
Ali, A., and M. A. B. Beg, 1981, Phys. Lett. **103B**, 376.
Ali, A., J. G. Körner, Z. Kunst, J. Willrodt, G. Kramer, G. Schierholz, and E. Pietarinen, 1979, Phys. Lett. B **82**, 285.
Ali, A., *et al.*, 1979, Phys. Lett. **82B**, 285.
Ali, A., *et al.*, 1980a, Nucl. Phys. **176B**, 454.
Ali, A., *et al.*, 1980b, Phys. Lett. **93B**, 155.
Ali, A., *et al.*, 1981, Nucl. Phys. **191B**, 93.
Alles-Borelli, V., M. Bernardini, D. Bollini, P. L. Brunini, E. Fiorentino, T. Massam, L. Monari, F. Palmonari, and A. Zichichi, 1972, Nuovo Cimento A **7**, 345.
Anderson, B., G. Gustafson, and C. Peterson, 1978, Nucl. Phys. B **135**, 273.
Anderson, B., G. Gustafson, and C. Peterson, 1980, Z. Phys. C **3**, 223.
Anderson, H. L., H. S. Matis, and L. C. Myrianthopoulos, 1978, Phys. Rev. Lett. **40**, 1061.
Applequist, T., and H. Georgi, 1978, Phys. Rev. D **8**, 4000.
Arteaga-Roméro, Napoléon, Antoine Jaccarini, and Paul Kessler, 1969, C. R. Acad. Sci., Ser. B **269**, 153.
Augustin, J. E., *et al.*, 1975, Phys. Rev. Lett. **34**, 233.
Babcock, John, and Jonathan L. Rosner, 1976, Phys. Rev. D **14**, 1286.
Bacci, C., G. Penso, G. Salvini, R. Baldini-Celio, G. Capon, C. Mencuccini, G. P. Murtas, A. Reale, and M. Spinetti, 1971, Lett. Nuovo Cimento **2**, 73.
Bacci, C., *et al.*, 1979, Phys. Lett. B **86**, 234.
Baier, R., J. Engels, and B. Peterson, 1979, University of Bielefeld Report No. B1-TP79/10 (unpublished).
Balakin, V. E., V. M. Budner, and I. F. Ginzburg, 1970, Zh. Eksp. Teor. Fiz. Pis'ma Red. **11**, 559 [JETP Lett. **11**, 388].
Baltay, C., 1979, in *Proceedings of the Nineteenth International Conference on High Energy Physics,* Tokyo, 1978, edited by S. Homma, M. Kawaguchi, and H. Miyazawa (Physical Society of Japan, Tokyo), p. 882.
Barber, D. P., *et al.*, 1979a, Phys. Rev. Lett. **42**, 1110.
Barber, D. P., *et al.*, 1979b, Phys. Rev. Lett. **42**, 1113.
Barber, D. P., *et al.*, 1979c, Phys. Lett. B **85**, 463.
Barber, D. P., *et al.*, 1979d, Phys. Rev. Lett. **43**, 830.
Barber, D. P., *et al.*, 1979e, Phys. Rev. Lett. **43**, 901.
Barber, D. P., *et al.*, 1979f, Phys. Rev. Lett. **43**, 1915.
Barber, D. P., *et al.*, 1979g, Phys. Lett. B **89**, 139.
Barber, D. P., *et al.*, 1980a, Phys. Rev. Lett. **44**, 1722.
Barber, D. P., *et al.*, 1980b, Phys. Rep. **63**, 337.
Barber, D. P., *et al.*, 1980c, Phys. Lett. B **95**, 149.
Barber, D. P., *et al.*, 1980d, Phys. Rev. Lett. **45**, 1904.
Barber, D. P., *et al.*, 1981, Phys. Rev. Lett. **46**, 1663.
Barger, V., W. Y. Keung, and E. Ma, 1980a, Phys. Rev. Lett. **44**, 1169.
Barger, V., W. Y. Keung, and E. Ma, 1980b, Phys. Rev. D **22**, 727.
Barger, V., W. Y. Keung, and E. Ma, 1980c, Phys. Lett. B **94**, 377.
Bartel, W., and A. Peterson, 1980, in *Proceedings of the XVth Recontre de Moriond,* edited by J. Trân Thanh Van (Editions Frontieres, Dreux, France, 1980), Vol. 2, p. 143.
Bartel, W., *et al.*, 1979a, Phys. Lett. B **88**, 171.
Bartel, W., *et al.*, 1979b, Phys. Lett. B **89**, 136.
Bartel, W., *et al.*, 1980a, Phys. Lett. B **91**, 142.
Bartel, W., *et al.*, 1980b, Phys. Lett. B **91**, 152.
Bartel, W., *et al.*, 1980c, Phys. Lett. B **92**, 206.
Bartel, W., *et al.*, 1980d, Z. Phys. C **6**, 295.
Bartel, W., *et al.*, 1981a, Phys. Lett. B **99**, 277.
Bartel, W., *et al.*, 1981b, Phys. Lett. B **99**, 281.
Bartel, W., *et al.*, 1981c, Phys. Lett. B **100**, 364.
Bartel, W., *et al.*, 1981d, Phys. Lett. B **101**, 129.
Bartel, W., *et al.*, 1981e, Phys. Lett. B **101**, 361.
Bassetto, A., M. Ciafoloni, and G. Marchesini, 1978, Phys. Lett. B **83**, 207.
Bebek, C., *et al.*, 1981, Phys. Rev. Lett. **46**, 84.
Behrend, H. J., *et al.*, 1981a, Phys. Lett. B **103**, 148.
Behrend, H. J., *et al.*, 1981b, in proceedings of the International Conference on High Energy Physics, Lisbon (unpublished).
Behrend, H. J., *et al.*, 1981c, Phys. Scr. **23**, 610.
Berends, F. A., K. J. F. Gaemers, and R. Gastmans, 1973a, Nucl. Phys. B **57**, 381.
Berends, F. A., K. J. F. Gaemers, and R. Gastmans, 1973b, Nucl. Phys. B **63**, 381.
Berends, F. A., K. J. F. Gaemers, and R. Gastmans, 1974, Nucl. Phys. B **68**, 541.
Berends, F. A., and R. Kleiss, 1981, Nucl. Phys. B **177**, 237.
Berends, F. A., and G. J. Komen, 1976, Phys. Lett. B **63**, 432.
Berger, Ch., 1980, in $\gamma\gamma$ *Collisions,* edited by G. Cochard and P. Kessler, Lecture Notes in Physics (Springer, Berlin), Vol. 134, p. 82.
Berger, Ch., *et al.*, 1978a, Phys. Lett. B **76**, 243.
Berger, Ch., *et al.*, 1978b, Phys. Lett. B **78**, 176.
Berger, Ch., *et al.*, 1979a, Phys. Lett. B **81**, 410.
Berger, Ch., *et al.*, 1979b, Phys. Lett. B **82**, 449.
Berger, Ch., *et al.*, 1979c, Phys. Lett. B **86**, 413.
Berger, Ch., *et al.*, 1979d, Phys. Lett. B **86**, 418.
Berger, Ch., *et al.*, 1979e, Phys. Lett. B **89**, 120.
Berger, Ch., *et al.*, 1980a, Phys. Lett. B **90**, 312.
Berger, Ch., *et al.*, 1980b, Phys. Lett. B **91**, 148.
Berger, Ch., *et al.*, 1980c, Phys. Lett. B **94**, 87.
Berger, Ch., *et al.*, 1980d, Phys. Lett. B **94**, 254.
Berger, Ch., *et al.*, 1980e, Phys. Lett. B **95**, 313.
Berger, Ch., *et al.*, 1980f, Phys. Lett. B **97**, 459.
Berger, Ch., *et al.*, 1980g, Z. Phys. C **4**, 269.
Berger, Ch., *et al.*, 1981a, Phys. Lett. B **99**, 287.
Berger, Ch., *et al.*, 1981b, Phys. Lett. B **99**, 292.
Berger, Ch., *et al.*, 1981c, Phys. Lett. B **99**, 489.
Berger, Ch., *et al.*, 1981d, Phys. Lett. B **100**, 351.
Berger, Steven B., and Bernard T. Feld, 1973, Phys. Rev. D **8**, 3875.
Bernardini, M., D. Bollini, P. L. Brunini, E. Fiorentino, T. Massam, L. Monari, F. Palmonari, F. Rimondi, and A. Zichichi, 1973, Nuovo Cimento A **17**, 383.
Beron, B. L., *et al.*, 1974, Phys. Rev. Lett. **33**, 663.
Besch, H. J., H. W. Eisermann, B. Löhr, G. Nöldeke, M. Tonutti, W. Vollrath, R. Wilcke, H. Hoffman, H. C. Dehne, H. Kowalski, H. J. Von Eyss, and H. von der Schmitt, 1979, Phys. Lett. B **81**, 79.
Bienlein, J. K., *et al.*, 1978, Phys. Lett. B **78**, 360.
Bjorken, J. D., 1979, Phys. Rev. D **19**, 335.
Bjorken, J. D., and S. J. Brodsky, 1970a, Phys. Rev. D **1**, 176.
Bjorken, J. D., and S. J. Brodsky, 1970b, Phys. Rev. D **1**, 1416.
Bletzacker, F., and H. T. Nieh, 1977, Phys. Rev. D **16**, 2115.
Blietschau, J., *et al.*, 1976, Nucl. Phys. B **114**, 189.
Böhm, A., 1980, in *High Energy Physics-1980,* proceedings of the XX International Conference, Madison, Wisconsin, edited by L. Durand and L. G. Pondrom (AIP, New York, 1981), p.

551; Aachen Report No. PITHA 80/9 (unpublished).
Bonneau, G., and F. Martin, 1971, Nucl. Phys. B **27**, 381.
Bosetti, P. C., *et al.*, 1978, Nucl. Phys. B **142**, 1.
Bramón, A., and M. Greco, 1971, Lett. Nuovo Cimento **2**, 522.
Brandelik, R., *et al.*, 1979a, Phys. Lett. B **83**, 261.
Brandelik, R., *et al.*, 1979b, Phys. Lett. B **86**, 243.
Brandelik, R., *et al.*, 1979c, Phys. Lett. B **88**, 199.
Brandelik, R., *et al.*, 1979d, Nucl. Phys. B **148**, 189.
Brandelik, R., *et al.*, 1980a, Phys. Lett. B **89**, 418.
Brandelik, R., *et al.*, 1980b, Phys. Lett. B **92**, 199.
Brandelik, R., *et al.*, 1980c, Phys. Lett. B **94**, 91.
Brandelik, R., *et al.*, 1980d, Phys. Lett. B **94**, 259.
Brandelik, R., *et al.*, 1980e, Phys. Lett. B **94**, 437.
Brandelik, R., *et al.*, 1980f, Phys. Lett. B **94**, 444.
Brandelik, R., *et al.*, 1980g, Phys. Lett. B **97**, 448.
Brandelik, R., *et al.*, 1980h, Phys. Lett. B **97**, 453.
Brandelik, R., *et al.*, 1980i, Z. Phys. C **4**, 87.
Brandelik, R., *et al.*, 1981, Phys. Lett. B **99**, 163.
Brandt, S., and H. Dahmen, 1979, Z. Phys. C **1**, 61.
Brandt, S., Ch. Peyrou, R. Sosnowski, and A. Wroblewski, 1964, Phys. Lett. **12**, 57.
Branson, J., 1981, *Proceedings 1981 International Symposium on Lepton and Photon Interactions of High Energies,* Bonn, Federal Republic of Germany, 1981, edited by W. Pfeil (Physikalisches Institut, Universtiy of Bonn), p. 279.
Bremer, H. D., *et al.*, 1980, DESY Report No. 80/76 (unpublished).
Brodsky, S., and S. D. Drell, 1970, Annu. Rev. Nucl. Sci. **20**, 147.
Brodsky, S., T. Kinoshita, and H. Terazawa, 1970, Phys. Rev. Lett. **25**, 972.
Brodsky, S., T. Kinoshita, and H. Terazawa, 1971, Phys. Rev. D **4**, 1532.
Budnev, V. M., and A. E. Kaloshin, 1979, Phys. Lett. B **86**, 351.
Budny, R., 1975, Phys. Lett. B **55**, 227.
Burkhardt, H., *et al.*, 1981, Nucl. Instrum. Methods **184**, 319.
Burmester, J., *et al.*, 1977a, Phys. Lett. B **68**, 297.
Burmester, J., *et al.*, 1977b, Phys. Lett. B **68**, 301.
Büsser, F. W., 1980, in *Proceedings of the XIX Internationale Universitäts wochen für Kernphysik 1980,* Schlädming, Steiermark, Austria, edited by P. U. Gras (Springer Verlag, Wien, New York, 1980), p. 139.
Calogero, F., and C. Zemack, 1960, Phys. Rev. **120**, 1860.
Capdequi-Peyranere, M., *et al.*, 1978, Montpellier Report No. PM/78/18 (unpublished).
Carimalo, C., P. Kessler, and J. Parisi, 1979a, Phys. Rev. D **20**, 1057.
Carimalo, C., P. Kessler, and J. Parisi, 1979b, Phys. Rev. D **20**, 2170.
Carimalo, C., P. Kessler, and J. Parisi, 1980, Phys. Rev. D **21**, 669.
Celmaster, W., and R. Gousalves, 1980, Phys. Rev. Lett. **44**, 560.
Chadwick, K., *et al.*, 1981, Phys. Rev. Lett. **46**, 88.
Chetyrkin, K. G., A. L. Kataev, and F. V. Tkachov, 1979, Phys. Lett. B **85**, 277.
Cords, D., 1980, in *High Energy Physics—1980,* proceedings of the XX International Conference, Madison, Wisconsin, edited by L. Durand and L. G. Pondrom (AIP, New York, 1981), p. 590.
Cottingham, W. N., and I. H. Dunbar, 1979, J. Phys. G **5**, L155.
Criegee, L., and G. Knies, 1981, DESY Report No. 81/044 (unpublished); Phys. Rep. (in press).
Curci, G., M. Greco, and Y. Srivastava, 1979a, Phys. Rev. Lett. **43**, 834.
Curci, G., M. Greco, and Y. Srivastava, 1979b, Nucl. Phys. B **159**, 451.
Darden, C. W., *et al.*, 1978a, Phys. Lett. B **76**, 246.
Darden, C. W., *et al.*, 1978b, Phys. Lett. B **78**, 364.
Daum, H. J., *et al.*, 1981, Z. Phys. C **8**, 167.
De Grand, T. A., Yee Jack Ng, and S.-H. H. Tye, 1977, Phys. Rev. D **16**, 3251.
De Groot, E. H., G. J. Gounaris, and D. Schildknecht, 1979, Phys. Lett. B **85**, 399.
De Groot, E. H., G. J. Gounaris, and D. Schildknecht, 1980a, Z. Phys. C **5**, 127.
De Groot, E. H., G. J. Gounaris, and D. Schildknecht, 1980b, Phys. Lett. B **90**, 427.
De Groot, E. H., and D. Schildknecht, 1980a, Phys. Lett. B **95**, 128.
De Groot, E. H., and D. Schildknecht, 1980b, Z. Phys. C **10**, 139.
De Groot, J. G. H., *et al.*, 1979a, Z. Phys. C **1**, 143.
De Groot, J. G. H., *et al.*, 1979b, Phys. Lett. B **82**, 292.
De Groot, J. G. H., *et al.*, 1979c, Phys. Lett. B **82**, 456.
De Rujula, A., J. Ellis, E. G. Floratos, and M. K. Gaillard, 1978, Nucl. Phys. B **138**, 387.
Dine, M., and J. Sapirstein, 1979, Phys. Lett. **43**, 152.
Dittmann, P., and V. Hepp, 1981, Z. Phys. C **10**, 283.
Drell, S. D., 1958, Ann. Phys. **4**, 75.
Drumm, D., *et al.*, 1980, Nucl. Instrum. Methods **176**, 333.
Duinker, P., 1981, in proceedings of the Conference on High Energy Physics, Lisbon, (unpublished); Report No. NIKHEF-H/81-30 (unpublished).
Duinker, P., and D. Luckey, 1980, Comments Nucl. Part. Phys. **9**, 123.
Eichler, R., and D. Haidt, 1981, JADE Collaboration, private communication.
Ellis, J., 1981, Comments Nucl. Part. Phys. **5**, 153.
Ellis, J., and M. K. Gaillard, 1976, CERN Report No. 76-18, 21 (unpublished).
Ellis, J., M. K. Gaillard, and G. G. Ross, 1976, Nucl. Phys. B **111**, 253.
Ellis, J., and I. Karliner, 1979, Nucl. Phys. B **148**, 141.
Euler, H., and B. Kockel, 1953, Naturwissenschaften **23**, 246.
Faiman, D., H. J. Lipkin, and H. R. Rubinstein, 1975, Phys. Lett. B **59**, 269.
Faissner, H., 1979, in *New Phenomena in Lepton-Hadron Physics,* edited by D. E. C. Fries and J. Wess (Plenum, New York), p. 371.
Faissner, H., E. Frenzel, W. Heinrigs, A. Preussger, D. Samm, and U. Samm, 1981, Phys. Lett. B **103**, 234.
Farhi, E., 1977, Phys. Rev. Lett. **39**, 1587.
Farrar, G. R., and P. Fayet, 1978a, Phys. Lett. B **76**, 575.
Farrar, G. R., and P. Fayet, 1978b, Phys. Lett. B **79**, 442.
Farrar, G. R., and P. Fayet, 1980, Phys. Lett. B **89**, 191.
Fayet, P., 1977, Phys. Lett. B **69**, 489.
Fayet, P., 1979a, Phys. Lett. B **84**, 421.
Fayet, P., 1979b, Phys. Lett. B **86**, 272.
Fayet, P., and S. Ferrara, 1977, Phys. Rep. C **32**, 249.
Febel, A., and G. Hemmie, 1979, DESY Report No. M79/13 (unpublished).
Feldman, G., *et al.*, 1977, Phys. Rev. Lett. **38**, 117.
Feldman, G. J., and M. L. Perl, 1977, Phys. Rep. **33**, 285.
Feynman, R. P., 1969, Phys. Rev. Lett. **23**, 1415.
Feynman, R. P., and R. D. Field, 1978, Nucl. Phys. B **136**, 1.

Field, J., 1980, Nucl. Phys. B **168**, 477.
Fil'kov, L. V., 1967, Zh. Eksp. Teor. Fiz. Pis'ma Red. **5**, 192 (1967) [JETP Lett. **5**, 153].
Fluegge, G., 1979a, Z. Phys. C **1**, 121.
Fluegge, G., 1979b, in *Proceedings of the European Physical Society International Conference on High Energy Physics,* Geneva, Switzerland, 1979, edited by A. Zichichi (CERN, Geneva, 1980), p. 259.
Frazer, W. R., and J. F. Gunion, 1979, Phys. Rev. D **20**, 147.
Furmanski, W., and S. Pokorski, 1979, Nucl. Phys. B **155**, 253.
Gabriel, T. A., and R. L. Bishop, 1978, Nucl. Instrum. Meth. **155**, 81.
Georgi, H., and S. Weinberg, 1978, Phys. Rev. D **17**, 275.
Glashow, S. L., 1961, Nucl. Phys. **22**, 579.
Gol'fand, Yu. A., and E. P. Likthman, Zh. Eksp. Teor. Fiz. Pis'ma Red. **13**, 452 (1971) [JETP Lett. **13**, 323].
Grassberger, P., and R. Kögerler, 1976, Nucl. Phys. B **106**, 451.
Greco, M., 1977, Nuovo Cimento A **42**, 315.
Greco, M., 1978, Phys. Lett. B **77**, 84.
Greco, M., and Y. Srivastava, 1978, Nuovo Cimento A **43**, 88.
Gross, D. J., and F. A. Wilczek, 1973, Phys. Rev. Lett. **30**, 1343.
Hanson, G., *et al.*, 1973, Lett. Nuovo Cimento **7**, 587.
Hanson, G., *et al.*, 1975, Phys. Rev. Lett. **35**, 1609.
Hasert, F. J., *et al.*, 1973, Phys. Lett. B **46**, 121.
Heile, F. B., *et al.*, 1978, Nucl. Phys. B **138**, 189.
Heisterberg, R. H., L. W. Mo, T. A. Nunmaker, K. A. Lefler, A. Skuja, A. Abashian, N. E. Booth, C. C. Chang, C. Li, and C. H. Wang, 1980, Phys. Rev. Lett. **44**, 635.
Hepp, V., 1980, in High Energy Physics—1980, proceedings of the XX International Conference, Madison, Wisconsin, edited by L. Durand and L. G. Pondrom (AIP, New York, 1981), p. 622.
Herb, S. W., *et al.*, 1977, Phys. Rev. Lett. **39**, 252.
Hilger, E., 1980, DESY Report No. 80/34 (unpublished).
Hilger, E., B. L. Beron, R. L. Carrington, R. L. Ford, W. T. Hill, R. Hofstadter, E. B. Hughes, A. D. Liberman, T. W. Martin, L. H. O'Neill, J. W. Simpson, and L. K. Resvanis, 1977, Phys. Rev. D **15**, 1809.
Hofstadter, R., 1975, in *Proceedings of the 1975 International Symposium on Lepton and Photon Interactions at High Energies,* edited by W. T. Kirk, (Stanford Linear Accelerator Center, Stanford University, Stanford, California, 1975), p. 869.
Hoyer, P., *et al.*, 1979, DESY Report No. 79/21 (unpublished).
Hung, P. Q., and J. J. Sakurai, 1977, Phys. Lett. B **69**, 323.
Hung, P. Q., and J. J. Sakurai, 1979, Phys. Lett. B **88**, 91.
Jaccarini, A., *et al.*, 1970, Lett. Nuovo Cimento **4**, 933.
Kleinert, H., L. P. Staunton, and P. H. Weisz, 1972, Nucl. Phys. B **38**, 87.
Kobayashi, M., and T. Maskawa, 1973, Prog. Theor. Phys. **49**, 652.
Konishi, K., and A. Ukawa, and G. Veneziano, 1979, Phys. Lett. B **80**, 259.
Kramer, G., G. Schierholz, and J. Willrodt, 1978, Phys. Lett. B **79**, 249.
Krammer, M., and H. Krasemann, 1978, DESY Report No. 78/66 (unpublished).
Krasemann, H., and J. A. M. Vermaseren, 1979, private communication.
Kroll, N. M., 1966, Nuovo Cimento **45**, 65.
Landau, L. D., and E. M. Lifschitz, 1934, Sov. Phys. **6**, 244.
Langacker, P., *et al.*, 1979, in *Neutrino '79,* proceedings of the International Conference on Neutrinos, Weak Interactions, and Cosmology, Bergen, Norway, 1979, edited by A. Haatuft and C. Jarlskog (University of Bergen, Bergen, 1980), Vol. 1, p. 276.
Lee, T. D., and G. C. Wick, 1970, Phys. Rev. D **2**, 1033.
Levy, N., P. Singer, and S. Toaff, 1976, Phys. Rev. D **13**, 2662.
Liede, I., and M. Roos, 1979, in *Neutrino '79,* proceedings of the International Conference on Neutrinos, Weak Interactions, and Cosmology, Bergen, Norway, 1979, edited by A. Haatuft and C. Jarlskog (University of Bergen, Bergen, 1980), Vol. 1, p. 309.
Litke, A., 1970, Ph.D. thesis, Harvard University (unpublished).
Low, F. E., 1960, Phys. Rev. **120**, 582.
Marini, A., *et al.*, 1981, contributed paper to the International High Energy Physics Conference, Lisbon (unpublished).
Marshall, R., 1980, Rutherford Laboratory Report No. RL-80-29 (unpublished).
Meyer, H., 1979, in *Proceedings of the 1979 International Symposium on Lepton and Photon Interactions at High Energies, Fermilab,* edited by T. B. W. Kirk and H. D. I. Abarbanel (Fermilab, Batavia, Illinois, 1980), p. 214.
Mo, L. W., and Y. S. Tsai, 1969, Rev. Mod. Phys. **41**, 205.
Newman, H., 1980, in *High Energy Physics—1980,* proceedings of the XX International Conference, Madison, Wisconsin, edited by L. Durand and L. G. Pondron (AIP, New York, 1981), p. 627.
Newman, H., R. Averill, J. Eshelman, L. Law, M. E. Law, J. Leong, R. Little, H. Mieras, K. Strauch, G. Tarnopolsky, R. Wilson, and H. Winick, 1974, Phys. Rev. Lett. **32**, 483.
Novikov, V. N., and S. I. Éĭdel'man, 1975, Yad. Fiz. **21**, 1029 (1975) [Sov. J. Nucl. Phys. **21**, 529].
O'Neill, L. H., B. L. Beron, R. L. Carrington, R. L. Ford, E. Hilger, R. Hofstadter, E. B. Hughes, A. D. Liberman, T. W. Martin, J. W. Simpson, and L. K. Resvanis, 1976, Phys. Rev. Lett. **37**, 395.
Orito, S., 1979, in *Proceedings of the 1979 International Symposium on Lepton and Photon Interactions at High Energies, Fermilab,* edited by T. B. W. Kirk and H. D. I. Abarbanel (Fermilab, Batavia, Illinois, 1980) p. 52.
Orito, S., R. Visentin, F. Ceradini, M. Conversi, S. d'Angelo, L. Paoluzi, and R. Santonico, 1974, Phys. Lett. B **48**, 165.
Pandoulos, D., 1980, in *High Energy Physics—1980,* proceedings of the XX International Conference, Madison, Wisconsin, edited by L. Durand and L. G. Pondrom (AIP, New York, 1981), p. 596.
Paoluzi, L., F. Ceradini, M. L. Ferrer, R. Santonico, G. Barbiellini, S. Orito, and T. Tsuru, 1974, Lett. Nuovo Cimento **10**, 435.
Peccei, R. D., and H. R. Quinn, 1977a, Phys. Rev. Lett. **38**, 1440.
Peccei, R. D., and H. R. Quinn, 1977b, Phys. Rev. D **16**, 1791.
Perl, M. L., *et al.*, 1975, Phys. Rev. Lett. **35**, 1489.
PETRA Proposal, 1976, updated version DESY.
Pohl, M., 1981, Review talk, XVIth Recontre du Moriond (unpublished); Aachen Report No. PITHA 81/10 (unpublished).
Politzer, H. D., 1973, Phys. Rev. Lett. **30**, 1346.
Porter, F., 1981, contribution paper, proceedings of the International High Energy Physics Conference, Lisbon (unpublished).
Prescott, C. Y., *et al.*, 1978, Phys. Lett. B **77**, 347.

Prescott, C. Y., *et al.*, 1979, Phys. Lett. B **84**, 524.
Quigg, C., 1979, in *Proceedings of the 1979 International Symposium on Lepton and Photon Interactions at High Energies, Fermilab,* edited by T. B. W. Kirk and H. D. I. Abarbanel (Fermilab, Batavia, Illinois), p. 239.
Radutskii, G. M., 1967, Zh. Eksp. Teor. Fiz. Pis'ma Red. **6**, 911 (1967) [JETP Lett. **6**, 336].
Radutskii, G. M., 1969, Yad. Fiz. **8**, 115 (1968) [Sov. J. Nucl. Phys. **8**, 65].
Reithler, H., 1979, Phys. Bl. **35**, 630.
Renner, B., 1971, Nucl. Phys. B **30** 634.
Revol, J. P., 1981, Ph.D. thesis, MIT (unpublished).
Ringhofer, K., and H. Salecker, 1975, contributed paper to the International Symposium on Lepton and Photon Interactions at High Energies, Stanford (unpublished).
Ripken, G., 1979, private communication.
Rosner, J. R., C. Quigg, and H. B. Thacker, 1978, Phys. Lett. B **74**, 350.
Rykaczewski, H., 1981, Ph.D. thesis, Aachen (unpublished).
Sakurai, J. J., 1979, in *Neutrino '79,* proceedings of the International Conference on Neutrinos, Weak Interactions, and Cosmology, Bergen, Norway, 1979, edited by A. Haatuft and C. Jarlskog (University of Bergen, Bergen, 1980), Vol. 1, p. 267.
Salam, A., 1968, in *Elementary Particle Theory,* edited by Nils Svartholm (Almqvist and Wiksell, Stockholm), p. 367.
Sanders, H. G., 1974, Diplomarbeit, Phys. Inst. Aachen, Report No. HEP74/07 (unpublished).
Schierholz, G., and K. Sundermeyer, 1972, Nucl. Phys. B **40**, 125.
Schopper, H., 1981, Comments Nucl. Part. Phys. **10**, 33.
Schwitters, R., 1975, in *Proceedings of the 1975 International Symposium on Lepton and Photon Interactions, Stanford,* edited by W. T. Kirk (Stanford Linear Accelerator Center, Stanford University, Stanford, 1975), p. 5.
Sehgal, L. M., 1978, in *Proceedings of the International Conference on Neutrino Physics, West Lafayette,* edited by Earle C. Fowler (Purdue University, West Lafayette), p. 253.
Sehgal, L. M., 1979, in *Proceedings of the Symposium on Lepton and Hadron Interactions, Visegrad,* edited by F. Csikor, G. Pintér, and G. Pócsik (Institute Theoretical Physics, Budapest, 1980), p. 29.
Siegrist, J. L., 1980, Ph.D. thesis (unpublished); Report No. SLAC-225 UC 34d (unpublished).
Soeding, P. 1979, in *Proceedings of the European Physical Society International Conference on High Energy Physics,* Geneva, Switzerland, 1979, edited by A. Zichichi (CERN, Geneva, 1980), p. 271.
Steffen, K., 1979, Internal Report No. DESY M-79/07 (unpublished).
Susskind, L., 1979, Phys. Rev. D **20**, 2619.
Takeda, H., 1981, JADE collaboration, private communication.
Terazawa, H., 1973, Rev. Mod. Phys. **45**, 615.
Timm, U., 1980, DESY Report No. 80/70 (unpublished).
Tsai, Y. S., 1974, Rev. Mod. Phys. **46**, 815.
Tsai, Y. S., 1979, Report No. SLAC-PUB-2450 (unpublished).
Vermaseren, J. A. M., 1980, in *$\gamma\gamma$-Collisions,* edited by G. Cochard and P. Kessler, Lecture Notes in Physics (Springer, Berlin), Vol. 134, p. 35.
Voss, G. A., 1979, Internal Report No. DESY M/79/16 (unpublished).
Wagner, W., 1980, in *High Energy Physics—1980,* proceedings of the XX International Conference, Madison, Wisconsin, edited by L. Durand and L. G. Pondrom (AIP, New York, 1981), p. 576.
Weinberg, S., 1967, Phys. Rev. Lett. **19**, 1264.
Weinberg, S., 1972, Phys. Rev. D **5**, 1412.
Weinberg, S., 1977, Phys. Rev. Lett. **40**, 223.
Weinberg, S., 1979, Phys. Rev. D **19**, 1277.
Weiss, J. M., *et al.*, 1979, Phys. Lett. B **101**, 439.
Wess, J., and B. Zumino, 1974, Nucl. Phys. B **70**, 39.
Wiik, B. H., 1979, in *Neutrino '79,* in proceedings of the International Conference on Neutrinos, Weak Interactions, and Cosmology, Bergen, Norway, 1979, edited by A. Haatuft and C. Jarlskog (University of Bergen, Bergen, 1980).
Wilczek, F., 1978, Phys. Rev. Lett. **40**, 279.
Winter, K., 1979, in *Proceedings of the 1979 International Symposium on Lepton and Photon Interactions at High Energies, Fermilab,* edited by T. B. W. Kirk and H. D. I. Abarbanel (Fermilab, Batavia, Illinois), p. 258; Report No. CERN-EP/79/132 (unpublished).
Wu, S. L., 1980, in *High Energy Physics—1980,* proceedings of the XX International Conference, Madison, Wisconsin, edited by L. Durand and L. C. Pondrom (AIP, New York, 1981), p. 664.
Wu, S. L., and G. Zobernig, 1979, Z. Phys. C **2**, 1979.
Yamada, S., 1980, in *High Energy Physics—1980,* proceedings of the XX International Conference, Madison, Wisconsin, edited by L. Durand and L. G. Pondrom (AIP, New York, 1981), p. 616.
Zee, A., 1973, Phys. Rev. D **8**, 4038.